論文 / 著書情報
Article / Book Information

題目(和文)	高時間分解能レーザ計測による乱流燃焼における火炎及び流動の動的特性に関する研究
Title(English)	Investigation on Flame and Flow Dynamics in Turbulent Combustion by High-Speed Laser Diagnostics
著者(和文)	城地文音
Author(English)	Ayane Johchi
出典(和文)	学位:博士（工学）, 学位授与機関:東京工業大学, 報告番号:甲第9775号, 授与年月日:2015年3月26日, 学位の種別:課程博士, 審査員:店橋　護,小酒　英範,齊藤　卓志,村上　陽一,志村　祐康
Citation(English)	Degree:, Conferring organization: Tokyo Institute of Technology, Report number:甲第9775号, Conferred date:2015/3/26, Degree Type:Course doctor, Examiner:,,,,
学位種別(和文)	博士論文
Type(English)	Doctoral Thesis

Doctoral Dissertation

Investigation on Flame and Flow Dynamics in Turbulent Combustion by High-Speed Laser Diagnostics

Supervisors

Professor : Mamoru Tanahashi

Department of Mechanical and Aerospace Engineering
Graduate School of Science and Engineering
Tokyo Institute of Technology

Ayane Johchi

Contents

The results of Chapter 2 and 3 have been partially published in the following journal article:

1. A. Johchi, Y. Naka, M. Shimura, M. Tanahashi and T. Miyauchi, Investigation on Rapid Consumption of Fine Scale Unburned Mixture Islands in Turbulent Flame via 10 kHz Simultaneous CH-OH PLIF and SPIV, Proceedings of the Combustion Institute, 35(3):3663–3671, 2015, doi: http://dx.doi.org/10.1016/j.proci.2014.09.007

The results of Chapter 4 have been partially published in the following conference proceeding:

1. A. Johchi, L. Zimmer and M. Tanahashi, Investigation on the Acoustic Behavior of a Turbulent Swirl-Stabilized Combustor Fed with Liquid Fuel, Proceedings of 17th International Symposium on Applications of Laser Techniques to Fluid Mechanics, p. 4.3.2, 2014

Chapter 1

Introduction

1.1 Energy and environmental issues

Energy and environmental problems constitute one of the most crucial issues in our society. After the Industrial Revolution, the energy demands of the society and accordingly energy supply have been continuously growing. Figure 1.1 shows the trend of the primary energy consumption for the last several decades in the world [1, 2]. Although fossil fuels such as coal, oil and natural gas are the dominant fuel, several problems have been posed. Energy and environmental issues such as the drain of fossil fuel, greenhouse gas emission leading to climate change and energy security become increasingly severe.

Recently, renewable energy is gathering worldwide attention as a new energy resource. The power generation using solar energy and wind force do not emit greenhouse gases. However, the share of renewable is not enough high to become dominant energy source at this stage although it shows a rapid growth. Nuclear energy is one of the possibilities to overcome these issues with its non-emission power generation method at the low cost. In Japan, the power generation using nuclear energy appeared promising to improve self-sufficiency as well. However, after nuclear disaster at the Fukushima 2011, the energy supply by the nuclear energy drops and is now 0 %. While the share in the primary energy over the world had been growing until around 2000, it has been declining until now. It is

expected that very few new plants are built in OECD countries [3]. The stringent safety requirements make it difficult to be competitive in the markets. Therefore, fossil fuel energies still dominate the energy supply with the share of 86 % in 2012. According to BP Energy outlook 2035 [3], fossil fuels lose share but they are still the dominant form of energy in 2035 with a share of 81 %.

Natural gas is now regarded as a promising resource with its abundance and the low carbon emission. In addition to conventional natural gases, productions of unconventional natural gas resources such as tight gas, shale gas and coalbed methane (CBM) become feasible. Figure 1.2 shows world natural gas resources by major region [4]. World recoverable total resources of conventional and unconventional natural gas are estimated to be equal to over 250 years of current production. As can be seen in Fig. 1.2, the global natural gas resource bases are widely dispersed geographically. It will help to improve energy security. Another merit is that the natural gas emits less carbon dioxide and pollutants when it burns in comparison to other fossil fuels. It mainly consists of methane (CH4) whose carbon number is small. From the point of view of the global warming issues, natural gas is effective resource.

Therefore, majority of the energy in the world is produced by combustion up until now and from now on. The development of highly efficient and low-emission combustor has a large contribution to the energy and environmental issues.

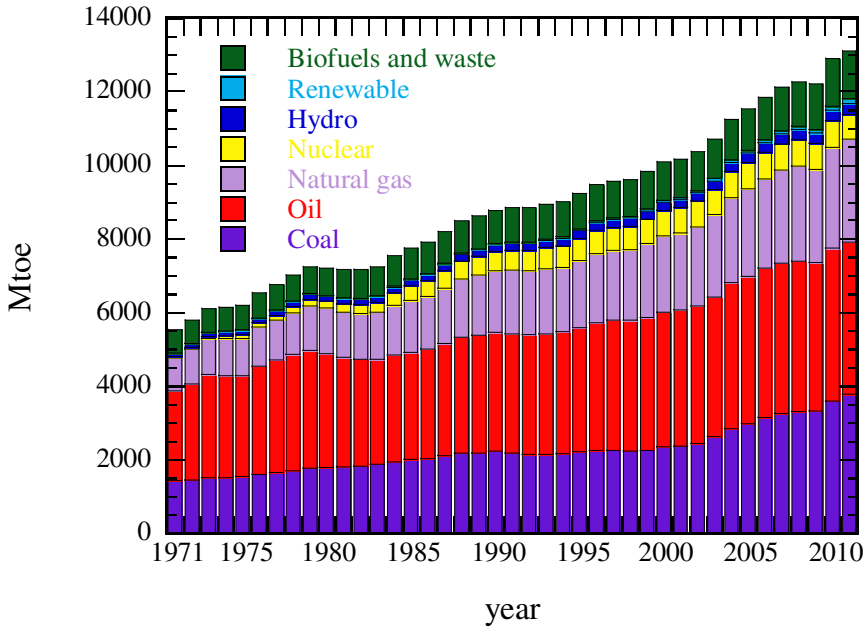

Figure 1.1: Total primary energy consumption trend in the world [1, 2].

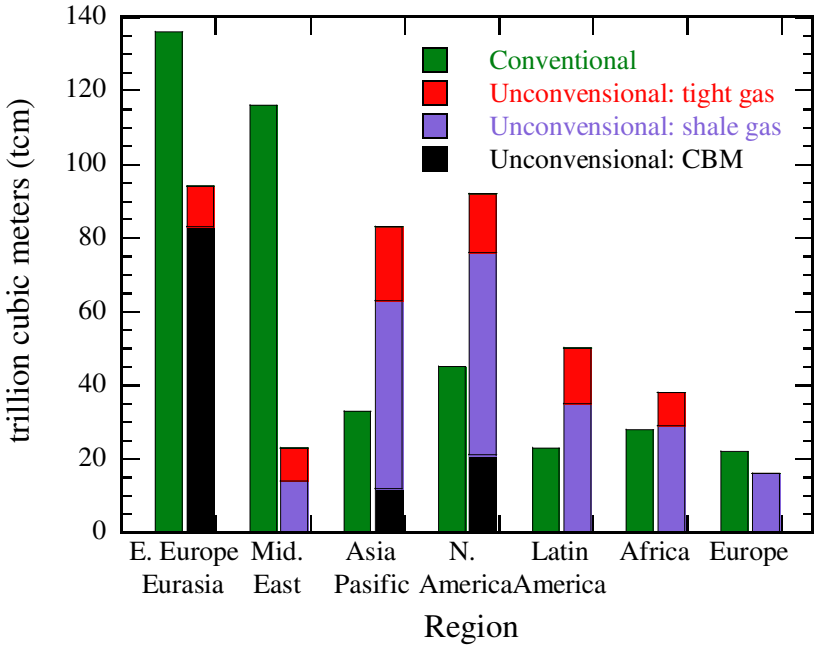

Figure 1.2: World natural gas resources by major region, January 2010 [4].

1.2 Combustion models for the numerical simulation

Computational fluid dynamics (CFD) increasingly plays an important role in the design process of combustor involving reacting flows. An application of large-eddy simulation (LES) to realistic combustion systems is becoming possible through recent developments in computation technology. In LES, unsteady large-scale phenomena are calculated by filtering the physical quantities and separating them into grid scale (GS) and subgrid scale (SGS) components.

Peters [5] proposed a combustion diagram and four regimes for the classification of flame structure. The structure of flame is classified based on the ratio of the turbulent intensity to the laminar burning velocity (u'_{rms}/S_L) and the ratio of the characteristic length of turbulence (the integral length scale) to the laminar flame thickness (l/δ_F). The four regimes are wrinkled flamelets, corrugated flamelets, thin reaction zones and broken reaction zones as shown in Fig.1.3. In wrinkled flamelets and corrugated flamelets regime, the flame thickness is smaller than the smallest turbulence scale (Kolmogolov scale). Fundamental flame elements hence retain the laminar flame structures. The flame fronts are subject to stronger flame–vortex interaction in corrugated flamelet regimes since $u'_{rms} > S_L$. When flame zone thickness reaches to the scale of Kolmogolov eddies in thin reaction zone regimes, the smaller eddies can now penetrate into the preheat zone and broaden it. However, the reaction sheet is still only wrinkled with its structure unaffected by eddy motion as long as the reaction layer thickness is smaller than Kolmogolov scale.

In the case of LES of turbulent premixed flame in flamelets regime, the flame thickness is assumed very thin compared to the LES filter size. It is impossible to determine the inner structure of the flame in LES, and the flame structure in SGS must be modeled.

G-equation [6] is often used to describe the flame front wherein the reaction zone is represented by an infinitely thin scalar iso-surface, based on the flamelet

concept. In LES with G-equation approach, a filtered G-equation has to be solved and a SGS combustion model is required. Since turbulent flame structure has not been fully clarified yet, SGS combustion model that can be applied to turbulent combustion field with various conditions has not be developed yet.

Shiwaku et al. [7] have proposed a SGS combustion model based on hierarchical structure of turbulent premixed flame. In the model, a SGS turbulent burning velocity is estimated based on fractal characteristics such as fractal dimension and inner cutoff in the flamelet regimes. The model is further developed by introducing the determination procedure of the fractal dimension, which is given by the Fractal Dynamic SGS combustion model of Miyauchi et al. [8]. In addition, a dilatation effect is separately modeled and the two models are combined [9]. he model has been evaluated by the 3D DNS result and the superiority to the conventional models has been indicated. However, due to the limitation of computation resources, DNSs under high pressure and/or in high Reynolds number turbulence, which are the case in the realistic combustion devices, are hardly conducted yet. Therefore, experimental investigations on flame and flow dynamics are necessary to validate the model with realistic conditions in engineering applications.

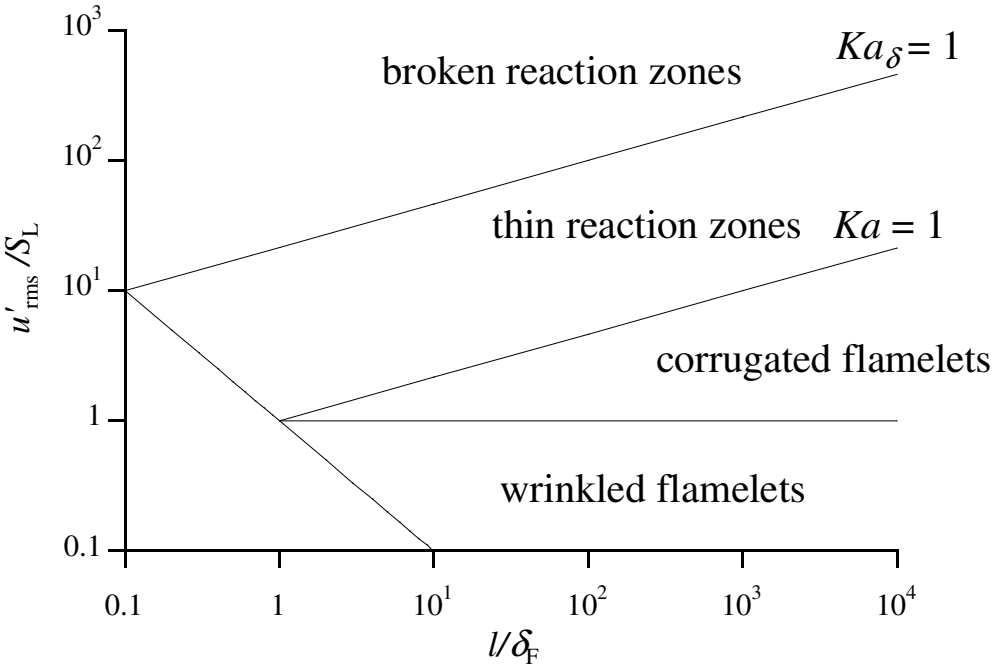

Figure 1.3: Combustion diagram proposed by Peters [5].

1.3 Gas turbine combustor with high-efficiency and low-emission

In engineering applications, a gas turbine has an advantage with its high power density. With heavy duty, jet engines and industrial gas turbines are utilized in aircraft, ships and electricity generation. To enhance the efficiency, turbine inlet temperature has been increasingly raised in industrial gas turbines. However, increasing operation temperature leads to a large emission of nitrogen oxide (NOx). To prevent local hot spots within the combustor that causes of significant thermal NOx formation, a lean premixed (LP) combustion is considered as a strong candidate. Uniform lean mixture of fuel and air is formed that burns with lower temperature than in the non-premixed combustion. Therefore, to reduce NOx emissions, the LP combustion is widely employed [10, 11].

In many industrial combustors, liquid fuel is used such as gas turbine engines, diesel engines and direct injection engines. It has advantages in the applicability to various configurations and the easiness of transportation. In new generation combustors, lean premixed prevaporized (LPP) combustion are considered [12–14].

One of the main problems of LP or LPP combustion is the susceptibility to dynamic phenomena such as blow-off, flashback [15, 16] and thermoacoustic instability, which can even cause damage in the combustor. Candel [17], Huang and Yang [18] made the extensive reviews about the combustion instability. To understand and control the combustion instability is one of the most important issues to achieve stable operation of the gas turbine combustor.

It has been known that the thermoacoustic instability is caused by the feedback interaction between natural acoustic modes of the combustor and an oscillation of a heat release rate [19].

The heat release rate and the acoustic pressure interact with each other in the combustor. The acoustic oscillation in the combustion chamber vibrates the reactant gas and flame, leading to the oscillation of the heat release. The unsteady

heat release and flame generate pressure wave that propagates in the chamber. The conditional expression of the thermoacoustic instability is denoted as the equation that is known as Rayleigh criterion,

$$\int_t \iiint_\Omega p'q' d\Omega dt > 0, \tag{1.1}$$

in which the heat release rate and the acoustic pressure oscillate in phase. Then a self-sustained instability occurs growing the oscillation amplitudes.

On the other hand, in many industrial applications including gas turbine combustor, swirling flow is used to stabilize flame. The general concept of the swirl-stabilized combustor is to anchor flame with recirculation zone by strong radial momentum of the flow. The aerodynamic structure has also a large effect on the stabilization of the system.

A non-reacting annular jet exhibit asymmetrical vortex rings, which are caused by Kelvin-Helmholtz instability because of shear between the jet and the ambient air. When swirling motion is introduced, the flow field exhibits helical waves, which replace the vortex rings to become the dominant structure. Beyond a critical strength in the swirling motion, axial and radial pressure gradients are set up, leading to the formation of the inner recirculation zone (IRZ) [20, 21].

IRZ plays an important role in swirl-stabilized combustor to ignite the inlet reactants flow by transporting hot products and radicals back. In a strong swirling motion, the precession of the vortex core of the mean swirling motion around the burner axis has been observed in experiments and simulations. The motion is refereed as precessing vortex core (PVC) and has gathered great interest. Syred [22] made an extensive review about PVC. The aerodynamic instability mode causes an oscillation of IRZ, which can relate to PVC.

The presence of combustion makes the flow structure much more complex with gas expansion, density variation and an acoustic pressure. It is reported that the helical aerodynamic mode and PVC have a significant effect on a mixing process in the gas turbine model combustor [18, 23, 24]. Hence, such coherent structures in swirling flow largely affect the flame instability. To understand and control

the combustion instability phenomena, it is required to understand the flame and flow dynamics in turbulent combustion.

1.4 Laser diagnostics in combustion

Turbulent flames are often experimentally investigated by planar laser induced fluorescence (PLIF) [25, 26] of molecules and radicals produced in chemical reactions, such as OH [27], CO [28], CH [29–31] and CH_2O [32]. Since OH radicals exist in the burned gas, OH PLIF is useful to separate the unburned and burned region. On the other hand, CH radicals are produced at the flame front and have very narrow width to represent flame front. Therefore, combining OH and CH radical detection, the flame structure can be investigated [33]. Simultaneous PLIF and particle image velocimetry (PIV), which gives instantaneous velocity maps, has enhanced the understanding of flame-turbulence interaction in non-premixed jet flame [30], lifted non-premixed flame [34] and swirl-stabilized combustor [35]. For investigating 3D flame structures, a system based on simultaneous dual-plane CH PLIF, single-plane OH PLIF and dual-plane stereoscopic PIV (SPIV) [36] is developed. The flame characteristics such as curvature and strain rate at the flame front are then discussed.

Although previous simultaneous measurements have clarified the instantaneous flame structure, they are typically limited to acquisition rates of approximately 10 Hz. To resolve the temporal development of a turbulent flame, repetition rates must exceed kHz order over long-duration. One approach to achieve high temporal resolution is multi-shot measurement with short time separation by laser cluster. High temporal resolution was achieved with multi-shot PLIF measurement of OH [37], CH [38, 39] and acetone as a fuel tracer [40]. Double-pulsed CH PLIF measurement has been realized to investigate local flame displacement speed in turbulent premixed flame by Tanahashi et al. [41]. These measurements clarify instantaneous flame dynamics. However, their duration time is not enough high to investigate unsteady evolution of turbulent flame.

Long-duration time-resolved measurements have become possible through recent developments in solid-state lasers, high-speed cameras and image intensifiers. Since the OH radical shows a high concentration in burned gas, OH PLIF with multi-kHz acquisition rate has been developed. Frequency-quadrupled Nd:YLF laser [42], dye lasers pumped by frequency-doubled Nd:YLF lasers [43] and frequency-doubled Nd:YAG lasers [44, 45] are used for high repetition rate OH PLIF. These techniques are combined with time-resolved PIV and used to investigate spatio-temporally unpredictable phenomena such as flashbacks [16], flame extinction [46] and flame hole dynamics and reignition events of non-premixed turbulent jet flame [47, 48]. These measurements also largely contribute to investigate the instability of gas turbine model combustors [49–51]. Recently, dual-plane OH PLIF at 10 kHz has been used to measure local flame displacement speeds [52, 53].

However, OH PLIF may not sufficiently investigate flame structures in high-Reynolds-number turbulence [30], which severely distorts the flame front and leads to complex flame structures. The OH radical does not directly indicate the primary reaction zone but the post-flame gases. In contrast, CH radicals are restricted to a narrow reaction layer of the reaction zone. Since burned and unburned gases are not easily distinguishable from CH images alone, combined CH-OH PLIF is important.

There exist few works have achieved high temporal resolution with CH PLIF. A possible way to generate UV pulses with high energy is by custom-built optical parametric oscillator (OPO) systems [54, 55]. Jiang et al. [54] have pumped OPO by a custom burst lasers and collected sets of ten CH images at 10 kHz in a non-premixed flame. Miller et al. [55] pumped the OPO system by a cluster of four double-pulsed, Q-switched Nd:YAG lasers. They excited the A-$X(1,1)$ band directly at 10 kHz and obtained sets of four CH images in a non-premixed flame.

Such multi-shot PLIF measurements have high temporal resolution and they can temporally resolve the flame development, whereas the issue is now the measurement duration time. Carter et al. [56] recently demonstrated a capability of a

long duration measurement to choose C-$X(0,0)$ band using Nd:YAG laser with an acquisition rate of 10 kHz.

1.5 Objectives

The main objective of the present study is clarifying the flame and flow dynamics in turbulent combustion by high-speed laser diagnostics in order to contribute the development of highly efficient and low-emission combustor. The objectives in each chapter are as follows.

In chapter 2, high-speed laser diagnostics consisting of CH–OH PLIF and stereoscopic PIV, which can measure flame structure and 3-component of velocity at 10 kHz, is developed. Its capability to investigate flow and flame dynamics is shown by applying the measurement to methane–air turbulent jet premixed flame.

In chapter 3, to clarify the flame and flow dynamics of turbulent premixed flame in high Reynolds number turbulence, the rapid consumption of the fine scale unburned mixtures, which are observed around the flame tip of the turbulent jet is investigated.

In chapter 4, to clarify the instability of liquid-fueled swirl-stabilized combustor, two dominant instabilities that are acoustic and aerodynamic instability are investigated by high–speed laser diagnostics.

Chapter 2

Development of high-speed laser diagnostics in turbulent combustion

2.1 Introduction and objectives

To investigate local flame structure and its dynamics in high Reynolds number turbulence, simultaneous planar laser induced fluorescence (PLIF) of CH and OH radical and particle image velocimetry (PIV) with high temporal resolution is important. However, the high repetition rate CH radical detection is hampered by the low density.

The capability of high-speed CH PLIF techniques that are overviewed in Sec. 1.4 have been demonstrated mostly in non-premixed flame. Since the density of the CH radical is significantly lower in premixed than that in non-premixed flames, CH PLIF in premixed flames is more difficult. In addition, they must be successfully combined with velocity measurement at the same temporal resolution to investigate flame-turbulence interactions.

The objective of this chapter is to develop simultaneous CH–OH PLIF and stereoscopic PIV with an acquisition rate of 10 kHz and a measurement duration exceeding 1.0 s, and to demonstrate its capability to investigate flame and flow dynamics in turbulent combustion. In Sec. 2.2, the basic theory of the measurement techniques used in this study is summarized and the measurement setups are shown in Sec. 2.3.1. The developed simultaneous measurement is applied to

methane–air turbulent jet premixed flame in Sec. 2.3.1.

2.2 Basic theory

In the present study, a measurement system for high-speed simultaneous laser diagnostics have been developed, which is composed of CH–OH planar laser induced fluorescence (PLIF) and stereoscopic particle imaging velocimetry (PIV). In this chapter, basic theories of LIF and PIV are firstly given. Then, stereoscopic method to obtain out-of-plane component of velocity is described.

2.2.1 Planar laser induced fluorescence (PLIF)

Fluorescence is a radiation emitted by atoms or molecules when it relaxes by spontaneous emission of a photon from a higher to a lower energy level. Laser induced fluorescence (LIF) excites an atom or molecule to an excited quantum state with laser radiation and observes the fluorescence of a particular atom or molecule taking an advantage of the nature that each atom and molecule has a specific spectral feature of absorption and emission line. LIF is firstly proposed by Wood [57] and is extended to two–dimensional (2D) measurement, named Planar LIF (PLIF), with laser light shaped geometrically thin to excite molecular transitions in the illuminated plane. PLIF is applied to determine different variables of the flow field in the plane of a laser light sheet: concentration (mole fraction) [58], temperature [59], pressure distribution [60] can be derived from calibrated LIF images.

In this study, PLIF is used to measure radical distribution qualitatively. The detailed description for the concentration measurement can be found in Daily [58]. The basic method to obtain the concentration of chemical species is briefly summarized here. The simplest system, illustrated in Fig. 2.1, is the two–level atom. The model has a ground state 1, and an excited state 2. The overall rate of the process is given by the product of a rate coefficient and the concentration of the molecule and photons. The radiative processes include absorption, induced emission and spontaneous emission. The rate coefficients of these processes are W_{12},

W_{21} and A_{21}, respectively. Induced emission arises when the presence of a radiation field, such as laser light source, forcing the molecule to the lower energy state. In addition, collisions play an important role and Q_{ij} denotes the rate coefficient of the energy transfer from an initial state i to a final state j.

Real molecular behavior is considerably more complex with attendance of vibrational and rotational sub-levels. The simplest molecular structure to consider is the two electronic level diatomic molecule, shown in Fig. 2.2. $N_1(i)$ and $N_2(i)$ denote the numbers of photons of each rotational sub-level i in the ground and excited electronic states, respectively. The index e is used specifically referring to the laser coupled states. Ignoring losses due to chemical reactions or predissociation, the rate equations, which are the conservation equation of the population density, then become:

$$\begin{aligned}\frac{dN_2(i)}{dt} &= \sum_{j\neq i} N_2(j)Q_{22}(j,i) + \sum_k N_1(k)Q_{12}(k,i) \\ &\quad - N_2(i)\left\{\sum_{j\neq i} Q_{22}(i,j) + \sum_k \left(Q_{21}(i,k) + A_{21}(i,k)\right)\right\} \qquad (2.1)\\ \frac{dN_2(e)}{dt} &= N_1(e)W_{12} + \sum_{i\neq e} N_2(j)Q_{22}(j,e) + \sum_k N_1(k)Q_{12}(k,e) \\ &\quad - N_2(e)\left\{\sum_{j\neq e} Q_{22}(e,j) + \sum_k \left(Q_{21}(e,k) + A_{21}(e,k)\right) + W_{21}\right\} \qquad (2.2)\\ \frac{dN_1(i)}{dt} &= \sum_k N_2(k)\left\{Q_{21}(k,i) + A_{21}(k,i)\right\} + \sum_{j\neq i} N_1(j)Q_{11}(j,i) \\ &\quad - N_1(i)\left\{\sum_{j\neq i} Q_{11}(i,j) + \sum_k Q_{12}(i,k)\right\} \qquad (2.3)\\ \frac{dN_1(e)}{dt} &= N_2(e)W_{21} + \sum_k N_2(k)\left\{Q_{21}(k,e) + A_{21}(k,e)\right\} \\ &\quad + \sum_{j\neq e} N_1(j)Q_{11}(j,e) - N_1(e)\left\{\sum_{j\neq e} Q_{11}(e,j) + \sum_k Q_{12}(e,k) + W_{12}\right\} \qquad (2.4)\end{aligned}$$

where $Q_{11}(i,j)$ and $Q_{22}(i,j)$ are the ground and excited state rotational collisional

rates. $Q_{12}(i,j)$ and $Q_{21}(i,j)$ are the electronic collisional energy transfer rates and $A_{21}(i,j)$ is the Einstein A coefficients from level i in the excited electronic state to level j in the ground electronic state which is the probability of decay in any direction. The conservation of total population is as followings.

$$N_T = \sum_i N_1(i) + \sum_i N_2(i) \tag{2.5}$$

The fractions of population of electronic states 1 and 2 are represented by α and β, respectively are then,

$$\alpha = \frac{N_1(e)}{N_1} \tag{2.6}$$

$$\beta = \frac{N_2(e)}{N_2} \tag{2.7}$$

where, N_1 and N_2 are the total population of electronic states 1 and 2.

$$N_1 = \sum_i N_1(i) \tag{2.8}$$

$$N_2 = \sum_i N_2(i) \tag{2.9}$$

Assuming the steady state, and using Eq. (2.2) to solve for N_2/N_T,

$$\frac{N_2}{N_T} = \frac{\frac{\alpha}{\beta} W_{12}}{\left\{ Q_{eff}(e) + A_{21}(e) + \left(\frac{\alpha}{\beta} + \frac{g_1(e)}{g_2(e)} \right) W_{12} \right\}} \tag{2.10}$$

where $g_1(e)$ and $g_2(e)$ are the degeneracies of the ground and excited laser coupled state respectively, and

$$Q_{eff}(e) \equiv Q_{22}(e) + Q_{21}(e) - \sum_{j \neq e} \frac{N_2(j)}{N_2(e)} Q_{22}(j,e) - \sum_k \frac{N_1(k)}{N_2(e)} Q_{12}(k,e) \tag{2.11}$$

$$Q_{22}(e) \equiv \sum_{j \neq e} Q_{22}(e,i) \tag{2.12}$$

$$Q_{21}(e) \equiv \sum_k Q_{21}(e,k) \tag{2.13}$$

$$A_{21}(e) \equiv \sum_k A_{21}(e,k) \tag{2.14}$$

$Q_{eff}(e)$ and $A_{21}(e)$ are the net collisional energy transfer and spontaneous emission rates from sub-state e respectively. Saturation excitation can be defined as

$$W_{12}^s \equiv \frac{Q_{eff} + A_{21}(e)}{\{\frac{\alpha}{\beta} + \frac{g_1(e)}{g_2(e)}\}} \tag{2.15}$$

so that

$$N_2 = N_T\{\frac{\frac{\alpha}{\beta}}{\frac{\alpha}{\beta} + \frac{g_1(e)}{g_2(e)}}\}\{\frac{W_{12}}{W_{12} + W_{12}^s}\} \tag{2.16}$$

The rate of absorption per molecule between state 1 and 2 can be related to the laser irradiance,

$$W_{12} \approx B_{12}\overline{E_\nu}\phi(\nu) \tag{2.17}$$

B_{12} is the Einstein coefficient for absorption, E_ν the local spectral irradiance, $\phi(\nu)$ the normalized spectral line shape function and ν the optical frequency of the transition. Here, laser line width is assumed narrower than the absorption line width [61].

In the limit of weak excitation ($W_{12} \ll W_{12}^s$), Eq. (2.16) will become:

$$N_2 \approx \frac{\frac{\alpha}{\beta}W_{12}}{Q_{eff}(e) + A_{21}(e)}N_T \tag{2.18}$$

while in the strong excitation limit ($W_{12} \gg W_{12}^s$):

$$N_2 \approx \frac{\frac{\alpha}{\beta}}{\frac{\alpha}{\beta} + \frac{g_1(e)}{g_2(e)}}N_T \tag{2.19}$$

From Eq. (2.19), if the laser irradiance is enough high, then N_1 and N_2 will occur in a fixed known ratio, independence of quenching rate, $Q_{eff}(e)$.

The spectral radiant power, $Q_F(\nu)$, an optical system collect is

$$Q_F(\nu) = \epsilon h\nu(\frac{A_{21}}{4\pi})\Omega_C \int_{\Delta t}\int_{V_C} N_2\phi(\nu)dV_C dt \tag{2.20}$$

where ϵ is the efficiency of the collection optics, h is Plank's constant, Ω_C is the solid angle of the collection optics. The integral is over focal volume defined by the intersection of the laser beam and the collection optics and over time. Thus, if a calibration constant is defined as

$$C \equiv h\nu(\frac{A_{21}}{4\pi})\Omega_C \int_{\Delta\nu_{Det}}\int_{V_C} \epsilon\phi(\nu)dV_C d\nu \tag{2.21}$$

then

$$Q_F = C\int_{\Delta t}\int_{V_C} N_2(t)dV_C dt \tag{2.22}$$

The fluorescence signal provides a measure of the population of the excitation state N_2, through Eq. (2.22). If a relationship can be found between the number density of all quantum states under excitation conditions, the total number density of the species can be deduced.

Einstein coefficients can be found in a number of sources. A large number of atomic transitions are listed in Wiese et al. [62, 63]. Radzig and Smirnof [64] give data for both atomic and molecular transitions. For molecules, the individual Einstein coefficients are a function of vibrational and rotational states as well. The transition probability data can be found in LIFBASE [65].

If the laser beam is spread into a sheet, then it is possible to image an entire plane onto an array of detectors. Here each focal volume is defined by the thickness of the laser sheet and the collection optics. In this Planar LIF (PLIF), Eq. (2.22) becomes

$$Q_F(x,y) = C\int_{\Delta t}\int_{V_C} N_2(x,y,t)dV_C dt \tag{2.23}$$

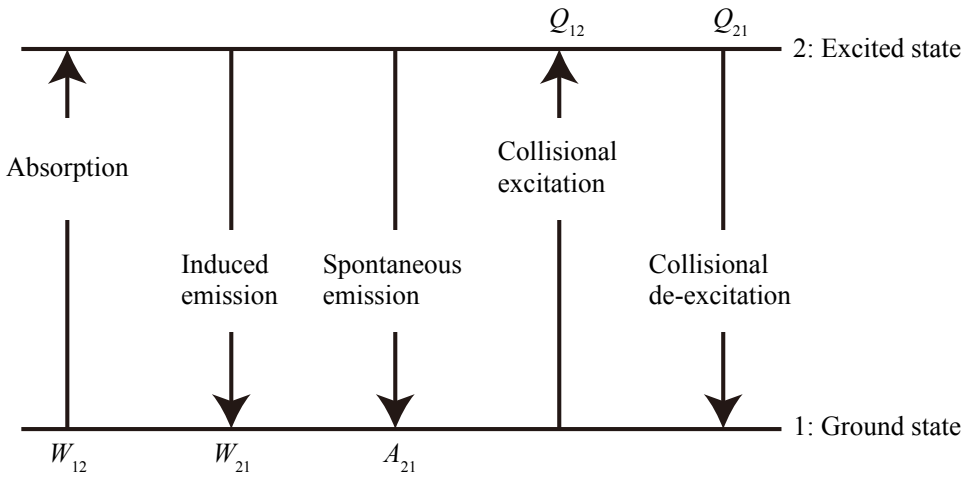

Figure 2.1: The two-level atom.

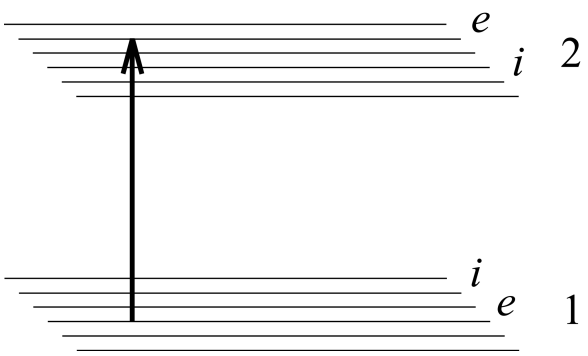

Figure 2.2: The two-electronic level molecule.

2.2.2 Particle imaging velocimetory (PIV)

Particle image velocimetry (PIV) is a non-intrusive measurement technique of flow visualization. Tracer particles ,which are seeded in the fluid, are assumed to follow the flow dynamics. The fluid with particles is illuminated by light source and the velocity field in the measurement plane is calculate the motion of the seeding particles. For PIV, pair of laser light are required. When a single frame that captures both exposures is used, the process called "auto–correlation" method. This method has a merit on temporal resolution. However, the direction of the flow is unclear since the first and the second exposures are not distinguishable is the frame. Alternatively, "cross–correlation " method uses two frames for each exposure.

In this section, the cross–correlation method to calculate two–dimensional (2D) velocity distribution from discrete images is described.

The images are split into interrogation areas, or windows. In each interrogation window, the correlation coefficient in any direction between the time intervals is calculated. To generate the correlation map, the interrogation window (from the first image) is shifted pixel by pixel over the search area (from the second image), and a correlation coefficient is calculated for each (m,n) shift according to the discrete formula:

$$\phi_{fg}(m,n) = \frac{\sum_k \sum_l f(k,l)g(k+m,l+n)}{\sum_k \sum_l f(k,l) \sum_k \sum_l g(k,l)} \tag{2.24}$$

Where f and g are the intensity values from the two frames obtained at t_0 and $t_0 + \Delta t$, respectively. Variables m and n are indices indicating the window offset. Iterating m and n over the entire correlation domain, a correlation map $\phi_{fg}(m,n)$ is generated. Calculating the offset of the correlation peak from the center of the domain gives the average distance (dx_{fg},dy_{fg}) the particles in the interrogation window traveled between frames. Dividing by the time interval Δt, the velocity vector of in the interrogation window (u_{fg},v_{fg}) can be obtained.

In practice, correlations are calculated via fast Fourier transforms (FFT) to enhance the computation speed [66]. Figure 2.3 shows a schematic of PIV algorithm with cross–correlation method using FFT. For the interrogation windows $f_(x, y)$ and $g_(x, y)$, Fourier coefficients $F_(k_x, k_y)$ and $G_(k_x, k_y)$ are computed. Then, the product Φ_{fg} are calculated as

$$\Phi_{fg} = F(k_x, k_y)G^*(k_x, k_y) \tag{2.25}$$

where $G^*(k_x, k_y)$ is the the complex conjugate of $G_(k_x, k_y)$. By Wiener–Khinchin theorem, applying inverse FFT to Φ_{fg}, the correlation coefficient in the physical field ϕ_{fg} can be obtained.

To improve the sub-pixel accuracy of the displacement estimation, three point Gaussian fit is used. The correlation coefficient distribution is fitted with a Gaussian function and the peak position is estimated with a sub–pixel resolution [66]. The estimated displacement (dx_{fg},dy_{fg}) will be as followings.

$$dx_{fg} = i + \frac{\ln c_{i-1,j} - \ln c_{i+1,j}}{2\left(\ln c_{i-1,j} + \ln c_{i+1,j} - 2\ln c_{i,j}\right)} \tag{2.26}$$

$$dy_{fg} = j + \frac{\ln c_{i-1,j} + \ln c_{i+1,j}}{2\left(\ln c_{i,j-1} + \ln c_{i,j+1} - 2\ln c_{i,j}\right)} \tag{2.27}$$

Here, (i,j) is the position at which the correlation coefficient has a maximum value, $c_{i,j}$.

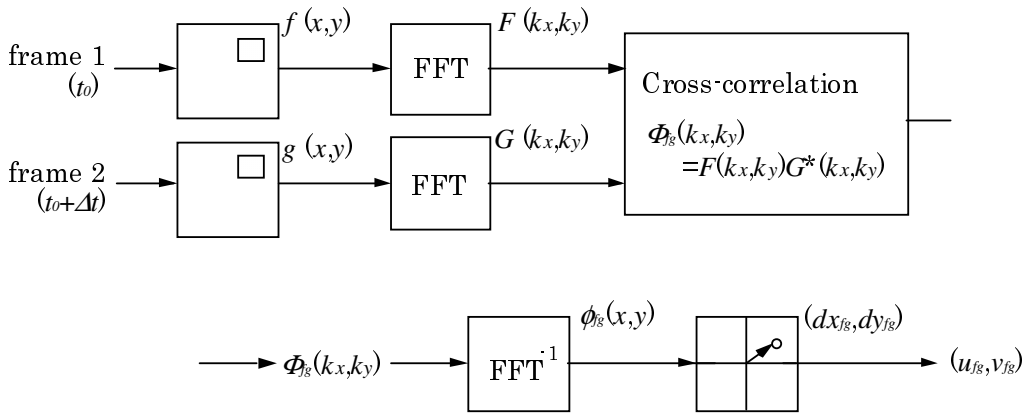

Figure 2.3: Schematic diagram of the high spatial resolution PIV algorithm.

High spatial resolution PIV algorithm

Since the size of the interrogation window is directory related to the spatial resolution, it has to be as small as possible to obtain high spatial resolution. On the other hand, the maximum particle displacement within the time interval Δt using the window size $X \times Y$ is approximately $X/4 \times Y/4$ [67] to minimize the effect of the particle pair loss. This poses the lower limit on the window size. Too small window size will then give spurious vector estimates in the region of the fast flow field. To achieve the high spatial resolution, especially in a flow field that has wide range of in velocity magnitude, processing algorithm which can estimate a large range of particles displacement using small interrogation windows, such as 2–step hierarchical method [68] and window–offset method [69], have been developed. In this study, high spatial resolution PIV algorithm developed by our previous study [70] based on the 2–step hierarchical method is used. It includes the elimination scheme of the spurious vectors and noises, which is established by a PIV simulation based on direct numerical simulation (DNS) of particle–laden homogeneous isotropic turbulence. The velocity vector at position (x, y) is calculated as follows,

1. The particle displacement $(dx_1(x, y), dy_1(x, y))$ is calculated by the cross–correlation method with a first interrogation window size that is enough large to capture particle displacement in the high velocity field. The overlap of the interrogation regions is introduced.

2. The spurious vectors and noises introduced into the velocity field by the first interrogation region are removed by applying a spatial low-pass filter (sharp cutoff filter). The cutoff filter width is selected to be the size of the first interrogation region.

3. The position of the interrogation window in the second frame is shifted by the displacement estimated by the first step $(g(x+dx_1(x, y), y+dy_1(x, y)))$, and the particle displacement $(dx_2(x, y), dy_2(x, y))$ is calculated by the cross–

correlation method with a second interrogation window size that corresponds to an appropriate spatial resolution. The interrogation regions are overlapped.

4. The spurious vectors and noises introduced into the velocity field by the second interrogation region are removed again by applying a spatial low-pass filter (sharp cutoff filter). The cutoff filter width is selected to be the size of the second interrogation region.

5. Finally, the velocity component $(u(x,y), v(x,y))$ is calculated as

$$u(x,y) = \frac{dx_1(x,y) + dx_2(x,y)}{\Delta t} \tag{2.28}$$

$$v(x,y) = \frac{dy_1(x,y) + dy_2(x,y)}{\Delta t} \tag{2.29}$$

2.2.3 Stereoscopic PIV

PIV is a two–dimensional two–components measurement. On the other hand, stereoscopic PIV is a two-dimensional three-component measurement using two cameras with separate viewing angles to extract the out-of-plane displacement component [71].

There are two basic configurations of stereoscopic PIV systems: the translation method (Fig. 2.4(a)) and the angular-displacement method (Fig. 2.4(b)). In the translation method, two cameras are arranged that their object planes, the lens planes, and the image planes are all parallel to each other and orthogonal to the light sheet [72]. In this method, the views of both cameras are common and it is possible for both cameras to focus an entire image plane. In the second configuration, called the angular-displacement method [71], two cameras locate at an arbitrary angle to the plane perpendicular to the object plane. In this method, it is more difficult to obtain well-focused images across the image plane since the object plane is not parallel to the lens plane. A simple way to focus the entire

image plane is increasing the depth of field (DOF), δz, which is given as [73]

$$\delta z = 4\left(1 + M_n^{-1}\right)^2 f^{\#^2}\lambda \tag{2.30}$$

where M is the camera magnification, $f_\#$ is the f-number and λ is the wavelength of the illuminating laser. This requirement either decreasing the magnification or increasing the f-number may cause a lack of image intensity. A second way to focus the entire image plane is applying Scheimpflug condition where the object plane, the lens plane and the image plane are collinear as shown in Fig.2.4(b).

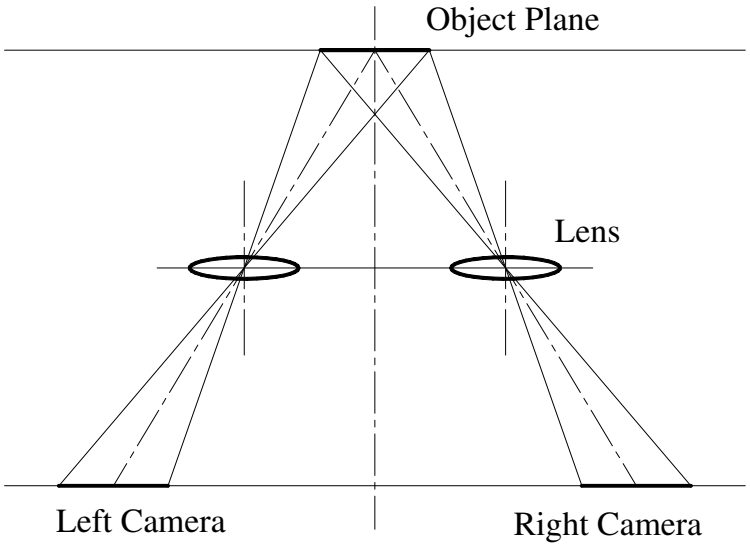

(a) Translation method

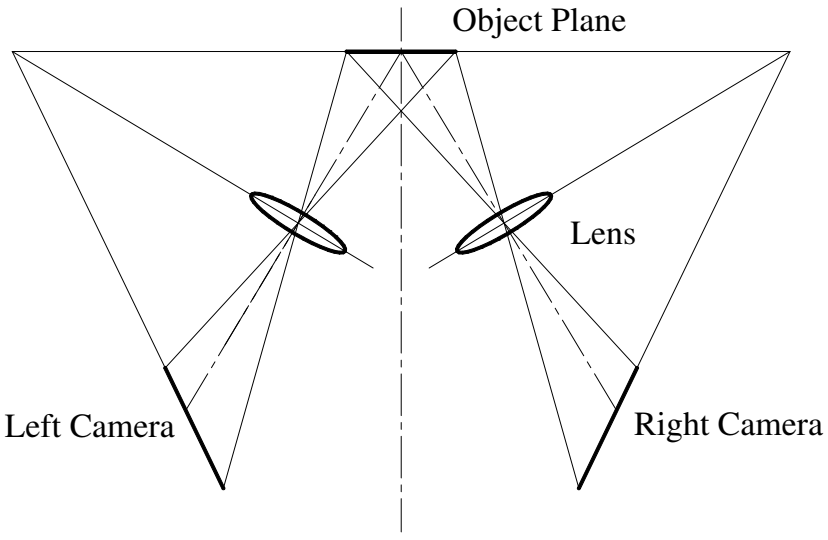

(b) Angular-displacement method

Figure 2.4: The basic configurations for stereoscopic PIV systems: (a) Translation method, (b) Angular-displacement method.

Sheimpflug condition

In this section, the Sheimpflug condition which can be used to obtain a well-focused image in the entire image plane is described [74]. As shown in Fig. 2.5, x axis is defined along to the lens plane and z axis along to the line-of-sight of the lens. The origin of the coordinate system is placed at the center of the lens, O. Any point $\mathrm{A}'(x_o, -z_o)$ in the object plane (O′C) will form an image at $\mathrm{A}''(-x_i, z_i)$ in the image plane (O"C) when their common point of intersection, C, also lies in the lens plane, OC. From Fig. 2.5, we have the following expressions:
For the object plane,

$$z_o = -x_o \tan\theta + d_o \tag{2.31}$$

For the image plane,

$$z_i = x_i \tan\alpha + d_i \tag{2.32}$$

where d_o and d_i are the nominal object and image distances, respectively. In the above expressions, d_o, d_i, θ, and α are all positive quantities.

Here, $\triangle \mathrm{OA}'\mathrm{B}'$ and $\triangle \mathrm{OA}''\mathrm{B}''$ are similar,

$$\frac{x_o}{z_o} = \frac{x_i}{z_i} \tag{2.33}$$

Using Eqs. (2.31 - 2.33),

$$\frac{1}{z_o} + \frac{1}{z_i} = \frac{1}{d_o} + \frac{1}{d_i} \left(= \frac{1}{f} \right) \tag{2.34}$$

which is the condition that particle images will be in sharp focus in the image plane, f being the focal length of the lens. The local magnification $-z_i/z_o$ varies across the image plane and only equals the nominal magnification $M = d_i/d_o$ for $x_o = x_i = 0$.

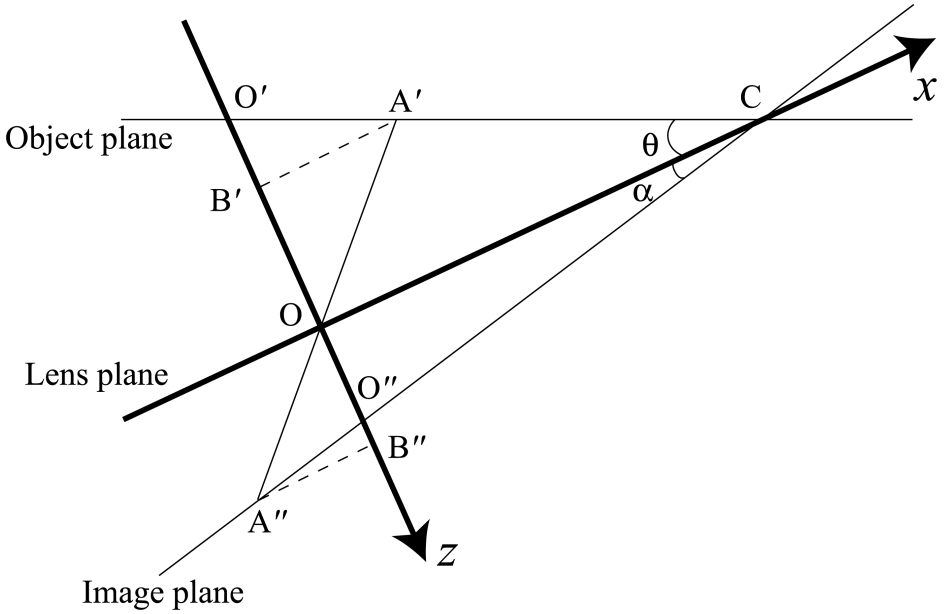

Figure 2.5: Schematic of Scheimpflug condition

Image correction methods

Scheimpflug condition causes significant non-uniformity in the local magnification across the image plane as shown in the previous section. However, the non-uniformity can be accounted for by using the mathematical manipulations [75].

There are several ways to reconstruct three components of velocity from the two pair of particle images. There are two different processes: (i) geometric reconstruction, and (ii) calibration–based reconstruction. As it will be described later, geometry of recording configurations is required to be completely known and mathematically modeled in the geometric reconstruction. On the other hand, calibration–based reconstruction requires calibration precedes and simplifies geometric reconstruction. As a result, it allows the recording devices locate more flexibly. Calibration–based reconstruction can be further classifies as 2D and 3D calibration based reconstruction. In the 3D calibration based reconstruction, knowledge of system geometry is unnecessary.

In this section, these reconstruction methods are summarized except for the 3D calibration based reconstruction since it is not used in this study. In the geometric reconstruction, to project the displacements from the image plane (X, Y) to the object plane (x, y) the following mapping function f is needed:

$$(x, y) = f(X, Y) \tag{2.35}$$

Figure 2.6 shows a schematic of the geometric reconstruction in the angular-displacement method without Scheimpflug condition, that is, image plane and lens plane are parallel to each other. A point on the image plane (X, Y) can be mapped on to the object plane (x, y) by,

$$x = \frac{SX}{L\cos\theta - X\sin\theta} \tag{2.36}$$

$$y = \frac{SY\cos\theta}{L\cos\theta - X\sin\theta} \tag{2.37}$$

Here, S is the distance between the origin of the object plane and lens plane, L is the distance between image plane and lens plane. In the angular-displacement

method, non-uniform magnification can be corrected in a coordinate $X'Y'$ as follows,

$$X' = \frac{L}{S}x = \frac{LX}{L\cos\theta - X\sin\theta} \tag{2.38}$$

$$Y' = \frac{L}{S}y = \frac{LY\cos\theta}{L\cos\theta - X\sin\theta} \tag{2.39}$$

One needs to input S, L and θ of both sensors accurately in the geometric reconstruction as shown in Eq. (2.38) and (2.39).

On the other hand, 2D calibration provides a mapping function between the 2D object plane and each 2D image plane using calibration grid. An advantage of the calibration–based reconstruction is that it can also correct optical aberration. The calibration data for each camera is

$$(x_i, y_i) = f(X_i, Y_i) \tag{2.40}$$

where (x_i, y_i) and (X_i, Y_i) are corresponding points on the object and image planes respectively. The calibration grid, a thin overhead projector transparency with black line rulings at a 5 mm square spacing, is placed inside the light sheet. A center of the target is indicated by a black dot as shown in Fig. 2.7(a). At first, to detect the location of intersection of the rulings (X_i, Y_i) and the center point (X_0, Y_0) , the calibration grid images are cross–correlated with a binary correlation mask. The correlation masks are numerically generated cross for the position of the line crossings, and cross plus dot for that of the origin, respectively. The grid points and the center point in the calibration image can be found as correlation peaks. Once the center point is detected, it can be related to the origin in the object coordinate $(x_o, y_o) = (0, 0)$. The adjacent 4 points are then, $(x_{\pm1}, 0) = (\pm0.5, 0)$ and $(0, y_{\pm1}) = (0, \pm0.5)$. All grid points can be related to the image plane coordinate, iteratively.

A first order mapping is

$$X_i = M_x X_o + C_x \tag{2.41}$$

$$Y_i = M_y Y_o + C_x \tag{2.42}$$

where M and C are the magnification and shift respectively. The first order mapping cannot correct non-uniform magnifications and other non-linearity such as an optical aberration. In this study, a second order mapping

$$X_i = a_1 X_o^2 + a_2 Y_o^2 + a_3 X_o Y_o + a_4 X_o + a_5 Y_o + a_6 \tag{2.43}$$

$$Y_i = b_1 X_o^2 + b_2 Y_o^2 + b_3 X_o Y_o + b_4 X_o + b_5 Y_o + b_6 \tag{2.44}$$

is employed. The coefficient $a_1, a_2, \ldots, a_6$ and $b_1, b_2, \ldots, b_6$ can be determined using a least square solution.

The particle images for both cameras are corrected by the mapping function Eq. (2.43 and 2.44), and the particle displacements are calculated with the PIV algorithm described in Sec. 2.2.2.

In this study, the 2D calibration method is also applied to PLIF images to correct optical aberration. Since lenses of the image intensifier are subject to a distortion, a third order mapping

$$\begin{aligned} X_i = a_1 X_o^3 + a_2 Y_o^3 + a_3 X_o^2 Y_o + a_4 X_o Y_o^2 + a_5 X_o^2 \\ + a_6 Y_o^2 + a_7 X_o Y_o + a_8 X_o + a_9 Y_o + a_1 0 \end{aligned} \tag{2.45}$$

$$\begin{aligned} Y_i = b_1 X_o^3 + b_2 Y_o^3 + b_3 X_o^2 Y_o + b_4 X_o Y_o^2 + b_5 X_o^2 \\ + b_6 Y_o^2 + b_7 X_o Y_o + b_8 X_o + b_9 Y_o + b_1 0 \end{aligned} \tag{2.46}$$

is employed.

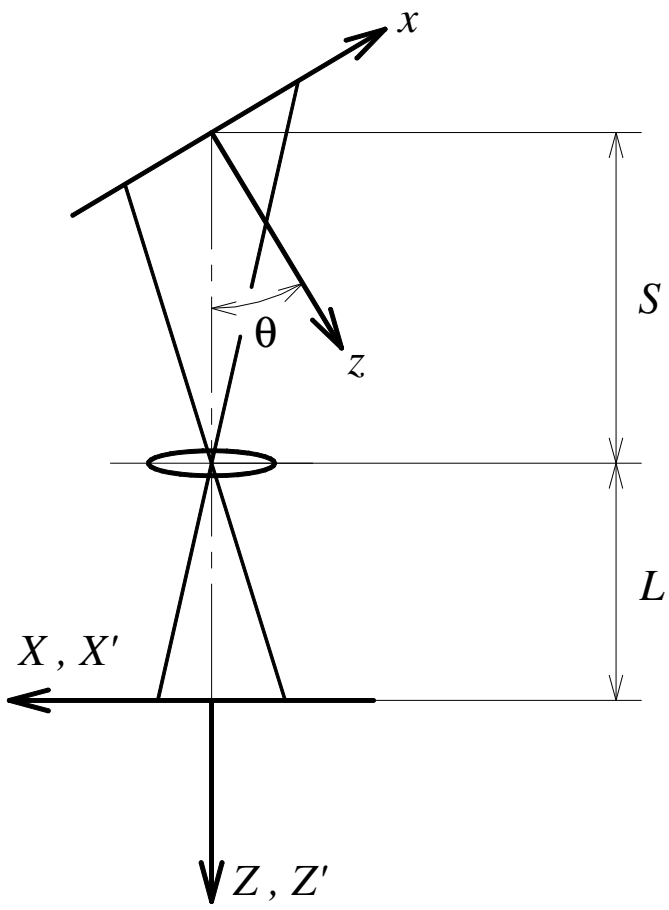

Figure 2.6: Schematic of the geometric reconstruction in the angular-displacement method without Scheimpflug condition

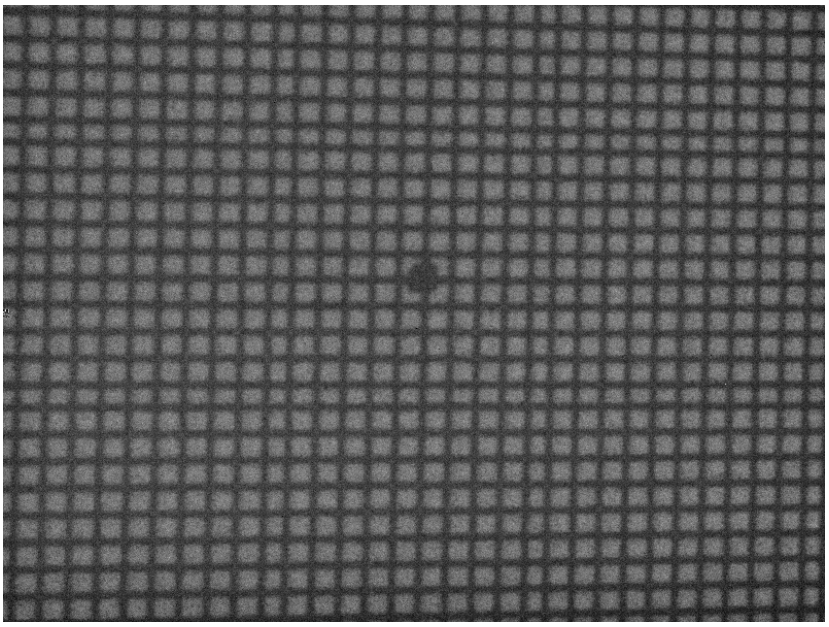

(a) A grid image taken with Scheimpflug condition

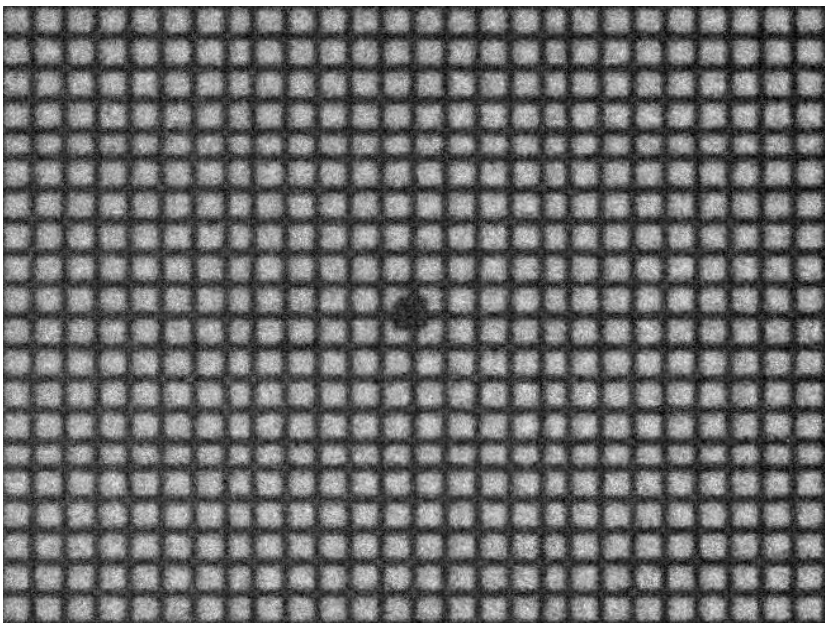

(b) A corrected image by 2D calibration method

Figure 2.7: Grid image

Reconstruction methods

In this section, the geometric relationship between the true particle displacements (dx, dy, dz) and the apparent displacements measured by left $(dx_{\mathrm{L}}, dy_{\mathrm{L}})$ and right $(dx_{\mathrm{R}}, dy_{\mathrm{R}})$ cameras are presented. In this study, two cameras are placed on either side of the light sheet. Because scattering efficiency is significantly higher in forward scatter, both views can have high and equal signal intensity [76]. Figure 2.8 shows the stereoscopic relationship between lenses, the position of a particle and the projection plane.

Setting O as a coordinate origin, L and R denote the center of the left and right lenses, A and B is the position at time t and $t + \Delta t$, respectively. A_i and B_i $(i = \mathrm{L}, \mathrm{R})$ denote the projected position on the left and right cameras. These points can be denoted with the vector expression as:

$$\overrightarrow{\mathrm{OA}} = \begin{pmatrix} x \\ y \\ z \end{pmatrix}, \quad \overrightarrow{\mathrm{OB}} = \begin{pmatrix} x + dx \\ y + dy \\ z + dz \end{pmatrix}, \quad \overrightarrow{\mathrm{OL}} = \begin{pmatrix} x_0 \\ 0 \\ -L \end{pmatrix}, \quad \overrightarrow{\mathrm{OR}} = \begin{pmatrix} x_0 \\ 0 \\ L \end{pmatrix} \tag{2.47}$$

where L and x_o are the distance between the center of the lenses and x and z axis, respectively. Therefore,

$$\overrightarrow{\mathrm{LA}} = \begin{pmatrix} x - x_0 \\ y \\ z + L \end{pmatrix}, \quad \overrightarrow{\mathrm{RA}} = \begin{pmatrix} x - x_0 \\ y \\ z - L \end{pmatrix} \tag{2.48}$$

Using Eqs. (2.47), (2.48), the projected position of the particle on the left and

right cameras can be as follows:

$$\begin{aligned}\overrightarrow{\mathrm{OA_L}} &= \overrightarrow{\mathrm{OL}} + k\overrightarrow{\mathrm{LA}} = \begin{pmatrix} x_0 + k(x - x_0) \\ ky \\ -L + k(z + L) \end{pmatrix} \\ &= \begin{pmatrix} x_0 + \dfrac{L}{L + z}(x - x_0) \\ \dfrac{L}{L + z} y \\ 0 \end{pmatrix} = \begin{pmatrix} x_L \\ y_L \\ 0 \end{pmatrix} \end{aligned} \tag{2.49}$$

$$\begin{aligned}\overrightarrow{\mathrm{OA_R}} &= \overrightarrow{\mathrm{OR}} + k\overrightarrow{\mathrm{RA}} = \begin{pmatrix} x_0 + k(x - x_0) \\ ky \\ L + k(z - L) \end{pmatrix} \\ &= \begin{pmatrix} x_0 + \dfrac{L}{L - z}(x - x_0) \\ \dfrac{y}{L - z} \\ 0 \end{pmatrix} = \begin{pmatrix} x_R \\ y_R \\ 0 \end{pmatrix} \end{aligned} \tag{2.50}$$

From Eqs. (2.49), (2.50), a mapping function from projected plane to the actual position of the particle is

$$\begin{pmatrix} x \\ y \\ z \end{pmatrix} = \begin{pmatrix} x_0 + \dfrac{2(x_\mathrm{R} - x_0)(x_\mathrm{L} - x_0)}{x_\mathrm{R} + x_\mathrm{L} - 2x_0} \\ \dfrac{2y_\mathrm{R}y_\mathrm{L}}{y_\mathrm{R} + y_\mathrm{L}} \\ \dfrac{x_\mathrm{R} - x_\mathrm{L}}{x_\mathrm{R} + x_\mathrm{L} - 2x_0} L \end{pmatrix} \tag{2.51}$$

By taking the partial derivative of Eq. (2.51), 3D displacements (dx, dy, dz) can be obtained.

$$\begin{pmatrix} dx \\ dy \\ dz \end{pmatrix} = \begin{pmatrix} \dfrac{2\{(x_\mathrm{L} - x_0)^2 dx_\mathrm{R} + (x_\mathrm{R} - x_0)^2 dx_\mathrm{L}\}}{\{(x_\mathrm{R} - x_0) + (x_\mathrm{L} - x_0)\}^2} \\ \dfrac{2({y_\mathrm{L}}^2 dy_\mathrm{R} + {y_\mathrm{R}}^2 dy_\mathrm{L})}{(y_\mathrm{R} + y_\mathrm{L})^2} \\ \dfrac{2\{(x_\mathrm{L} - x_0) dx_\mathrm{R} + (x_\mathrm{R} - x_0) dx_\mathrm{L}\}}{\{(x_\mathrm{R} - x_0) + (x_\mathrm{L} - x_0)\}^2} L \end{pmatrix} \tag{2.52}$$

Dividing Eq. (2.52) by the time interval Δt, 3 components of velocity (u, v, w) can be obtained.

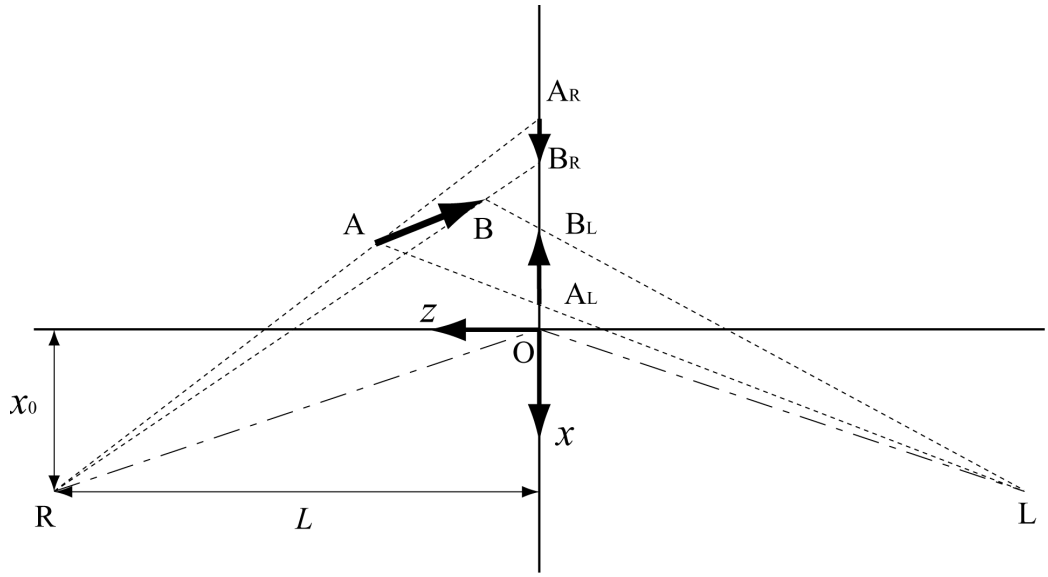

Figure 2.8: Geometric description used for reconstruction of the 3D displacement vector in forward scattering mode.

2.3 Measurement techniques

In this study, high repetition rate simultaneous CH–OH PLIF system is developed to investigate local flame structure and flame dynamics in turbulent combustion. The measurement setup will be described in Sec. 2.3.1. The time–resolved stereoscopic PIV, which is developed in our previous study [77] will be described in Sec. 2.3.2. Combining these measurement techniques, kHz measurement system consists of two laser-based measurement systems, PLIF for OH and CH detection and stereoscopic PIV, is developed. The schematic diagram of the measurement system for the high repetition rate simultaneous CH–OH PLIF and stereoscopic PIV is shown in Fig. 2.9. The measurement system comprises high-speed lasers, cameras and image intensifiers as shown in Fig. 2.10.

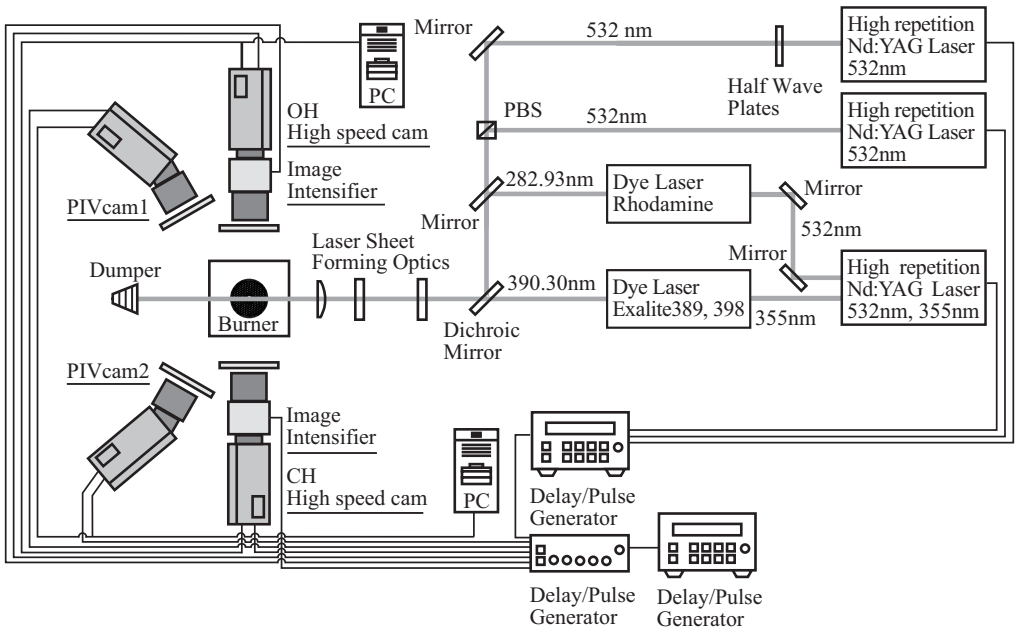

Figure 2.9: Schematic diagram of the high repetition rate simultaneous CH–OH PLIF and stereoscopic PIV measurement.

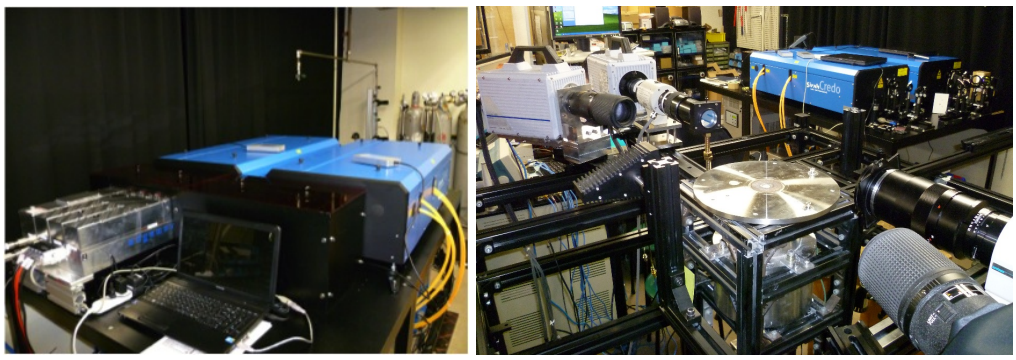

Figure 2.10: Photos of the high repetition rate simultaneous CH–OH PLIF and stereoscopic PIV measurement system.

2.3.1 High repetition rate simultaneous CH–OH PLIF

In high repetition rate CH PLIF measurements, the $Q_1(7,5)$ transition of the $B^2\Sigma^-$-$X^2\Pi(0,0)$ band at 390.30 nm is excited and fluorescence from the A-$X(1,1),(0,0)$ and B-$X(0,1)$ bands between 420 and 440 nm is detected. In OH PLIF, the $Q_1(7)$ transition of the $A^2\Sigma^-$-$X^2\Pi(1,0)$ band at 282.93 nm is excited and fluorescence from the A-$X(1,1),(0,0)$ and B-$X(0,1)$ bands between 306 and 320 nm is detected. The laser system consists of an Nd:YAG laser (Edge-wave, HD-40-III) and two dye lasers (Sirah, Credo) for high repetition pumping. A laser module converts the fundamental output of the Nd:YAG laser to the third (355 nm) and second (532 nm) harmonic wavelengths, which are independently and simultaneously emitted at 6 and 5 mJ/pulse, respectively. The dye lasers are pumped by the laser beams emitted from the Nd:YAG laser. A blend dye of Exalite 389 and Exalite 398 in p-dioxane solvent is used for CH and Rhodamine 6G for OH.

At 10 kHz, the pulse energies of the 390 and 283 nm laser are 0.60–0.80 and 0.16–0.20 mJ/pulse, respectively. According to the dye laser specifications, the full divergence angle of the laser beam and the shot-to-shot laser energy variation are 500 μradians and 5 % rms, respectively.

The separate laser beams are guided to the same axis by a dichroic mirror, and then expanded by sheet forming optics, comprising several plano-convex and -concave lenses. The collection devices are positioned perpendicular to the laser sheet. The CH radical fluorescence is collected by a 100 mm f/2.0 lens (Carl Zeiss, Macro Planar T*2/100 ZF) fitted with a band pass filter (Semrock, FF01-434/17-25) to block flame radiation and particle-scattered light, and is imaged onto an image intensifier (Hamamatsu Photonics, C10880-03F). The amplified images are detected by a high-speed camera (Photron, SA-X, 1024×888 pixels at $10,000$ fps). The OH radical fluorescence is collected by a 105 mm f/4.5 UV lens (Nikon, UV-Nikkor) with a band pass filter (Semrock, FF01-320/40-25) and imaged onto an image intensifier (Hamamatsu Photonics, C6534). The amplified

images are detected by a high-speed camera (Photron, SA-5, 896×704 pixels at $10,000$ fps).

Because the laser intensity is non-uniform, striped distributions appear in the vertical direction of the raw images. Because the fluorescence intensity does not saturate in this measurement, the PLIF signal directly depends on the incident laser intensity. Therefore, images are corrected by the distribution of the mean OH fluorescence intensity. However, the correction of the CH PLIF images is precluded by the large shot noise.

2.3.2 Time–resolved stereoscopic PIV

The laser system for time-resolved Stereoscopic PIV consists of two high-repetition-rate Nd:YAG lasers (Lee Laser, LDP-100MQG). At 10 KHz, the maximum power of these lasers is 50 W. Two independent single pulse lasers are combined to make double pulse laser beam with high pulse energy. Polarization of the laser beams, which are emitted with short time difference, are originally vertical. One of them is rotated 90° by half wave plates (CVI Laser). They are combined in the same axis by polarizing beam splitter (CVI Laser) and become double-pulsed beam. The double-pulsed beams are expanded by the laser sheet optics.

These double-pulsed beams illuminate the measurement region. The scattered light by the tracer particles is recorded by two high-speed cameras (Photron, SA-5) with equipping a macro lens (Nikon, Micro-Nikkor 200mm $\mathrm{f}/4$), placed at $\pm 20.0^\circ$ to capture stereoscopic pairs of particle images, and the Scheimpflug condition described in Sec. 2.2.3 is applied. Both cameras record 736×448 pixels images at $20,000$ fps. The cameras are fitted with 532 nm band-pass filters (Shonan Optical Thin Film Laboratories, 532 nm). The tracer particles are 1.0-μm-diameter SiO_2 particles.

2.4 Simultaneous CH–OH PLIF and stereoscopic PIV

2.4.1 Experimental apparatus and conditions

The developed measurement is applied to the methane-air turbulent jet premixed flames shown in Fig. 2.11(a). This burner has a main jet nozzle and a surrounding nozzle for flame holding. The inner diameters of the main and surrounding nozzles are 10 and 60 mm, respectively.

In this study, high repetition rate measurements are conducted for three jet velocities: $U_0 = 10, 15$ and 20 m/s ($Re_D = 6667, 10,001$ and $13,333$, respectively), where Reynolds number Re_D is computed from the nozzle inner diameter (D) and the mean axial velocity at the jet exit. The equivalence ratio of the main and surrounding flame is fixed at 1.0 and 0.86, respectively. Figure 2.11(b) shows a photograph, CH chemiluminescence and OH fluorescence images of the turbulent jet premixed flame. Measurements were conducted at axial distances of $x/D = 5, 7, 8$ and 10, which are indicated by gray dotted lines in Fig. 2.11(b). Here, x is the distance from the jet exit. The turbulence characteristics obtained at the center of the measurement region are summarized in Table 2.1. The velocity fluctuation are measured by a hot-wire constant temperature anemometer with an X-probe (Kanomax Japan, Model0250R, tungsten $\Phi = 5$ μm) preliminary for inert flow and turbulence properties are estimated by adopting Taylor's hypothesis. In this table, l, λ and η denote the integral length scale, Taylor micro scale and Kolmogorov length scale, respectively. Re_λ denotes the Reynolds number computed from λ and u'_{rms}. δ_F is a laminar flame thickness and S_L is a laminar burning velocity. These conditions are classified into corrugated flamelets regime and on the border with thin reaction zones regime in the turbulent combustion diagram by Peters [5], which is shown in Fig. 2.12.

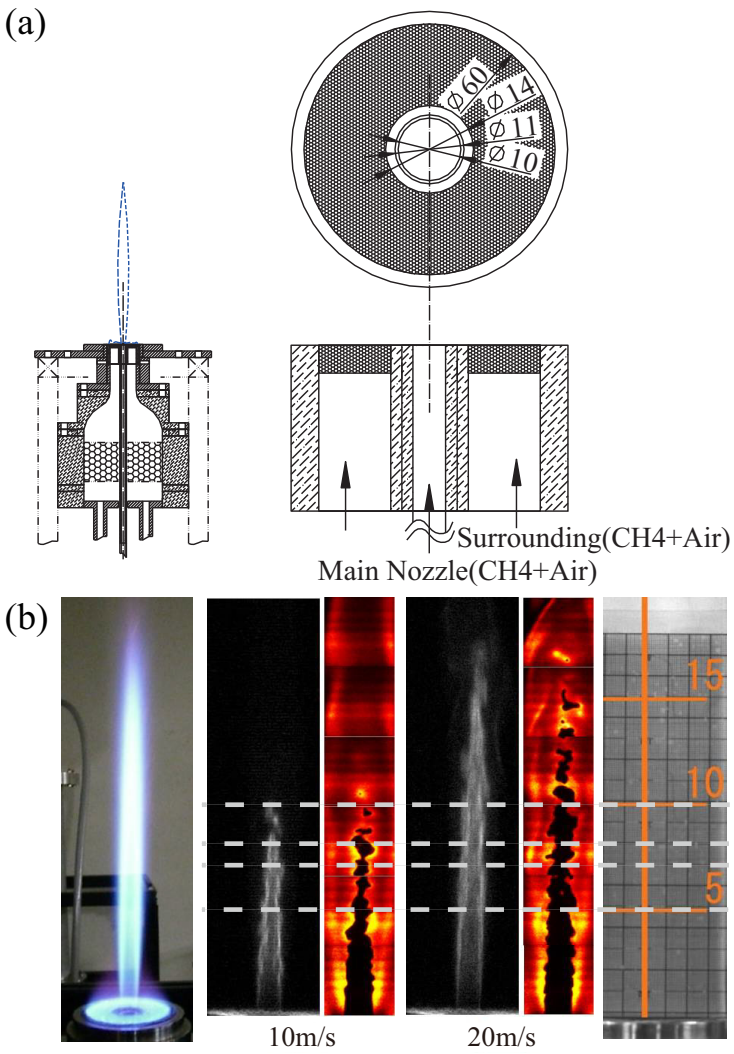

Figure 2.11: (a) Schematic of a turbulent jet burner and (b) a photograph, CH chemiluminescence images and OH fluorescence images of turbulent jet premixed flame.

Table 2.1: Turbulence characteristics of experimental conditions.

U_0 [m/s]	x/D	Re_D	Re_λ	U_m [m/s]	u'_{rms} [m/s]	l [mm]	λ [mm]	η [μm]	l/δ_{F}	$u'_{\mathrm{rms}}/S_{\mathrm{L}}$
10	5	6667	93.4	11.40	1.15	6.21	0.998	58.0	144.7	3.02
15	7	10001	173.1	14.74	2.12	11.65	1.006	42.9	271.4	5.56
20	8	13333	228.5	17.70	2.81	15.22	0.999	37.2	354.5	7.38
20	10	13333	256.8	14.49	2.87	18.83	1.100	38.6	438.6	7.53

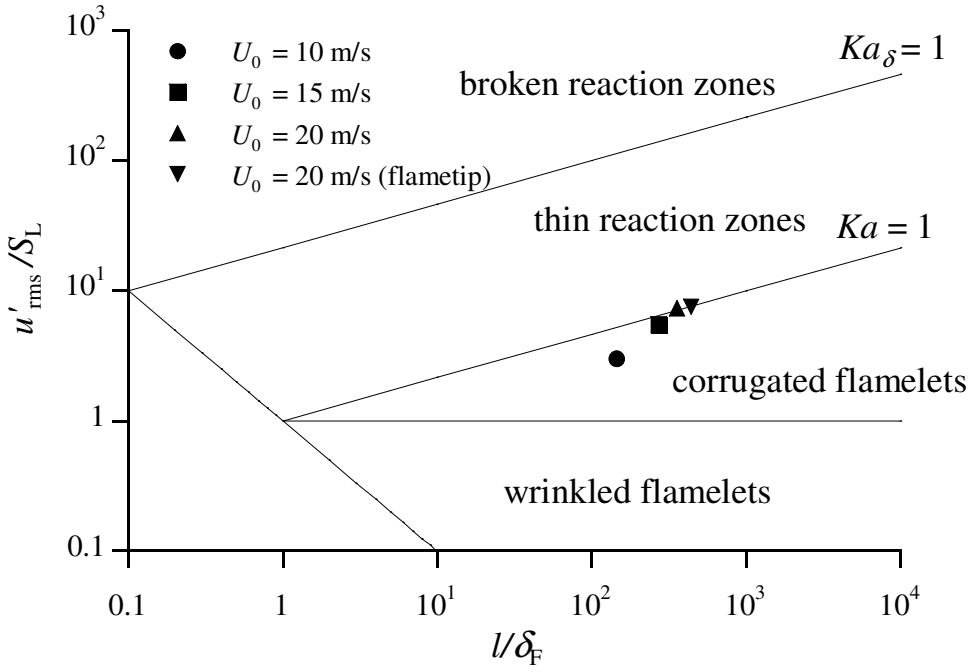

Figure 2.12: Measurement conditions of the present study on the combustion diagram by Peters.

2.4.2 Measurement conditions

The measurement conditions were then determined from the turbulent characteristics. The measurement regions of CH PLIF and OH PLIF were set to 62.7×52.7 and 55.5×44.6 mm, respectively, giving an approximate spatial resolution of 60 μm/pixels for both CH and OH PLIF. For SPIV, the camera resolution is determined to be 450×550 pixels over a 13.5×16 mm region, which means that the spatial resolution of PIV is 900 μm for a 30×30 pixel interrogation region. Since the velocity vectors are evaluated with 50% overlap, they were obtained at 450 μm intervals.

The intensity profile and position of each laser measured by a beam profiler (Ophir, FX-50) is shown in Fig. 2.13. The FWHM thicknesses of the laser sheets in CH and OH PLIF were approximately 400 μm; for the first and second lasers of SPIV they were approximately 800 μm and 500 μm, respectively. The peak positions of all laser sheets were separated by less than 100 μm.

Timing control

The timing of the simultaneous measurement is controlled by two delay generators (Stanford Research Systems, DG535 and DG645), a pulse generator (LabSmith, LC880) and the delay systems of image intensifiers. Figure 2.14 shows the timing diagram of simultaneous CH/OH PLIF and stereoscopic PIV measurement. After CH PLIF, OH PLIF is conducted with 25 ns ($= \Delta t_{PLIF}$) delay. To optimize signal-to-noise ratio, gate time of image intensifiers CH PLIF (Δt_{ECH}) and OH PLIF (Δt_{EOH}) are set to 180 ns. These PLIF measurements are conducted between the first and second frames for stereoscopic PIV. The time separation of PIV ranged from 6 to 9 μs. Thus, the inherent velocity uncertainty in sub-pixel interpolation was at most 0.33 m/s.

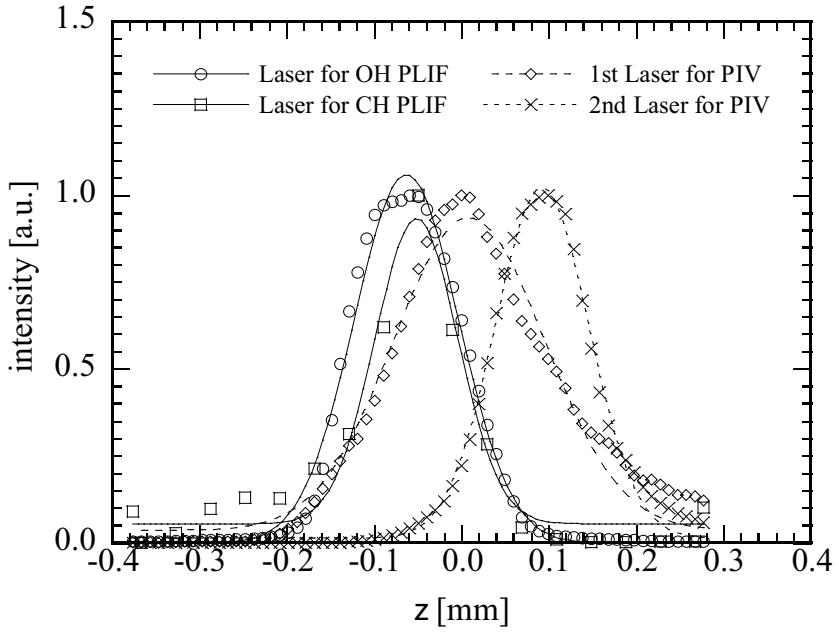

Figure 2.13: Intensity profile of laser sheets for CH, OH PLIF and stereoscopic PIV.

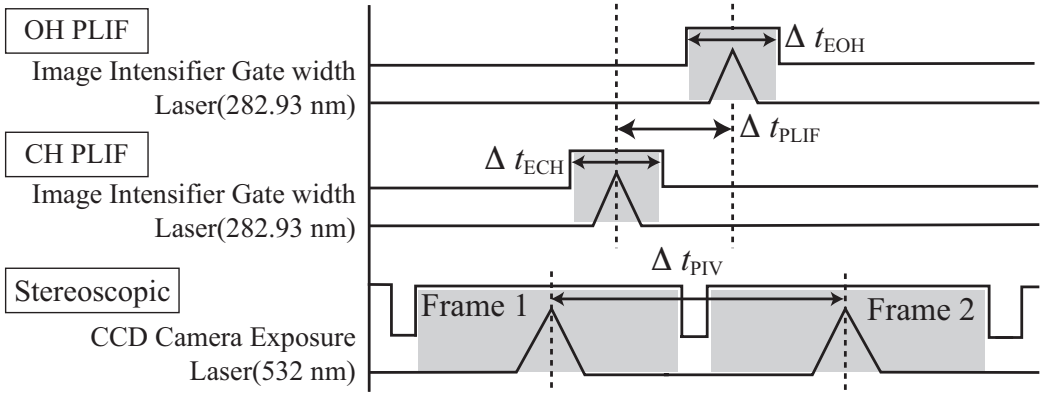

Figure 2.14: Timing diagram of the simultaneous measurement

2.4.3 Flame dynamics in turbulent jet

The representative PLIF images acquired by this system are shown in Figs.2.15–2.18. The illustrated area is approximately 13×13 mm. The quantized light intensity in the (a) OH images and (b) CH images is mapped from 0 (minimum) to 1 (maximum). Figures 2.15(c)–2.18(c) show distributions of fluctuating velocity. The arrows and background indicate the in-plane (x and y) and out-of-plane (z) component of the velocity fluctuation, respectively. The mean velocity distribution obtained from $10,000$ samples was subtracted from the instantaneous velocity. The largest vector corresponds to 2.3 m/s, 2.5 m/s, 3.2 m/s and 4.0 m/s in each condition (2.15(c)–2.18(c)), respectively.

The signal-to-noise ratios (SNRs) for PLIF measurement can be evaluated by the ratio of mean fluorescence intensity to r.m.s. of non-fluorescence region's intensity. The SNRs of CH PLIF images vary between 6 and 12 for each condition. They are between 13 and 18 for OH PLIF images. The mean SNRs for OH and CH PLIF images are approximately 15.1 and 8.8 respectively. Although SNR for each condition largely varies and the shot noise in the CH fluorescence distribution is significant, the simultaneous measurement can track temporal development of the flow and flame structure.

In the case of relatively low Reynolds number case ($U_0 = 10$ m/s), the unburned mixtures convect to downstream with continuous shape (Fig. 2.15). Isolate reactant pockets or entrainment of burnt gas in the unburned region is barely observed. Note that the time interval of each image is 200 μs since every two images are illustrated in this case, corresponding to a 5 kHz acquisition rate.

However, in the case of moderate Reynolds number ($U_0 = 15$ m/s, Fig. 2.16), the number of flame wrinkling increases and the flame front turns to exhibit a very complicated geometry. Due to the entrainment of burned gas in the unburned region, flame front sometimes appears to be disconnected. Between the disconnected unburned mixtures, the velocity field exhibits strong flow motion.

At $U_0 = 20$ m/s (Fig. 2.17), the unburned mixture in the main jet frequently di-

vides in two in the stream wise direction. The large scale turbulent structures in the downstream region are caused by Kelvin-Helmholtz instability of the shear layer. Consequently, large scale islands of unburned mixture are created and ejected into the downstream.

Figure 2.18 shows a typical sequence of the flame and flow structure observed around the flame tip ($x/D = 10$) for $U_0 = 20$ m/s. Note that the flow condition is that of Fig. 2.17 but measurements are taken further downstream. In this region, the continuous shape of the main jet flame is not observed. The large scale unburned mixture islands are split into many fine scale unburned mixtures. These fine scale unburned mixtures are expected to be consumed very rapidly; they may enhance the turbulent burning velocity of the entire jet flame.

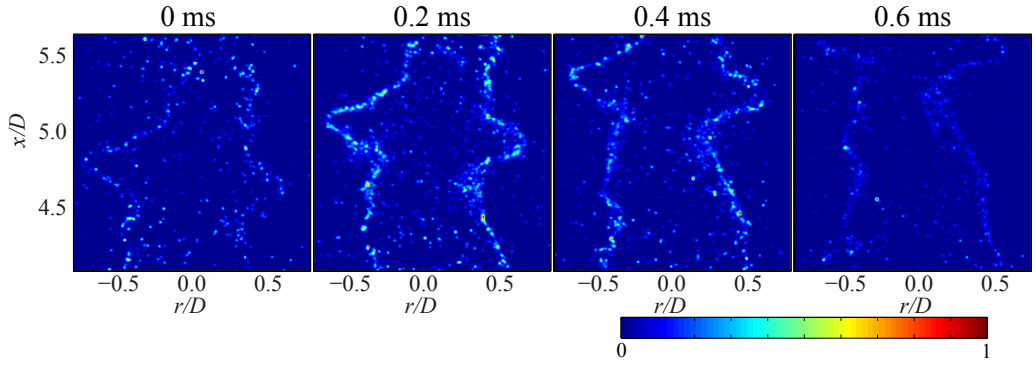

(a) CH PLIF images

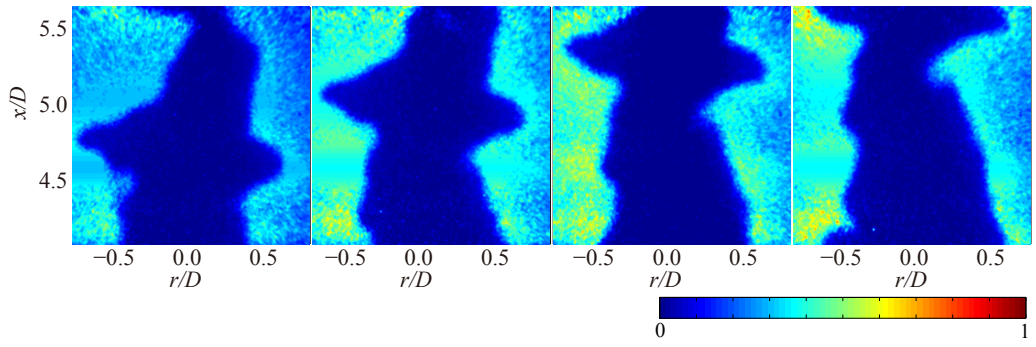

(b) OH PLIF images

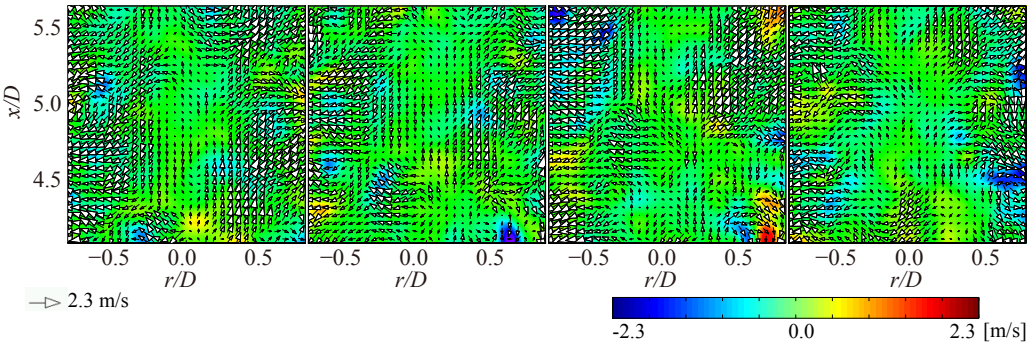

(c) Fluctuating velocity vector map images

Figure 2.15: Sequential CH–OH PLIF and PIV images in the case of low Reynolds number at $x/D = 5$ for $U_0 = 10$ m/s

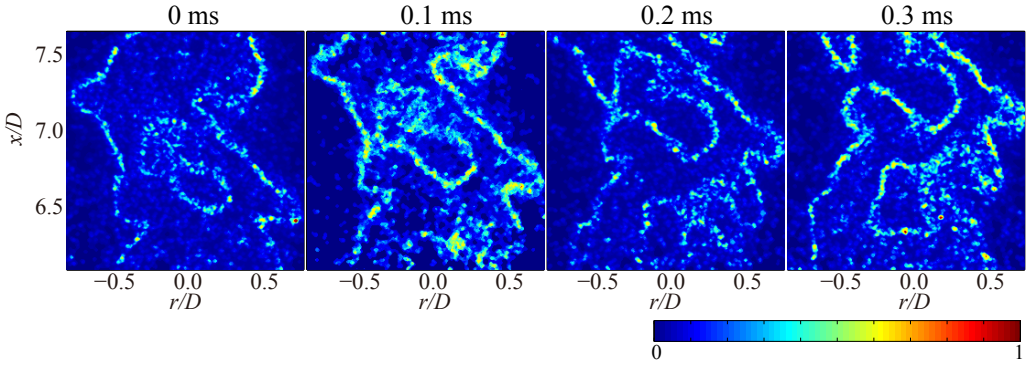

(a) CH PLIF images

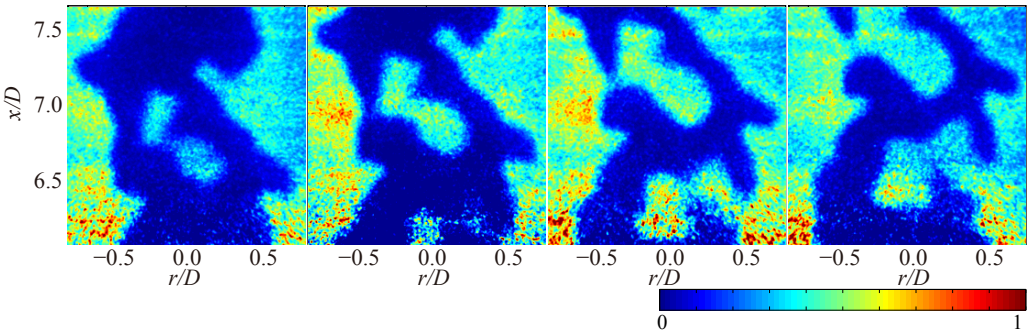

(b) OH PLIF images

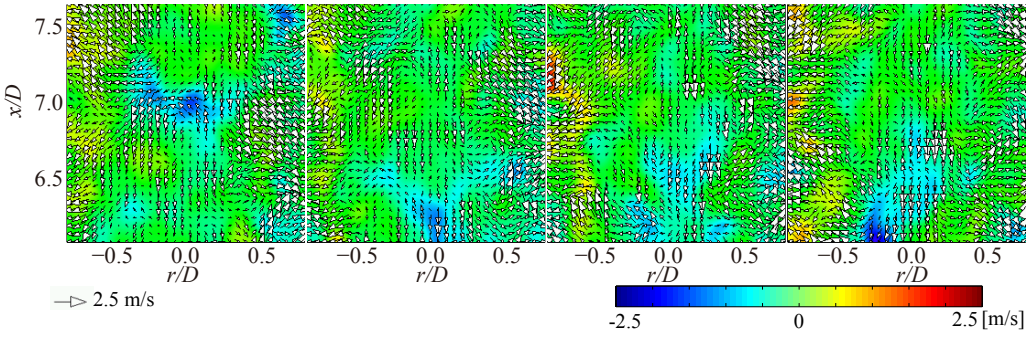

(c) Fluctuating velocity vector map images

Figure 2.16: Sequential CH–OH PLIF and PIV images in the case of moderate Reynolds number at $x/D = 7$ for $U_0 = 15$ m/s

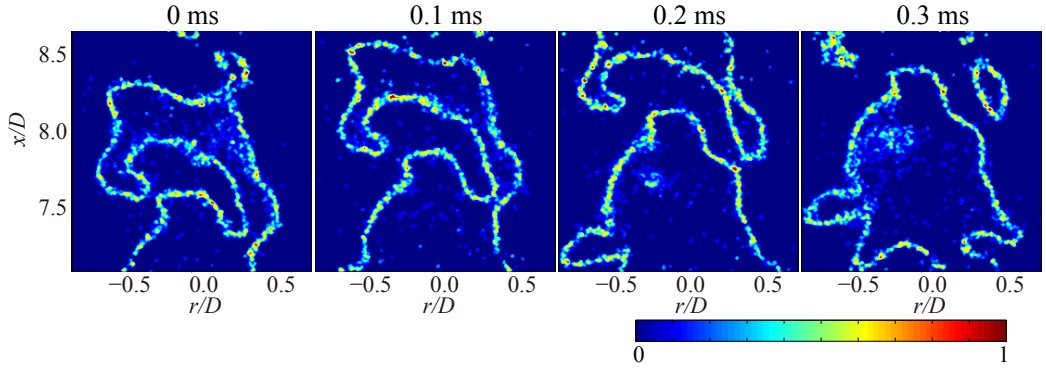

(a) CH PLIF images

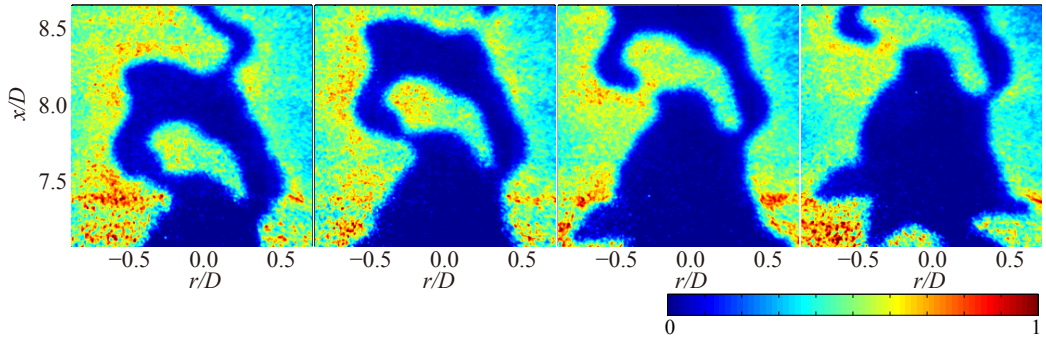

(b) OH PLIF images

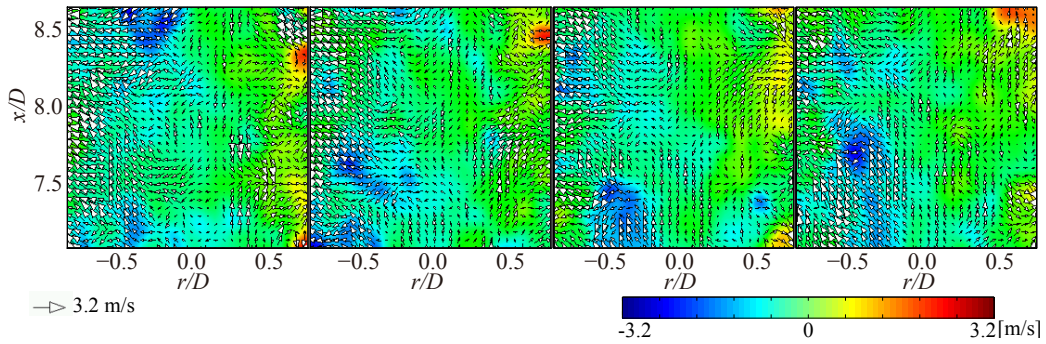

(c) Fluctuating velocity vector map images

Figure 2.17: Sequential CH–OH PLIF and PIV images in the case of high Reynolds number at $x/D = 8$ for $U_0 = 20$ m/s

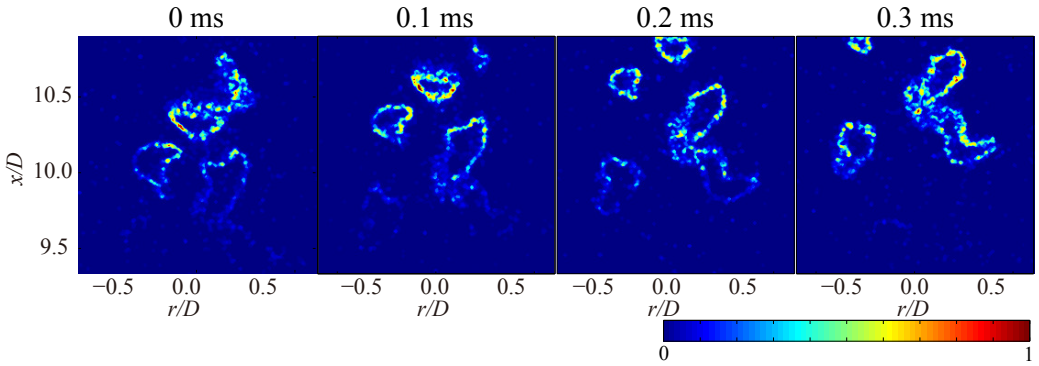

(a) CH PLIF images

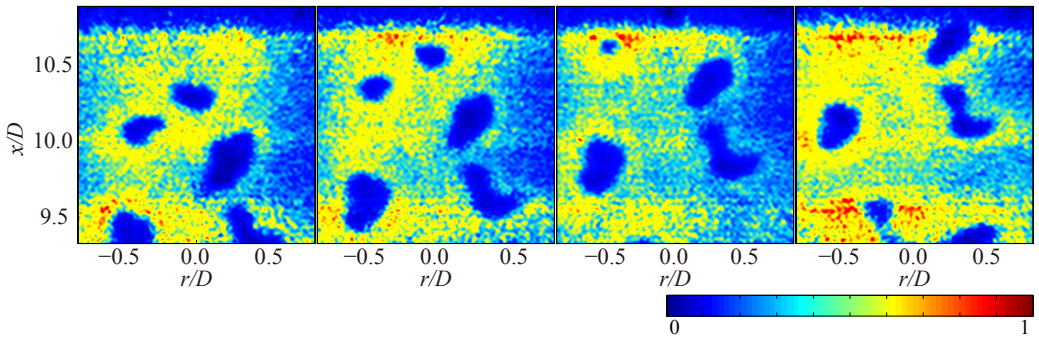

(b) OH PLIF images

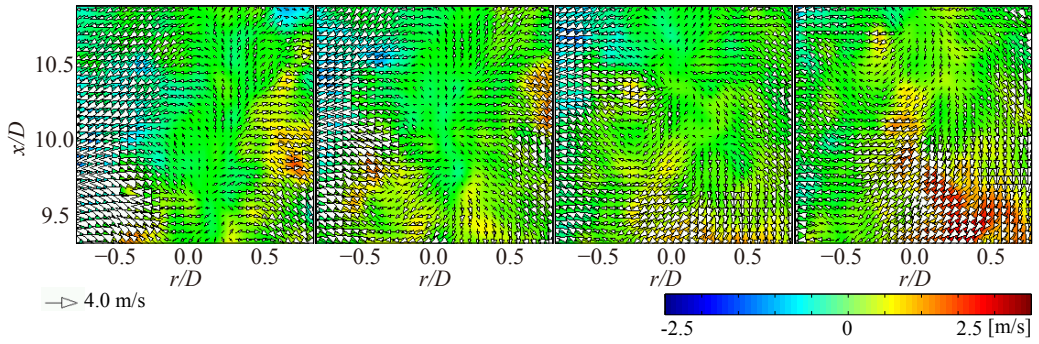

(c) Fluctuating velocity vector map images

Figure 2.18: Sequential CH–OH PLIF and PIV images in the case of high Reynolds number around flame tip at $x/D = 10$ for $U_0 = 20$ m/s

2.4.4 Unburned mixture detected in CH PLIF image

When sequential OH and CH PLIF images are observed simultaneously, some regions of unburned mixtures are detected only in the CH images. An example is presented in Fig. 2.19. In Figs. 2.19(a) and (c), small scale unburned mixture is detected in both OH and CH images (pink dotted circles). After 100 μs, the unburned mixture is observed in the CH image (Fig. 2.19(d)) but is absent at the same location in the OH image (Fig. 2.19(b)). The opposite phenomenon was rarely observed. This demonstrates the fundamental limitations of OH as a flame marker since OH PLIF are much more easily acquired than CH PLIF. Due to 3D geometry, the smaller the unburned mixture, the larger the flame surface area per unit volume. The unburned mixtures in such small structures are rapidly heated. Within these very small scale hot unburned mixtures, OH radicals may have been created while the CH fluorescence indicates that there is still unburned mixture and they are consumed with a significant heat release rate. This emphasizes the importance of obtaining the distributions of both CH and OH radicals.

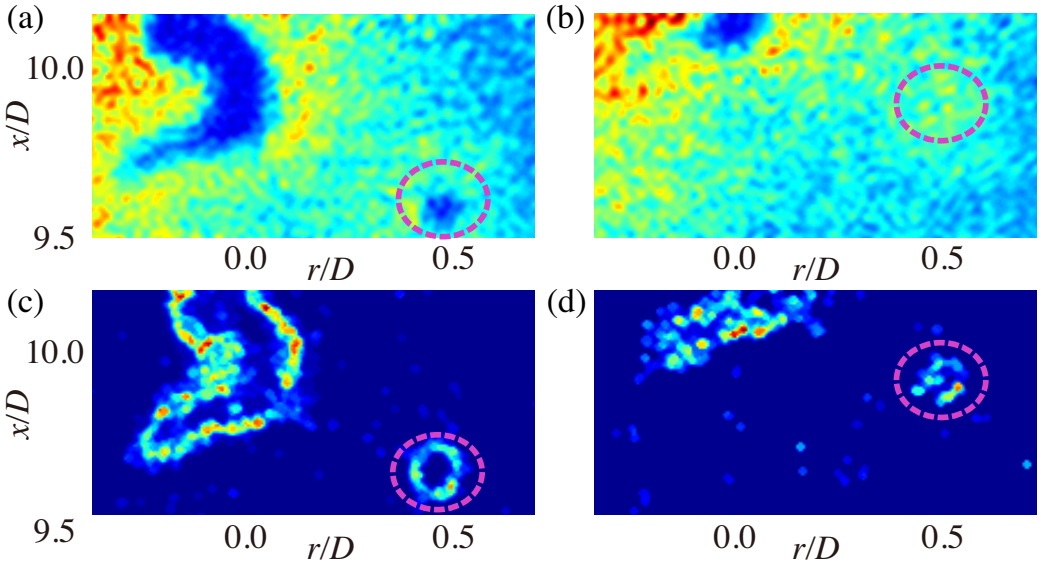

Figure 2.19: Example of fine scale unburned mixture that cannot be detected by OH PLIF measurement. (a) OH and (c) CH images for a first frame and (b) OH and (d) CH images for the subsequent frame.

2.5 Interim conclusions

In this chapter, high repetition rate simultaneous CH–OH PLIF and stereoscopic PIV with an acquisition rate of 10 kHz and a measurement duration exceeding 1.0 s has been developed. The obtained results are summarized as follows.

(1) With increasing the jet velocity, the number of flame wrinkling increases and the flame front turns to exhibit a very complicated geometry, leading to the creation of the large-scale unburned mixture islands in high Reynolds number turbulent jet premixed flame.

(2) The large-scale unburned mixture islands are split into many fine-scale unburned mixtures. These fine-scale mixtures are expected to be consumed very rapidly, they may enhance the turbulent burning velocity of the entire jet flame.

(3) When sequential OH and CH PLIF images are observed simultaneously in high Reynolds number turbulence, some regions of fine-scale unburned mixtures are detected only in the CH images.

(4) The developed high-speed measurement system based on simultaneous CH–OH PLIF and stereoscopic PIV can investigate flame and flow dynamics in turbulent combustion.

In the next chapter, the enhancement of the turbulent burning velocity due to the formation and rapid consumption of fine scale unburned mixtures will be investigated in more detail.

Chapter 3

Dominant flame structure and dynamics in the tip of the turbulent jet premixed flame

3.1 Introduction and objectives

In Chap. 2, the formation and rapid consumption of fine-scale unburned mixtures have been observed around the flame tip of the turbulent jet. The formation of unburned mixture caused by vortex–flame interaction has been shown in a numerical simulation [78] and in an experiment [79] by imposing high stretch on the laminar flame. Not only in simple laminar flames, the formation of isolated pocket has been also observed in turbulent flames, for example, at the tip of a Bunsen flame [80, 81] and turbulent jet premixed flame [82]. The fine-scale unburned mixtures are also observed in a 3D DNS of an H_2-air turbulent plane jet premixed flame [83]. Thermo–diffusive process has a different effect on the local flame structure because the Lewis number of the H_2-air mixture differs from that of CH_4-air mixture in the present case. However, they found that the fine scale eddies near the flame front were related to the unburned mixtures at the flame tip.

These fine-scale mixtures are consumed very rapidly, thickening the flame blush at the flame tip. Consequently, they may enhance the turbulent burning velocity of the entire jet flame. In SGS combustion model, turbulent burning velocity

(S_T) is modeled with the flamelet assumption, where the effect of turbulence is to wrinkle the thin reaction layers. The local structure retains characteristics of a laminar flame. The increase in S_T is accounted for by the increase of the flame surface area. The recent 3D DNSs [84–86], have revealed the characteristics of turbulent premixed flames and local flame structures that are hardly expected from theoretical classifications based on flamelet concept. Nada et al. [85] reported that 3D flame structures, which are caused by strong fine scale eddies in turbulence, appear even in the laminar flamelet regime from DNS of a freely propagating H_2-air turbulent premixed flame. Since the flame–turbulence interaction has not been fully clarified yet, the turbulent burning velocity especially in high Reynolds number turbulence has to be investigated.

In this chapter, the contribution of fine-scale unburned mixtures to enhance the turbulent burning velocity is investigated by evaluating the local consumption rate. After showing that the formation and the rapid consumption of the fine-scale unburned mixtures are dominant phenomena around the flame tip in Sec.3.2.1, the size and local consumption rate is statistically analyzed in Sec.3.3.

3.2 Dominant flame structure in turbulent jet

3.2.1 Proper orthogonal decomposition (POD) analysis

To investigate the dominant structure of the turbulent jet premixed flame, proper orthogonal decomposition (POD) analysis is introduced in this study. In POD, series of data is decomposed, using some mathematical tools, into a set of orthogonal basis functions in the most "optimal" way. POD is based on energy considerations. If a field has energetic structures that systematically appear, they will be captured in POD modes. The relative contribution of a given POD mode to the overall energy is represented by POD eigenvalues.

POD was first introduced by Lumley [87]. The basic idea of the POD is to express the fluctuating part with a linear combinations of POD modes ϕ^i and time

varying modal coefficients a_i,

$$\boldsymbol{x}^n = \bar{\boldsymbol{x}} + \sum_{i=1}^{N} a_i^n \phi^i. \tag{3.1}$$

When time-series data are given as

$$\boldsymbol{x}(t) \in \mathbb{R}^n; t_{min} < t < t_{max}. \tag{3.2}$$

POD eigenvalues, λ, and eigenvectors, ϕ can be derived as follows

$$\boldsymbol{R}\varphi_k = \lambda_k \varphi_k; \lambda_1 \geq \ldots \lambda_n \geq 0. \tag{3.3}$$

Here $\boldsymbol{R}$ is a covariance $n \times n$ symmetric matrix formed as

$$\boldsymbol{R} = \int_{t_{min}}^{t_{max}} \boldsymbol{x}(t)\boldsymbol{x}^T(t)dt \in \mathbb{R}^{n \times n}, \tag{3.4}$$

and $\boldsymbol{R}$ is a positive-definite matrix and all the eigenvalues are positive. The eigenvectors are orthonormalized as

$$\langle \varphi_i, \varphi_j \rangle = \delta_{ij}, i, j = 1, \ldots, n. \tag{3.5}$$

The eigenvalues (λ_k) are ranked in descending order. They are proportional to the energy of the data so that the most energetic POD mode comes up to the first mode. The eigenvalue problem to solve by Eq. (3.3) is of size $n \times n$, and hence it is computationally expensive with high spatial resolution data. Alternatively, with high spatial resolution data, the snapshot POD method, which was first introduced by Sirovich [88], is normally applied. With time discrete datasets by $t_{min} = t_1, \ldots, t_N = t_{max}$, one can appropriate the covariance as (assuming the ensemble is sufficiently large),

$$\boldsymbol{R} = \sum_{j=1}^{N} \boldsymbol{x}(t_j)\boldsymbol{x}^T(t_j). \tag{3.6}$$

With N snapshots consisting of $n = l \times m$ data points, the data can be expressed with a $lm \times N$ matrix for a whole dataset. Each column is a snapshot expressed by vector field and each row is the data at the different location.

$$\boldsymbol{X} = [\boldsymbol{x}(t_1), \ldots, \boldsymbol{x}(t_N)] \in \mathbb{R}^{n \times N}. \tag{3.7}$$

From Eqs. (3.6) and (3.7),

$$\boldsymbol{R} = \boldsymbol{X}\boldsymbol{X}^T. \tag{3.8}$$

In snapshot POD, the eigenvalue problem of $\boldsymbol{X}^T\boldsymbol{X} \in \mathbb{R}^{N\times N}$ is solved, instead of $\boldsymbol{X}\boldsymbol{X}^T \in \mathbb{R}^{n\times n}$,

$$\boldsymbol{X}^T\boldsymbol{X}\varphi_k = \lambda_k\varphi_k, \phi_k \in \mathbb{R}^N, N \ll n. \tag{3.9}$$

A basis of the POD modes are provided by the eigenvectors,

$$\phi_k = \frac{X\varphi_k}{\sqrt{\lambda_k}}, k = 1, \ldots, N. \tag{3.10}$$

POD analysis has been used to decompose velocity fields into spatial POD modes for the investigation of the fluid mechanics [88–91] as well as in the combustion fields [91].

3.2.2 POD analysis on flame structure

Since OH PLIF image correlates to OH radical density, the POD modes describe the energy of flame fluctuation, which can be represented by OH radical distribution. In this study, the snapshot POD method is applied to a series of $10,000$ OH PLIF images. Figure 3.1 shows first ten POD modes computed from OH PLIF fluorescence distribution obtained around the flame tip. The values next to the number of each mode show the relative energy of the mode. Since a mean OH image is preliminary subtracted, a positive value means burned gas in the unburned region and a negative value represents unburned mixture in the burned region on average. The first mode, which has 43% of the energy, shows uniform distribution and represents burned region without any unburned mixture. The second, third and sixth modes show the convection of large scale unburned mixture islands. The less energetic modes, after seventh mode, represent the formation and rapid consumption of the fine-scale unburned mixture.

The energetic POD modes indicate that the formation and the rapid consumption of the fine-scale unburned mixture are dominant structures around the tip of high Reynolds number turbulent jet flame.

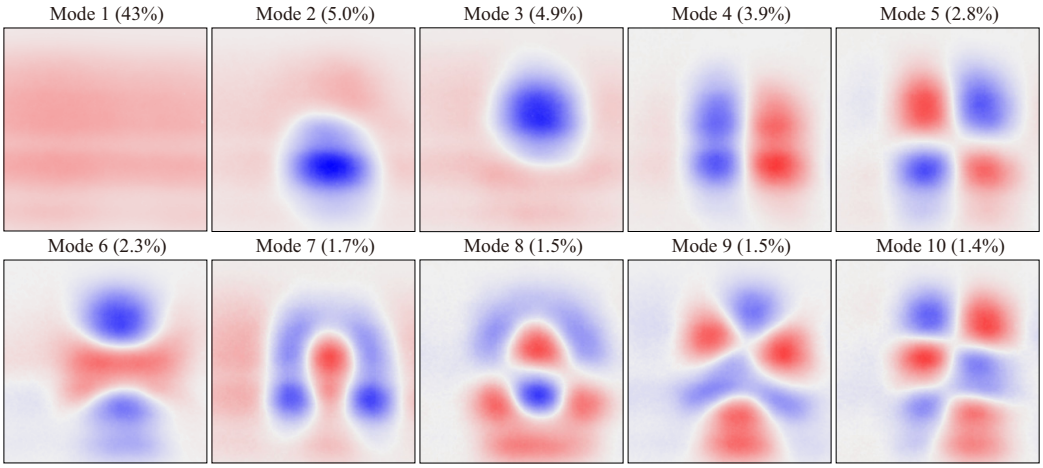

Figure 3.1: First ten POD modes for burned and unburned regions structure at $x/D = 10$ for $U_0 = 20$ m/s

3.3 Consumption of fine-scale unburned mixture

A large effort has been made to measure turbulent burning velocity S_T since it describes a flame dynamics in premixed combustion, which is the basis of turbulent combustion models. It is known that turbulent burning velocity increases with increasing turbulence intensity. Global consumption rate, which is a type of turbulent burning velocity, $S_{T,G}$, is defined by balancing the total mass flow rate of reactants, $\dot{m}_R$, and the mass per unit time of reactant that was transverse by the flame surface, $\rho_R S_{T,G} A$, as followings

$$S_{T,G} = \frac{\dot{m}_R}{\rho_R A} \tag{3.11}$$

Global consumption rate is traditionally derived as the product of the inlet velocity and the sine of the angle between the flow direction and the surface of the flame [92]. In Bunsen burner, the global consumption rate is calculated with defining A as the area of mean flame surface area [93, 94]. In outwardly propagating flames (OPFs) formed in fan-stirred bomb, the global consumption rate has been investigated with high turbulent intensity [95]. The turbulence intensity, u'/S_L, reaches to the order of ten [96, 97], which is not stabilized in the Bunsen burner under the atmospheric pressure condition.

In general, the local flame structure behaves as a laminar flame propagating with laminar burning velocity based on the flamelet concept. It is considered that an increase of flame surface are due to flame wrinkling accounts for the increase of turbulent burning velocity. It is also known that laminar burning velocity can be modified by the effect of flame stretch. Analytic, numerical and experimental studies have been made to evaluate the effect of stretch and determine the value of S_L using a counterflow flame, an outwardly and inwardly propagating flame and a Bunsen flame [98]. However, it has not been clarified that the flamelet retains laminar flame nature in high Reynolds number turbulence even with the consideration of flame stretch.

As mentioned above, high turbulent intensity can be achieved by fan-stirred

bomb. However, the radius of the flame is often measured by schlieren shadowgraphy due to the difficulty of the optical access especially under the high-pressure condition. In addition, dilatation effects cannot be distinguished from flame displacement in an OPF. On the other hand, in inwardly propagating flame (IPF), the consumption rate can be more precisely represented by the rate of volume change [99]. In this section, the fine-scale unburned mixtures are tracked in sequential images and local consumption rate is estimated from the OH and CH PLIF images.

3.3.1 Identification of the unburned mixture from the OH PLIF images

Figure 3.2 explains the identification procedure of fine-scale unburned mixture islands from OH PLIF. Figure 3.2(a) shows the filtered OH image after the correction by laser intensity distribution. The OH image is binarized as described in [100] and shown in Fig. 3.2(b). Here, red region represents burned gas and blue region shows unburned. The threshold is selected from the probability density function of OH signals. Since the probability density function is bi-nominal, the threshold is selected to the value where the probability shows the minimum between two peaks. This value is about 25% of the maximum OH signal. Only the unburned regions that are surrounded by burned regions are considered as part of fine-scale unburned mixture and included in the statistical analysis. Then, a unique identifier number is then assigned to each detected fine-scale unburned mixture, indicated by the different colors in Fig. 3.2(c).

For determining the dynamics of the detected unburned mixture, the each structure is tracked through time. The process is explained in Fig. 3.3. For a detected structure, the location in the next frame is estimated based on the mean convection velocity. If the unburned mixture is found in the estimated area in the next frame, it is regarded as a continuation of the same structure through time.

The method was applied to 10,000 sequential OH images, and approximately

4,500 unburned mixtures were detected. The cross sectional areas and perimeters of the detected mixtures are then recorded and their changes within measurement time resolution ($100\ \mu$s) are calculated.

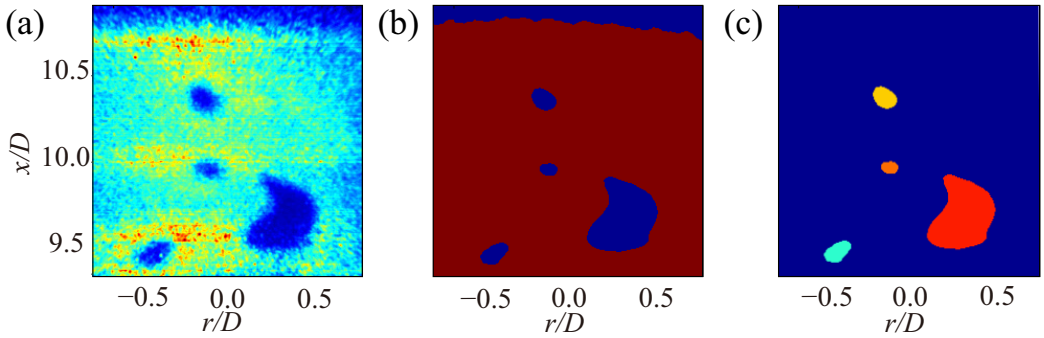

Figure 3.2: An example for the detection procedure of the fine-scale unburned mixtures from OH PLIF image.

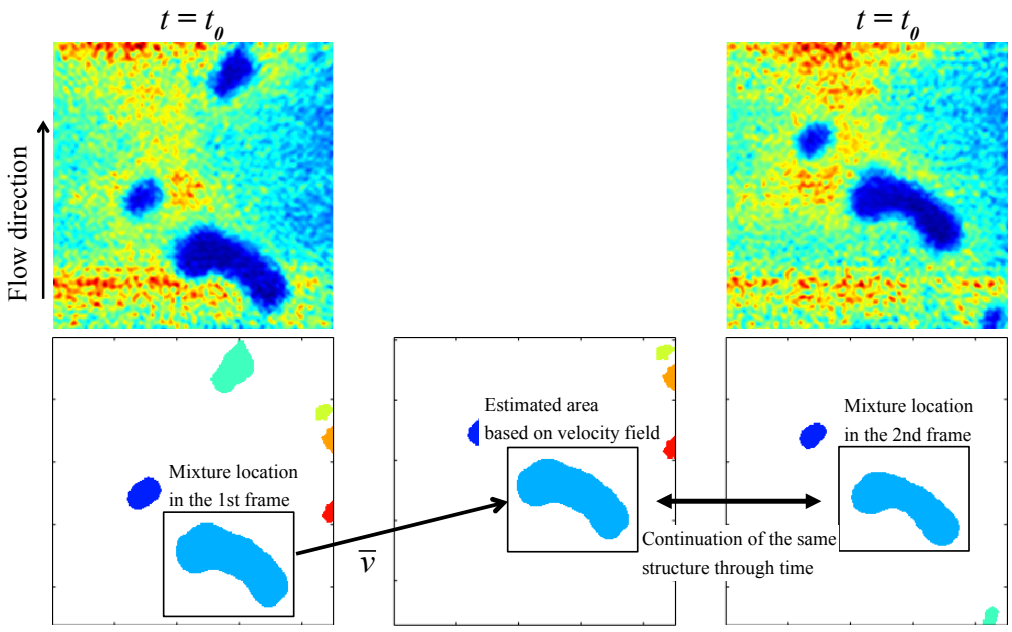

Figure 3.3: An example for the tracking of the fine-scale unburned mixtures.

3.3.2 Size of the unburned mixtures

The perimeter of the detected fine-scale unburned region (L) was calculated and treated as the length of the flame front surrounding the unburned mixture. The radii (r) of the unburned mixtures were estimated by treating the regions as circles with equivalent perimeter ($r = L/2\pi$). Figure 3.4 plots the probability density function (PDF) of the radii of the mixtures. The most expected radius of the fine-scale unburned mixtures is approximately 1 mm, of Taylor micro scale order (λ = 1.10 mm).

Elimination condition based on circularity

The geometrical departure of the cross section from a perfect circle was quantified by the circularity, defined as the perimeter ratio of the projection area to a circle of equivalent area as followings:

$$C = \frac{L}{2\sqrt{\pi A}} \tag{3.12}$$

where A is the cross-section area of the unburned mixture on the measurement plane. The ratio of a perfectly circular is unity. Figure 3.5 shows PDF of the circularity calculated from the detected mixtures. In this analysis, the threshold was set to be two. With this limitation, approximately 2.5 % of the detected mixtures were excluded in Fig. 3.4.

Figure 3.6 shows joint PDF of the radius and circularity. The scatter plot is presented only in regions of probability below 0.012. Because larger unburned mixture tends to have larger circularity, the decrease of the threshold value corresponds to exclusion of larger mixture. Therefore, conducting the same analyses with a smaller circularity threshold, the PDF of r is narrowed but the peak remains unchanged.

The following statistical analysis excludes mixtures with radii exceeding 4 mm (6.0 %), which are not regarded as fine-scale mixtures. Because of the spatial resolution limit of PLIF, very small mixtures are also excluded. Here, the radial

threshold was set to 0.20 mm (approximately 3 pixels); consequently, 6.4 % of the mixture was excluded.

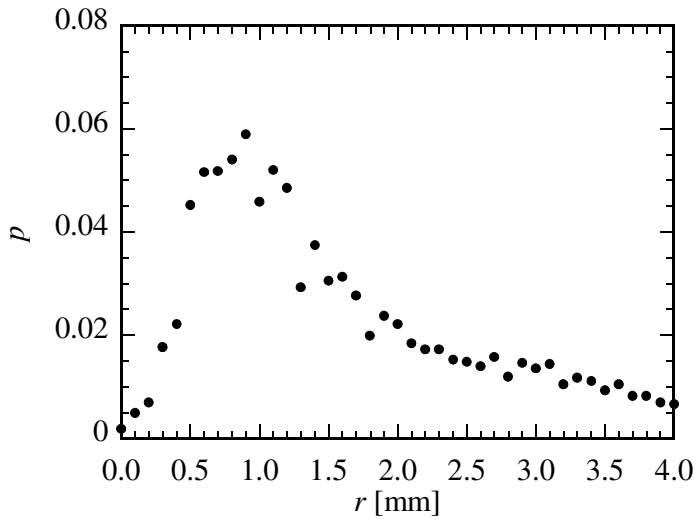

Figure 3.4: PDF of estimated radius of the fine-scale unburned mixtures detected in OH PLIF images.

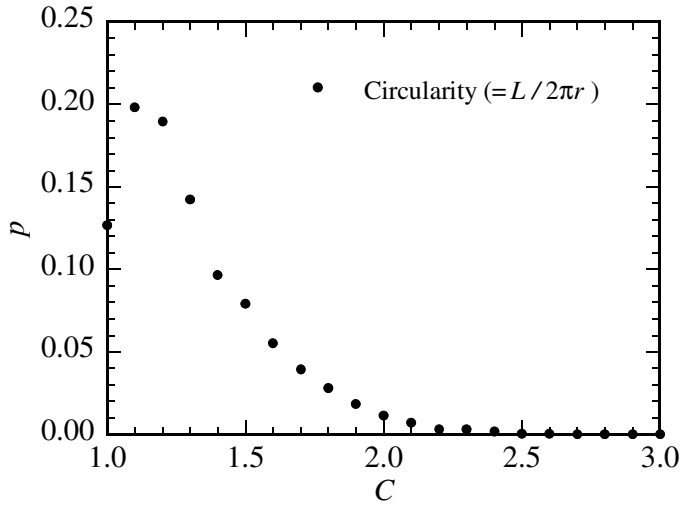

Figure 3.5: PDF of circularity, the ratio of the perimeter of the projection area to that of an equivalent area circle ($L/2\pi r$).

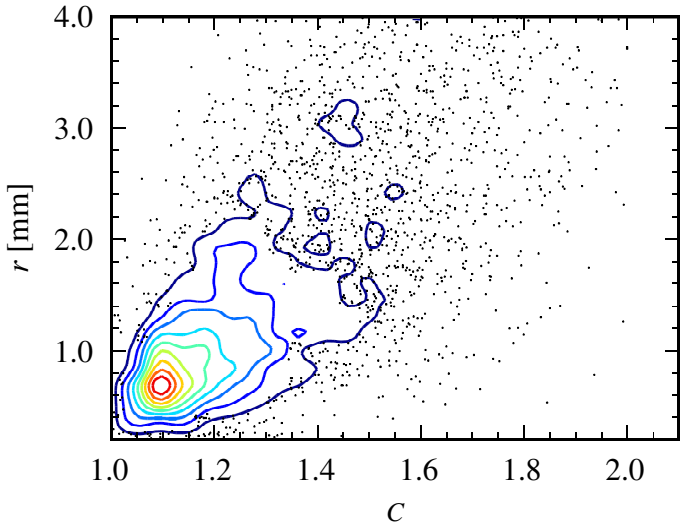

Figure 3.6: Joint PDF of mean radius of the unburned mixtures and its circularity.

3.3.3 Consumption rate of the unburned mixture

From the radii of the unburned mixtures in subsequent images (r_1 and r_2), the local consumption rate of the unburned mixture can be estimated. In this study, the local consumption rate was defined as $S_{T,l} = \Delta V/A$, where ΔV is the volume change of the unburned mixtures in a 100 μs interval and A is the flame surface area in the first image. There are several ways to estimate ΔV and A. In this study, two method will be presented: spherical assumption method and pillar assumption methods.

In Fig. 3.7, consumption rates obtained from two different methods, the spherical assumption and the pillar assumption are compared by their PDF. The most probable values of both cases coincide well. The relation between consumption rates for the spherical case and the pillar case is shown in Fig. 3.8. The pillar case shows slightly higher probability of the higher consumption rate. The difference tends to increase for higher consumption rate, which is easily expected if one considers the geometrical difference between two methods.

Figure 3.7 indicates that the fine-scale unburned mixtures has consumption rate of 1.1 m/s around the tip of the turbulent jet flame, which is very high value corresponding to 2.7 times the laminar burning velocity (0.39 m/s).

It is noted that, conducting the same analyses with a smaller circularity threshold, the PDF of $S_{T,l}$ is narrowed but the peak remains unchanged. However, the effect of error for assuming the 3D structure of the unburned mixtures to estimate volume and flame surface area as sphere or pillar is different for for each case and they have to be examined.

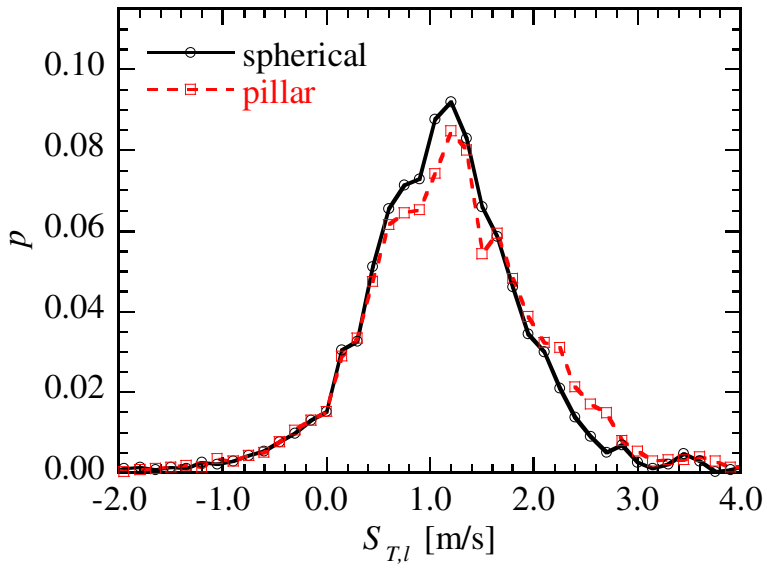

Figure 3.7: PDF of the consumption rate estimated by the spherical case and the pillar case.

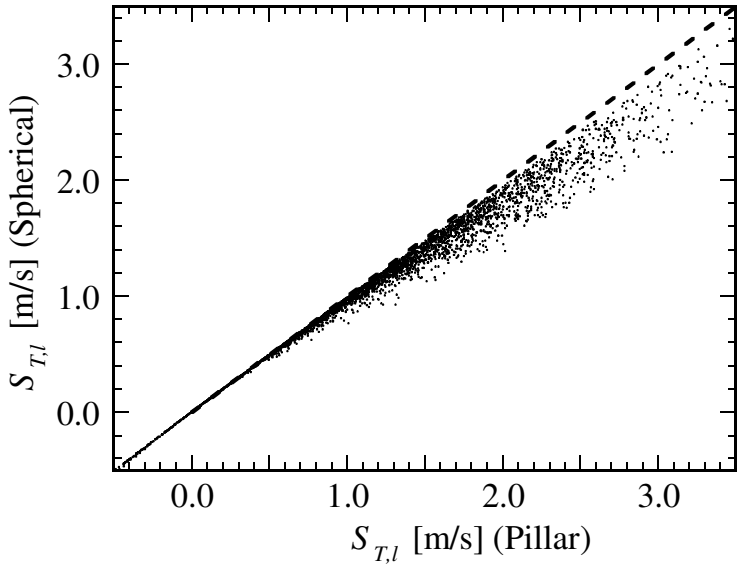

Figure 3.8: The relation between consumption rates obtained for the spherical case and the pillar case.

Consumption rate and error estimation based on spherical assumption

First, completely isolated unburned mixtures can be approximated by spheres. In this case, $\Delta V = 4\pi(r_1^3 - r_2^3)/3$ and $A = 4\pi r_1^2$.

Under the spherical assumption, the error in the consumption rate is chiefly sourced from the out-of-plane motion of the unburned mixture. Figure 3.9 shows a schematic explaining the apparent radius change by the out-of-component of the velocity (V_z). If the unburned mixture is assumed as a sphere and the measurement plane locate at the center of the sphere in the first frame ($t = t_0$), its radius measured in the subsequent frame ($t = t_0 + \Delta t$) is appeared as

$$r_{t_0+\Delta t} = r_{t_0}\left(1 - \cos\theta\right). \tag{3.13}$$

Here, $r_{t0+\Delta t}$ and r_{t0} are the radii that are measured in the first and second frames, and θ is the zenith angle of the measurement plane in the second frame with its origin at the center of the unburned mixture. From Fig. 3.9,

$$\theta = \sin^{-1}\left(\frac{V_z dt}{r_{t_0}}\right), \tag{3.14}$$

From Eqs. (3.13) and (3.14), the apparent consumption rate due to the cross plane motion of the mixture can be estimated as a function of V_z and r_{t_o}. Figure 3.10 plots the z–component of the velocities that cause an erroneous consumption rate of 1%, 5% and 10% of S_L as a function of radii of the mixtures. When the measurement plane does not exactly coincide with the center of the unburned mixture in the first frame, the value of $S_{T,l}$ is overestimated or underestimated because it is affected by out-of-plane motions.

The velocity of the unburned mixture is estimated from SPIV data. In this study, the mixture velocity is assumed as the mean velocity in the unburned region. Figure 3.11 shows the probability density function (PDF) of the velocity of the pocket. Here, the stream wise component (V_x) represents fluctuation from the mean value averaged for all detected pockets. The PDFs of all velocity components are nearly Gaussian shape. Although the out-of-plane motions of the un-

burned mixtures produce random variations in $S_{T,l}$, the contribution to the statistics is canceled out since V_z is symmetrically distributed around zero.

Figure 3.12 relates the consumption rate and the out-of-plane component of the mixture velocity (V_z) by a joint PDF. No strong correlation appears between the out-of-plane velocity and the estimated consumption rate. The most provable consumption rate is approximately 1.1 m/s at $V_z = 0$. This result suggests that, in a spherical geometry, the consumption rate of the fine-scale mixture can be estimated as approximately 2.7 times higher than the laminar burning velocity (0.39 m/s).

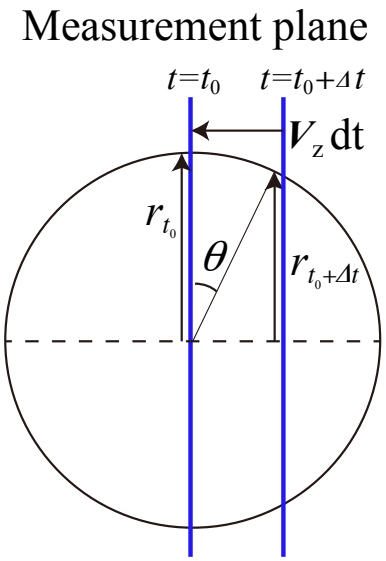

Figure 3.9: Schematic of apparent radius change for spherical mixture with out-of-plane component of velocity.

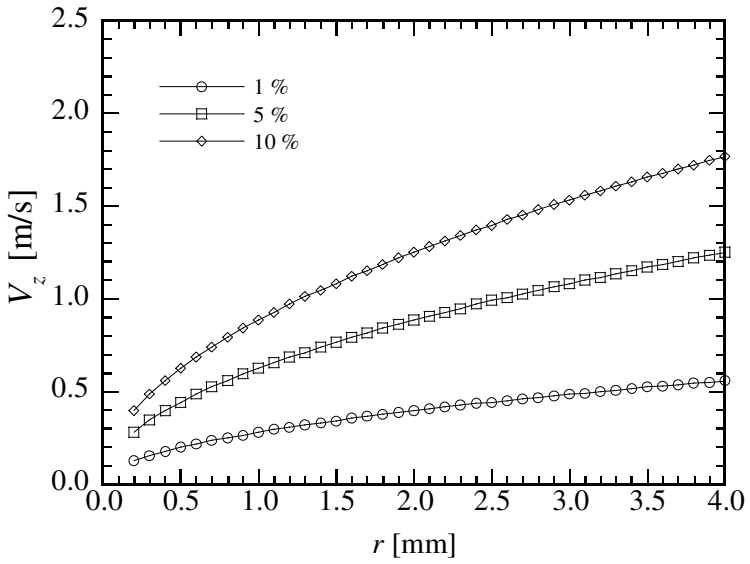

Figure 3.10: z–component of the velocities that cause an erroneous consumption rate of 1%, 5% and 10% of S_L as a function of radii of the mixtures.

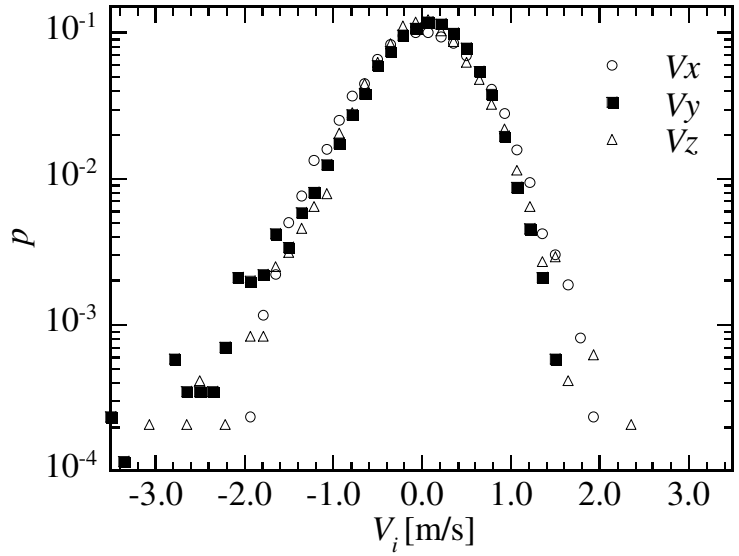

Figure 3.11: PDF of the velocity of small-scale unburned mixtures.

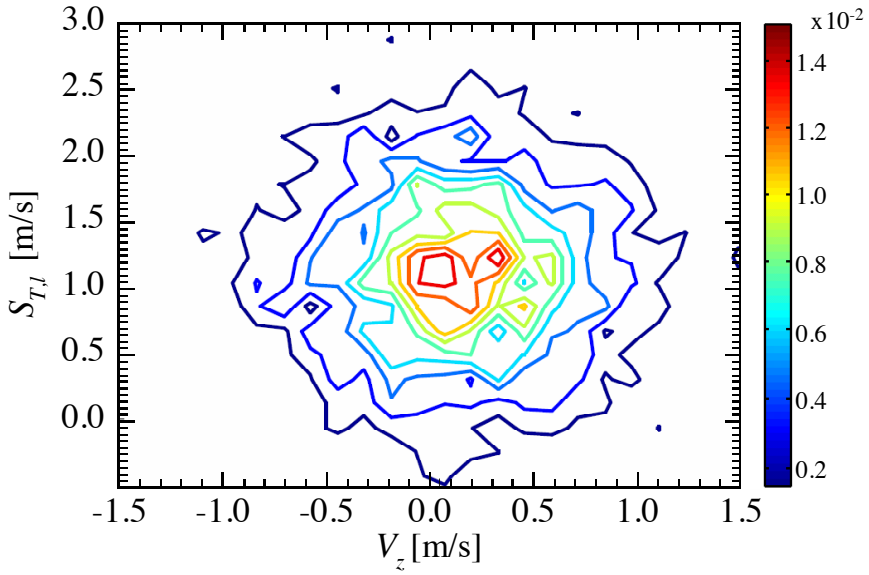

Figure 3.12: The joint PDF of the consumption rate and out-of-plane velocity of the unburned mixture in the spherical assumption.

Consumption rate and error estimation based on pillar assumption

The consumption rate is estimated using the "pillar assumption" , wherein the cross sections of a two-dimensional object are cut by the laser sheet. In this case, $S_{T,l} = \pi(r_1^2 - r_2^2)/2\pi r_1$ for the unit depth. It should be noted that the pillar assumption is insensitive to out-of-plane motions of the unburned mixture. Figure 3.13 relates the consumption rate and the out-of-plane component of the mixture velocity (V_z) by a joint PDF. No strong correlation appears between the out-of-plane velocity and the estimated consumption rate.

Under this assumption, errors mainly arise from the inclination of the measurement plane with respect to the plane perpendicular to the pillar object. If the unburned mixture is assumed as a circular cylinder, the inclination effect can be related to the circularity of the detected unburned mixture. In this study, the effect is corrected by assuming a circular cylindrical flame with laminar burning velocity S_L. In Fig. 3.14, a joint PDF of the consumption rate and circularity is presented, and it can be observed that the most probable value of the consumption rate depends on the circularity.

Figure 3.15 shows a schematic explaining the apparent consumption rate by the inclined measurement plane. When the pillar axis is inclined to the measurement plane, its projected shape on the image plane becomes elliptical. The effect of inclination appears most significantly on the major axis of the elliptic image. The maximum apparent consumption rate with the laminar burning velocity, S_L can be represented by $S_L\Delta t/e$ where e denotes ellipticity ($e = b/a$, a and b stand for the semi-major and semi-minor axes of the ellipse) and Δt means the time separation between two consecutive frames. In Fig. 3.14, the apparent consumption rate of circular cylinder mixture at $C = 1$ due to the inclination effect is also plotted by dotted lines. Since it is on the same order of magnitude compared to the measured values, its effect cannot be neglected and should be taken into account.

When the correction is performed to the detected unburned mixtures, the ratio of the apparent increase of the consumption rate calculated by the decrement of

ellipse area dA_e in Δt is adopted:

$$dA_e = \frac{\pi \left(ab - \left(a - \frac{S_L \Delta t}{e} \right) \left(b - S_L \Delta t \right) \right)}{S_L \Delta t L_e} \tag{3.15}$$

which is a function of e, L_e and the area of ellipse. Here in this analysis, e is obtained from the measured value of perimeter L_e. To obtain the functional relationship between e and L_e, it is necessary to solve the so-called elliptic integral of the second kind:

$$L_e = 4a \int_0^{\pi/2} \sqrt{1 - k^2 \cos\theta} d\theta, k^2 = 1 - \frac{b^2}{a^2} \tag{3.16}$$

Here, instead, the function is numerically integrated. Figure 3.16 shows the relation between the corrected consumption rate and circularity. Due to this correction, the most probable value of the consumption rate at certain circularity does not depend on the circularity itself.

Figure 3.17 shows the joint PDF of the corrected consumption rate and the out-of-plane velocity in the pillar assumption. It is shown that the most probable consumption rate, $S_{T,l}$ is 0.72 m/s at V_z = 0, far exceeding S_L on the basis of the pillar assumption as well.

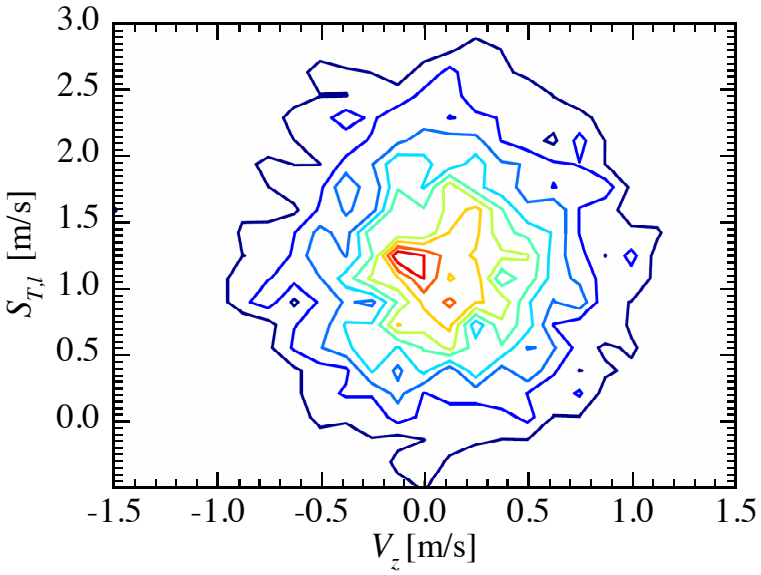

Figure 3.13: Joint PDF of the consumption rate and out-of-plane velocity of the unburned mixture in the pillar assumption.

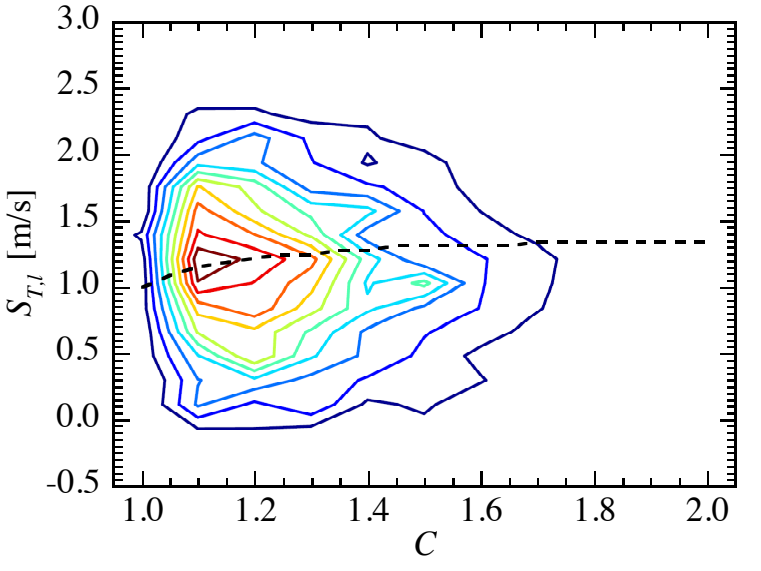

Figure 3.14: Joint PDF of the consumption rate and circularity for the pillar case. The dotted lines represent the apparent consumption rate for circular cylinder mixture with the most probable consumption rate at $C = 1$.

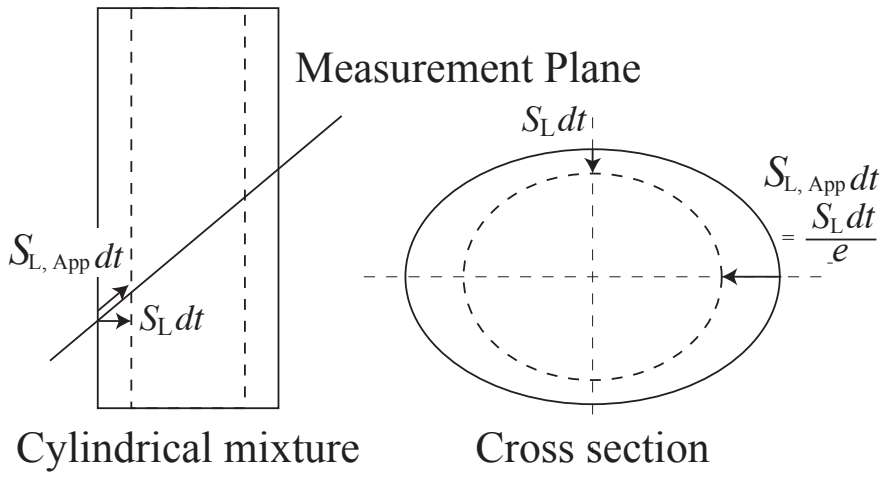

Figure 3.15: Schematic of apparent consumption rate for circular cylinder mixture with S_L.

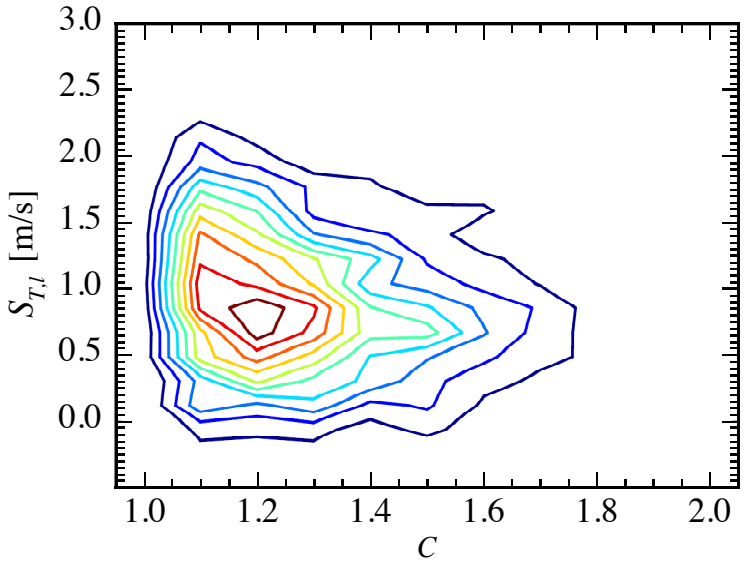

Figure 3.16: Joint PDF of the corrected consumption rate and circularity for the pillar case.

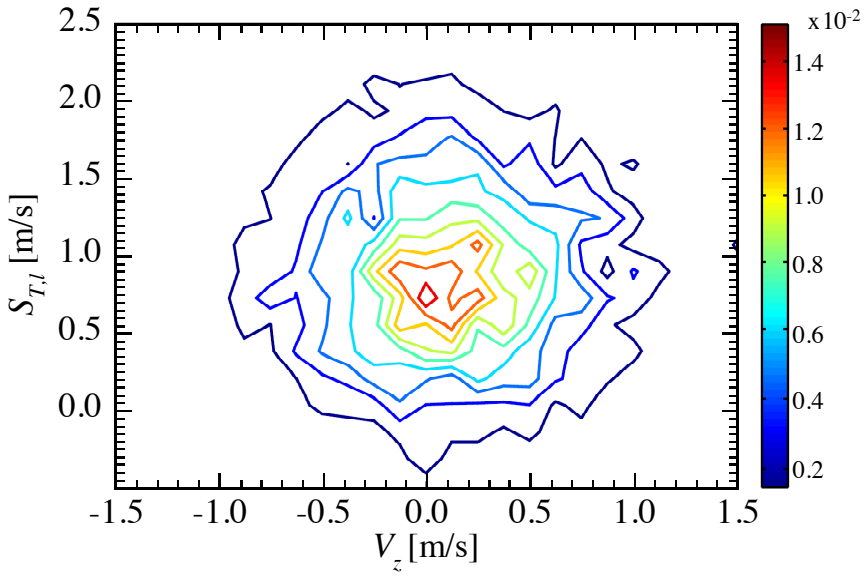

Figure 3.17: Joint PDF of the corrected consumption rate and out-of-plane velocity of the unburned mixture in the pillar assumption.

Neither assumption yields strong correlation between the local consumption rate and the out-of-plane components of the velocity fluctuation (cf. Figs. 3.12 and 3.17). When the unburned mixture is neither spherical nor pillar-shaped, the out-of-plane motions would raise or lower the $S_{T,l}$ depending on the 3D shape. Consequently, $S_{T,l}$ may vary around the peak.

In the above analysis, radii of the unburned mixture are estimated by the perimeter of the detected area as described in Sec.3.3.2. As an alternative to the perimeter, r can be estimated from the area occupied by the unburned mixture (A_c) as $r = (A_c/\pi)^{1/2}$. When the cross-section of the mixture is a perfect circle, resulting r from these two methods coincide. In the case of non-perfect circle, that is, the mixtures that have non-unity circularity, the area method results in smaller radii. Because the perimeter of the cross section of the mixture relates to the flame surface area and the flame surface area relates to the turbulent burning velocity, the perimeter method is adopted in this study. Table 3.1 summarize the methods to calculate r and $S_{T,l}$. As presented in Fig. 3.18 by PDFs of consumption rate obtained from both methods, the adaptation of the area does not have a huge effect on the consumption rate under the pillar assumption (Fig. 3.18(a)), nor under the spherical assumption (Fig. 3.18(b)).

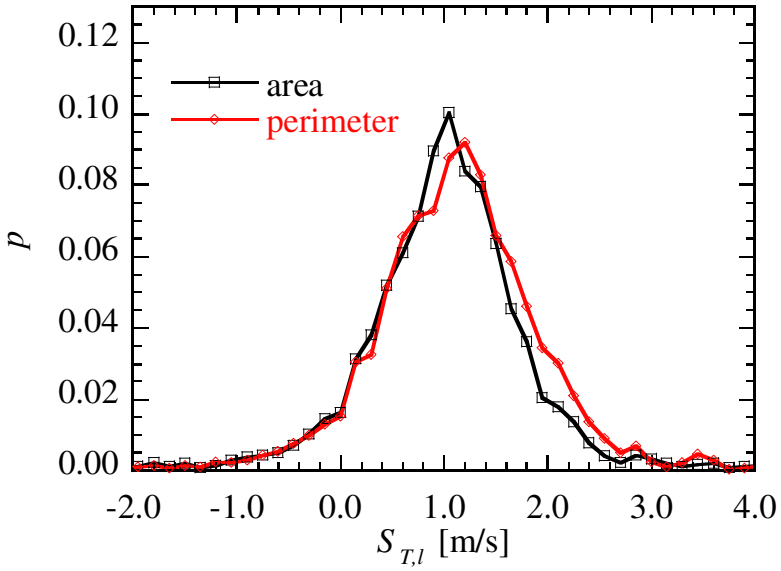

(a) spherical assumption

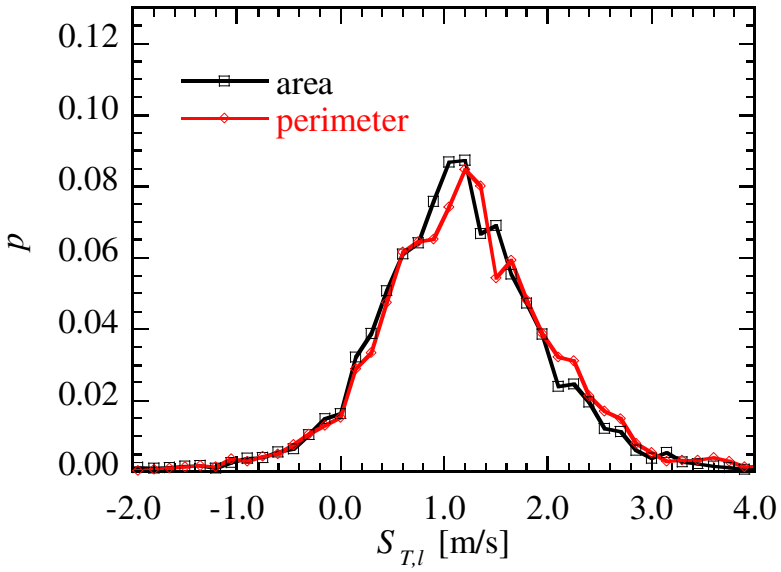

(b) pillar assumption

Figure 3.18: PDF of the consumption rate calculated from the radii estimated with the perimeter and the area.

Table 3.1: The estimation methods for radii and consumption rate.

	By the perimeter	By the area of cross-section
r	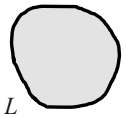 $\frac{L}{2\pi}$	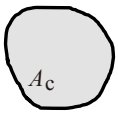 $\left(\frac{A_c}{\pi}\right)^{\frac{1}{2}}$
$S_{T,l} = \Delta V/A$	Spherical assumption	Pillar assumption
	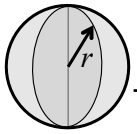 $\frac{\Delta\left(\frac{4}{3}\pi r^3\right)}{4\pi r^2}$	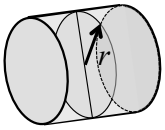 $\frac{\Delta\left(\pi r^2\right)}{2\pi r}$

3.3.4 Consumption rate estimated from the CH PLIF images

In this study, the consumption rate of the unburned mixture can be estimated from the acquired CH PLIF images. However, as shown in Fig. 2.18(a), the CH images were very noisy and distributed. Therefore, the consumption rate is estimated from the CH images with the assistance of the OH images as depicted in Fig. 3.19.

Initially, the CH signals were searched around the unburned mixture identified from the OH PLIF images and the mean radius of the signal distribution was calculated. In this calculation, a certain point in the unburned region is selected to be an origin and distance between the origin and a CH signal detection point represented by r_i. The mean radius is estimated by $r = \Sigma r_i/N$, where N is the number of points at which a CH signal is detected. For the subsequent frame, the CH signals were searched within the region predicted from the convection velocity of the unburned mixture, and the mean radius was recalculated. The consumption rate of the unburned mixture was then estimated from the difference between the radii, under both spherical and pillar assumptions. It is noted that the CH fluorescence signal is searched also in a frame after unburned mixture disappears in OH images since there are fine-scale unburned mixtures that are only detected in CH PLIF images as shown in the Sec.2.4.4.

Figure 3.20 compares the consumption rates obtained from the CH and OH images. Note that the number of samples in the CH methods is not as high as that in OH ones. The CH method gives a flat probability distribution around the peak obtained from the OH PLIF data. This flattening is caused by the disconnected CH signal distribution. When calculating the mean radius, the degree of the disconnected distribution corresponds to the number of points used to discretize the continuous flame front. In other words, the degree of the disconnected distribution represents the spatial resolution of the radius estimation, and induces errors in flames of low consumption rate. Therefore, the peak of the consumption rate is obscured in the CH method. However, the mean consumption rate (approxi-

mately 1.2 m/s) is the same in both CH and OH methods. Consequently, local consumption rate of fine-scale unburned mixture estimated by CH PLIF images also indicates much higher burning velocity than S_L.

Figure 3.21 is a histogram of the radii of unburned mixtures detectable in the CH image (excluding those found in the OH image). The most probable value is approximately 1 mm, which is coincident with Fig. 3.4. Due to 3D geometry, the smaller the unburned mixture, the larger the flame surface area per unit volume. The unburned mixtures in such small structures are rapidly heated. Within these very small scale hot unburned mixtures, OH radicals may have been created while the CH fluorescence indicates that there is still unburned mixture and they are consumed with a significant heat release rate.

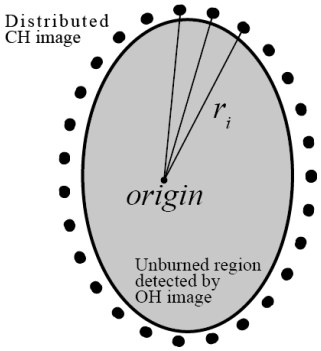

Figure 3.19: Schematic of the unburned mixture detection from the CH PLIF images with an assistance of the OH PLIF images.

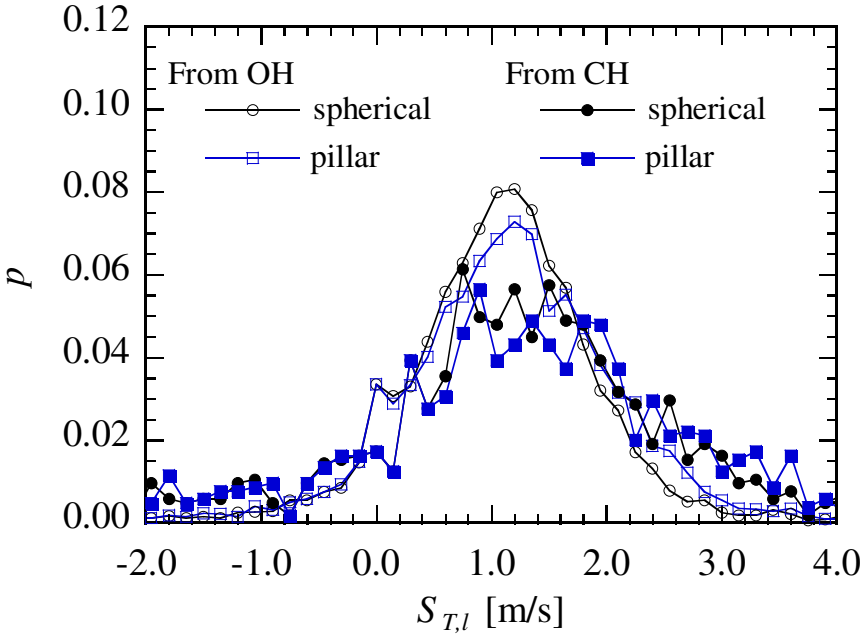

Figure 3.20: PDF of the consumption rate estimated from the OH and CH PLIF images in the spherical and pillar assumptions.

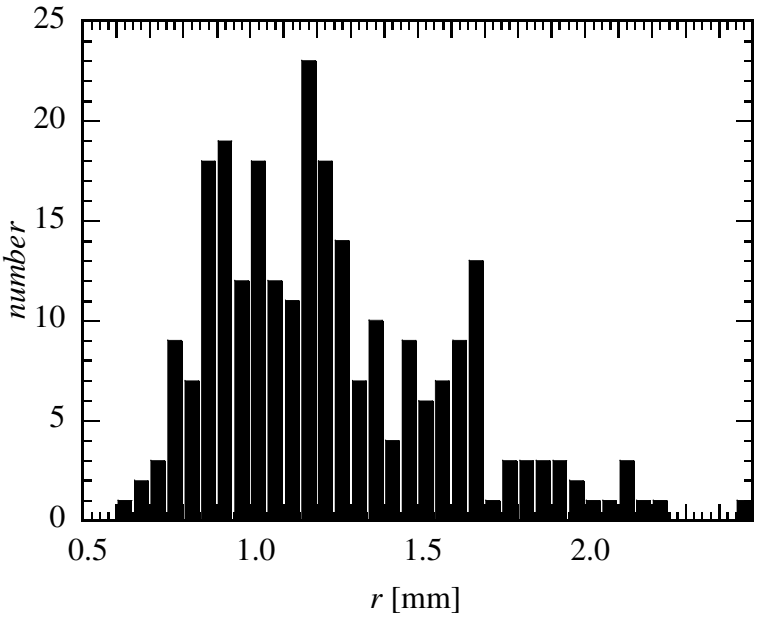

Figure 3.21: Histogram of estimated radius of the fine-scale unburned mixtures detected only from CH PLIF images.

Radius effect on the consumption rate based on the pillar assumption

Figure 3.22 shows the relation between the size of the unburned mixture and the consumption rate by joint PDF of the consumption rate and mean curvature ($k = -1/r$) of the flame front that. The flame element convex toward the burned side has negative curvature. The scatter plot is presented only in regions of probability below 0.002. This plot clarifies the effect of radius on the consumption rate. The thick solid line in this figure plots the most probable consumption rate as a function of k, which suggests the increase of the consumption rate with decreasing k (or decreasing r). When $k \approx -1.6 \times 10^3$ m^{-1} ($r \approx 0.63$ mm), the consumption rate reaches 1.25 m/s, which is 3.2 times higher than laminar burning velocity. When $k \approx -1.8 \times 10^3$ m^{-1} ($r \approx 0.56$ mm), the most probable consumption rate decreases. This may be caused by many unburned mixtures in this range of size that are completely consumed within measurement time resolution (100 μs). They may represent high consumption rate but are not included in the estimation of the consumption rate. It is important to note that heat conduction or even radiation also has a significant effect in the fine-scale structure. Consequently, heating up of the unburned mixtures may have a large effect to enhance $S_{T,l}$.

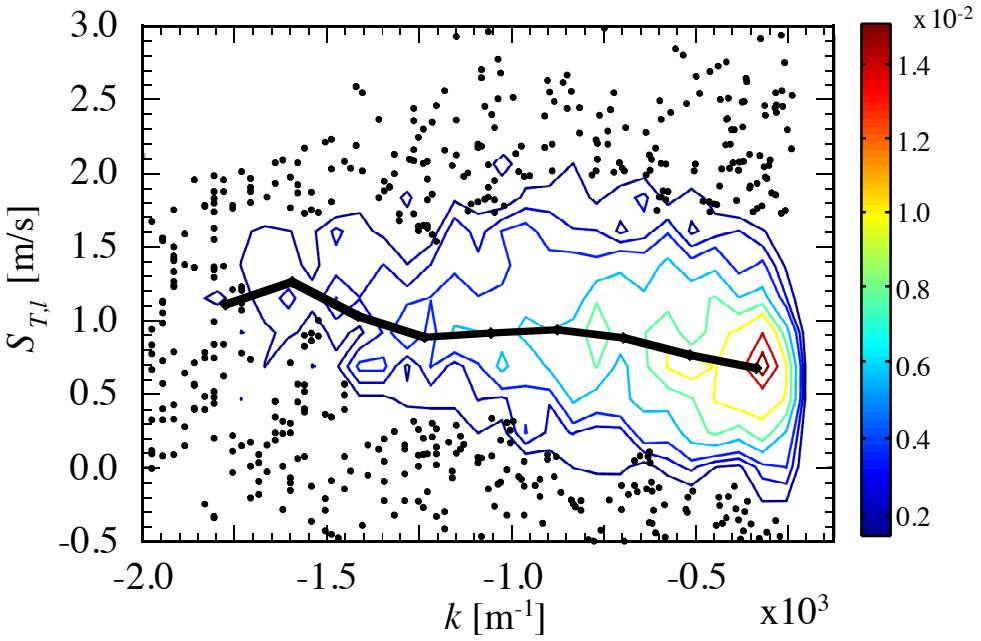

Figure 3.22: Joint PDF of the corrected consumption rate and mean curvature of the flame front. Thick solid line indicates the most probable consumption rate as a function of mean curvature k.

3.4 Heating of the fine-scale unburned mixtures

Considering the facts that there are some regions of fine-scale unburned mixtures are detected only in the CH images, and consumption rate shows increasing trend with decreasing the size of the unburned mixtures, it can be deduced that the unburned mixtures in such small structures are heated because of heat conduction from surrounding burned hot gases or heat radiation. In this section, an influence of heating of the fine-scale unburned mixtures is estimated assuming heat conduction due to surrounding hot gases.

Figure 3.23 shows laminar burning velocity (S_L) as a function of preheat temperature under the same condition of the present measurement, pressure of 0.1 MPa and equivalence ratio of 1.0. Here, S_L is calculated by PREMIX of CHEMKIN package [101] considering GRI Mech3.0 which includes 53 reactive species and 325 elementary reactions of methane/air reaction. The approximate curved line fitted to a third degree polynomial equation in the range between 300 K and 800 K, is added. S_L generally increases with increasing preheat temperature. Temperature of the unburned mixtures observed in the present measurement is estimated using the relationship between preheat temperature and the laminar burning velocity.

Figure 3.24 shows estimated temperature of unburned mixtures from the most probable consumption rate conditioned by mean curvature. On the assumption that the temperature increase of the unburned mixtures themselves is the cause of the consumption rate, the estimated temperature is about 590 K at $r \approx 0.63$mm, where the consumption rate reaches the maximum within the range of this measurement.

It is known that burning velocity of a laminar flame with curvature is different from unstretched laminar burning velocity (S_L) aside from the effect of flame stretch. To demonstrate this "pure curvature effect", the simplest situation is a stationary spherical flame as shown in Fig. 3.25 [102]. The flame is supported by a point source of constant mass flow rate $\dot{m} = \rho u A$, where ρ is the density, u the

velocity and A the area of streamtube. The one-dimensional balance equation of energy and species though a radical streamtube across the unstretched flame are

$$\dot{m}c_p(T_b - T_u) = A_F q_c w_F, \tag{3.17}$$

$$\dot{m}c_p Y_u = A_F w_F, \tag{3.18}$$

where T is the temperature, Y the mass fraction and subscript u and b indicate values in the unburned and burned state, respectively. c_p is the specific heat, A_F the area of flame front, q_c the heat of combustion, w_F the mass reaction rate integrated over the reaction zone. Since there is no heat loss in this situation, the flame is basically one-dimensional planar flame. From Eq. 3.17 and Eq. 3.18, $c_p(T_b - T_u) = q_c Y_u$, which shows that the burned gas temperature (T_b) becomes the adiabatic temperature. In this case of stationary spherical flame, since streamtube area is varying across the flame, the equation of continuity is,

$$\rho_u u_u A_u = \rho_b u_b A_b, \tag{3.19}$$

where A_u and A_b denote the stream tube area at preheat zone and reaction zone, respectively. Comparing Eq. 3.19 from that of unstretched laminar flame ($\rho_u S_L = \rho_b u_b$), the burning velocity is

$$u_u = \frac{A_b}{A_u} S_L. \tag{3.20}$$

Since $A_b > A_u > 1$, the burning velocity is hence increased for a flame with negative curvature.

In a flame with curvature, the increase of the burning velocity is caused by the unbalance between reactant mass flow rate and the amount of mass needed to keep a laminar flame due to a varying streamtube area as shown above. However, in the theory using the stationary spherical flame, the deficient reactant is provided by a point source, which is physically impossible. Here instead, the laminar flame propagating with curvature is considered as shown in Fig. 3.26.

The differential conservation equation of mass in flame coordinate $\eta = R - x$,

where R is the location of the thin reaction zone, can be expressed as [103]

$$\frac{\partial \dot{m}}{\partial \eta} - \rho \dot{R} \frac{\partial A}{\partial \eta} = 0, \tag{3.21}$$

where $\dot{R}$ is the propagation speed and $\dot{m} = A\rho(\dot{R} - u)$ the mass flow rate consumed by the flame. Integrating Eq. 3.21 from unburned state to burned state,

$$\dot{m}_u - \dot{m}_b = -\rho \dot{R} A_b (1 - \frac{A_u}{A_b}), \tag{3.22}$$

The streamtube area ratio across the flame is

$$\frac{A_u}{A_b} = (\frac{R - \delta_T}{R})^2, \tag{3.23}$$

where δ_T is preheat zone thickness. Equation 3.22 shows that the mass flow rate of burned gas leaving the reaction zone ($\dot{m}_b$) does not balance reactant mass flow rate at the upstream boundary of the preheat zone ($\dot{m}_u$) as is the case in a stationary flame with curvature.

Now, the temperature increase in the fine-scale unburned mixture is estimated on the assumption that heat of combustion of the excess mass flow shown as Eq. 3.22 is used for the heatup. Further assuming that the temperature increases uniformly in the unburned mixture, the rate of temperature increase $\Delta T/\Delta t$ can be estimated as

$$\frac{\Delta T}{\Delta t} = \frac{q_c(\dot{m}_u - \dot{m}_b)}{\rho_u V c_p}, \tag{3.24}$$

where V is a volume of the unburned mixture. Figure 3.27 shows a temperature transition of unburned mixture released into burned gases with an initial size of r_0. The size of the mixtures decreases with unstretched laminar burning velocity at the preheat temperature. The estimated temperature of the unburned mixtures from the most probable consumption rate is added with red circle. The estimated temperature of the mixtures whose size are below 0.8 mm, coincides with the temperature transition of unburned mixtures that are released with the initial size of $1.5 \sim 3.0$ mm.

In this analysis, the laminar flame propagates into quiescent mixture as shown in Fig. 3.26. An effect of flame stretch is not taken into account since Lewis number of stoichiometric methane-air mixture is about unity. In actuality, the effect of flame stretch due to the turbulence may have an effect to the burning velocity. It has been revealed that the strain rate tangential to the flame surface can be normalized by turbulence characteristics [86]. The most probable tangential strain rate normalized by Taylor time scale (λ/u'_{rms}) is 1.0 in fully developed turbulence. This means that many flame elements of turbulent premixed flame is subject to tangential strain rate about the reciprocal of Taylor time scale. According to the turbulence characteristics obtained at the center of the measurement region, the reciprocal of Taylor time scale is about 2600 s^{-1}. Although the effect of such strong strain rate on laminar burning velocity remains to be clarified, it is not expected to depend strongly on the size of the unburned mixtures. The facts that the estimated temperature from the most probable consumption rate of larger mixture than approximately 1.2 mm is far exceeding that is expected considering the effect of the heatup, and the difference between those does not strongly depend on the size of the unburned mixtures suggest that the burning velocity could have influenced by strain rate caused by turbulence.

Structure of coherent fine-scale eddies, which are universal structure of turbulence, and their interaction with turbulent flame have been investigated by recent 3D DNS [84–86]. It has been reported that the coherent fine-scale eddies in the burned side tend to decay rapidly by the increase of viscosity [85, 86]. It has been also clarified that the distance between fine-scale eddies in turbulence is about Taylor micro scale. It is reasonable to suppose that fine-scale eddies in isolated unburned mixtures smaller than Taylor micro scale decay rapidly due to turbulent flame and there is no strong turbulence. Taylar micro scale obtained at the center of the measurement region is 1.10 mm. In unburned mixtures that are smaller than approximately 1 mm, there is no strong turbulence and therefore, and the effect of heatup of the mixtures becomes probably dominant.

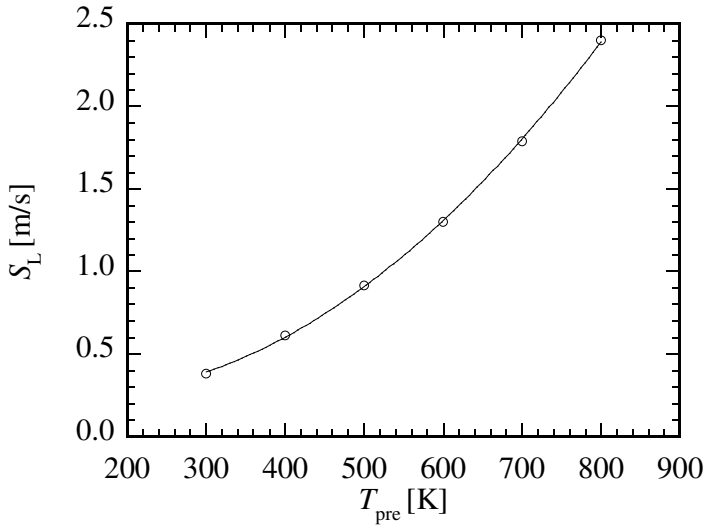

Figure 3.23: Laminar burning velocity as a function of preheat temperature.

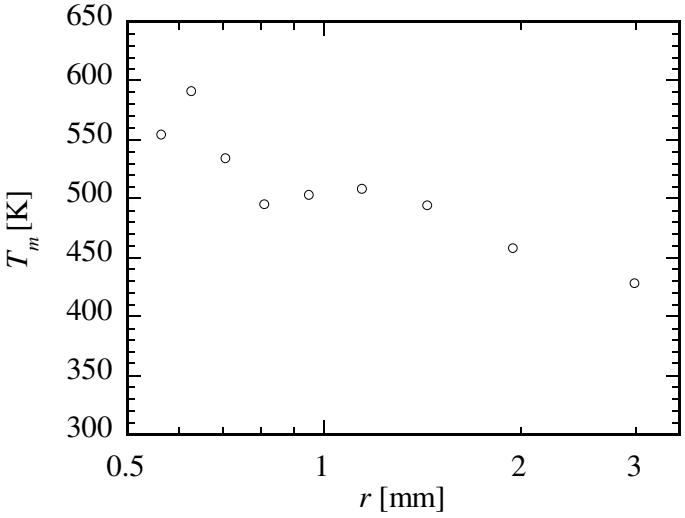

Figure 3.24: Estimated temperature of unburned mixtures from the most probable consumption rate conditioned by mean curvature.

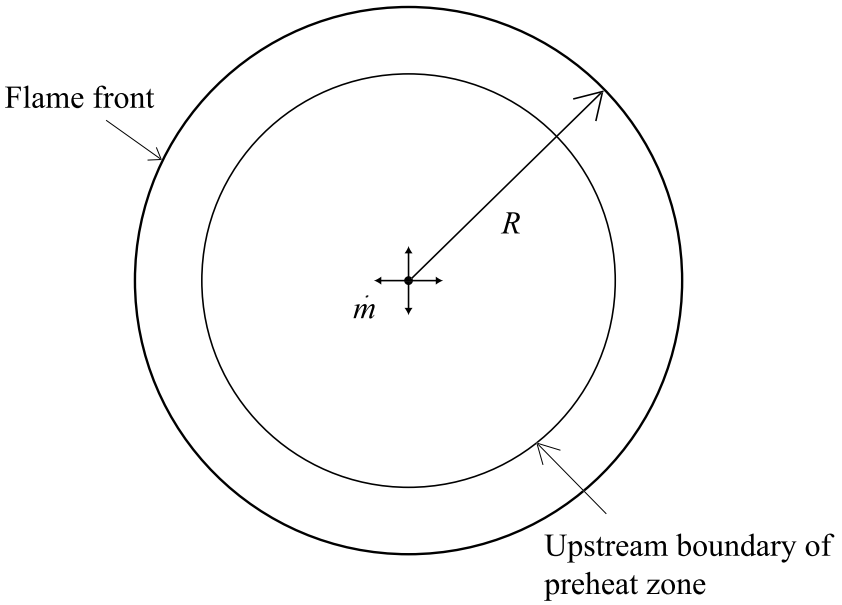

Figure 3.25: Schematic of the stationary spherical flame supported by a point source.

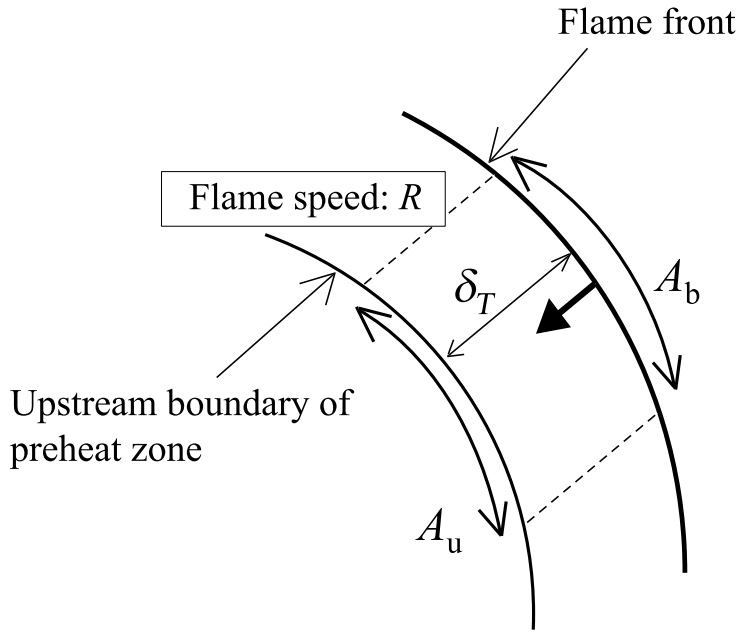

Figure 3.26: Schematic of the propagating spherical flame.

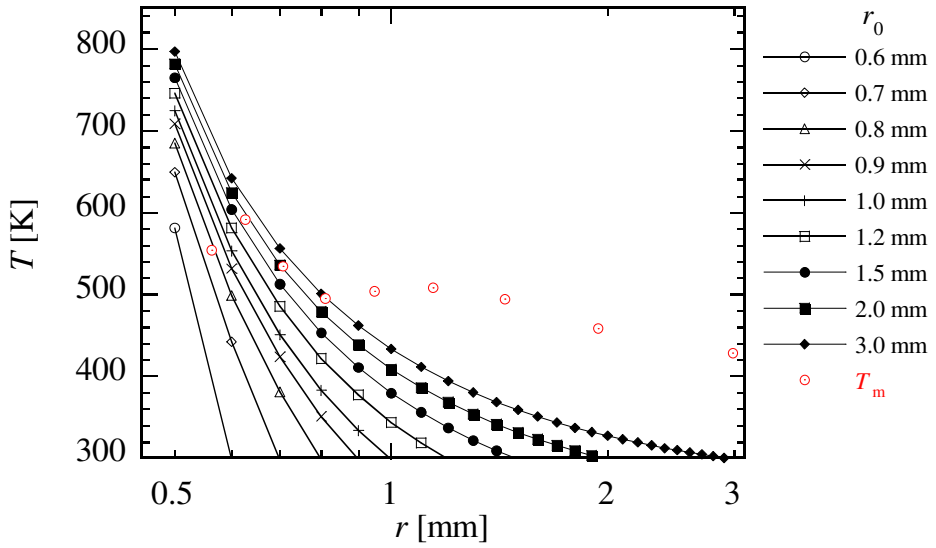

Figure 3.27: Temperature transition of unburned mixture released into burned gases with an initial size of r_0.

3.5 Interim conclusions

In this chapter, to clarify the flame and flow dynamics of turbulent premixed flame in high Reynolds number turbulence, the rapid consumption of the fine-scale unburned mixtures, which are observed around the flame tip of the turbulent jet, has been investigated. The followings are the obtained results.

(1) The formation and the rapid consumption of the fine-scale unburned mixture are dominant structures around the tip of high Reynolds number turbulent jet flame.

(2) The radius of the fine-scale unburned mixtures is approximately 1 mm, of the order of Taylor micro scale.

(3) Every consumption rate which is obtained from CH/OH PLIF images on the basis of spherical and pillar assumption, is much higher than the laminar burning velocity (0.39 m/s).

(4) The most probable consumption rate as a function of mean curvature suggests the increase of the consumption rate with decreasing curvature (or decreasing radius of the mixture).

(5) There are two dominant effects on the consumption rate, which are heating up of the mixtures by surrounding burned gas and strain rate due to turbulence.

Chapter 4

Instability of liquid-fueled swirl-stabilized turbulent combustor

4.1 Introduction and objectives

In power generation and aircraft gas turbine engines, especially operated on lean premixed regime, combustion instability is a critical problem.

Secondary fuel injection and fuel staging procedures are considered an effective combustion control approach. The addition of considerably small amount of energy has an effect to anchor the main lean flame to locally created near stoichiometric flame leading flame stabilization [104]. It has been revealed that the frequency control of secondary fuel injection suppresses fluctuations of the high temperature gas in the recirculation zone and large-scale fluctuation of the heat release rate [105].

Flame stabilization process is investigated in staged multi-injection combustor [106]. It has been revealed that the fuel distribution because of staging multi-injection strongly affects the flame stabilization process, modifying the thermoacoustic coupling. They also revealed the existence and the dominant influence of PVC in certain range of operating condition. They inferred that the primary stage controls the formation of the aerodynamic instability.

In order to achieve a stable operation over wide range of conditions in terms of input temperature, pressure, equivalence ratio and flow velocity etc., which

is required in the industrial gas turbine combustor, the dynamic behavior of the turbulent combustor has to be clarified in various conditions.

While the thermoacoustic instability is described as a system dependent instability, the aerodynamic instability strongly depends on the whole flow field in the combustion chamber as well as swirl number, the mode of fuel entry and equivalence ratio. The objective of this chapter is to clarify the instability of liquid-fueled swirl-stabilized combustor using the high-speed laser diagnostics. The two types of instability that are acoustic and aerodynamic instability are investigated in various flow and droplet conditions.

After the measurement techniques and combustor configuration in Sec 4.2, the operating conditions investigated in this study are shown in Sec. 4.3 and followed by analytic technique in Sec. 4.4. The global structure of flame and flow, and acoustic behavior are shown firstly, and the each mode is further investigated using dynamic mode decomposition (DMD) in Sec. 4.6 and 4.7.

4.2 Experimental setup and apparatus

Figure 4.1 shows a schematic view of the experimental setup. In this section, experimental burner and diagnostics are introduced.

4.2.1 Time–resolved stereoscopic PIV

The velocity measurement is conducted in the axial plane of the combustion chamber with time–resolved particle imaging velocimetry (PIV). In this study, no seeding is added in the flow, the fuel droplets are used as tracer particle instead. The basic theory is same as described in 2.3.2 but the measurement system consists of laser, camera and optics are different.

The laser system consists of two Nd:YAG lasers (Quantronix) with the wavelengths of 532 nm, which are emitted at 5 mJ/pulse. A temporal width od the laser is 120 ns at a frequency of 10 kHz. The laser beams are guided to the measurement region, and expanded by sheet forming optics (Melles Griot). The width and

thickness are 100 mm and 1 mm, respectively. Large rectangular silica windows are equipped to both sides of the combustion chamber. The laser sheets cross the chamber its center line through two small rectangular quartz windows that are placed on the upper and lower walls. The light scattered by the tracer particles is recorded by a high speed camera (Photron, SA-5) with a macro lens (Nikon, Micro-Nikkor, 105mm f/2.8) . The camera records 776×448 pixel images at $20,000$ fps. The timing of the measurement is controlled by a delay generator (BNC 555 pulse/delay Generator) and the delay systems of the high speed camera. The time delay between two pulses, Δt, has been set to 20 μs. The size of the interrogation window size is 48×48 pixels in this study. Measurement regions are set to 90×150 mm and the camera resolution is determined to be 776×448 pixels, which means that the spatial resolution of PIV is about 9 mm for 48×48 pixels interrogation region. Note that the velocity vectors are evaluated with 67 $\%$ overlap. In this sense, velocity vectors are obtained every 3 mm. The high spatial resolution PIV algorithm described in Sec. 2.2.2 is used to calculate the two-dimensional velocity field.

4.2.2 Pressure and heat release fluctuations measurements

To measure pressure fluctuation, three Brüel and Kjær microphones (shown as M1, M3 and M4 in Fig. 4.1) are placed in semi-infinite water cooled wave-guides. M1 is flush mounted in plenum while M3 and M4 are placed in the middle and downstream of combustion chamber to measure pressure fluctuations. These microphones have an uniform sensitivity in a wide band of frequency between 4 and 20 kHz.

In lean premixed flame, it is known that the chemiluminescence is caused by the radiation from excited species in the reaction region, such as OH^*, CH^* and C_2^* for hydrocarbon flames. The chemiluminescence of these radicals has been commonly used to characterize combustion flame. It has been shown that for a lean premixed flame, these intensities are proportional and in phase with its heat

release rate [107, 108]. Although a complexity in turbulent partially premixed flame to measure heat release rate especially in turbulence is also shown [109, 110], the chemiluminescence emission gives qualitative information and is a good indicator of the flame location and behavior [110, 111].

In this study, CH^* chemiluminescence is measured as shown in Fig. 4.1. A photo-multiplier (Hamamatsu, H5784-04) is used to measure global CH^* chemiluminescence. A filter ($\lambda = 408 \pm 10$ nm) is equipped and a spherical lens ($f = 300$ mm) is used to collect the light emitted by the flame in the combustion chamber. The signals of the microphones and the photo-multiplier are acquired simultaneously on a multi-port acquisition card (National Instruments). The signals are taken during 1.6 seconds for the PIV measurements at a rate of 16 kHz.

4.2.3 Experimental apparatus

The gas turbine model combustor used in this study was originally developed as a multi-injection burner and the different stabilization processes were investigated [106, 112]. The experimental injector is composed of two stages: the pilot stage and the take-off stage. In each stage, air is injected through a swirler to provide a rotational movement to the flow and to ensure a better mixing.

A schematic view and a picture of the injection device are given in Fig. 4.2. In the present study, only the primary (pilot) stage is used to generate a swirl-stabilized flame while air is provided through both stages. The pressurized nozzle generates a solid cone spray and fuel can be injected at a maximum flow rate of 6.3 l/h. Its flow number is equal to 1.4 $\text{lh}^{-1}\text{bar}^{-0.5}$. The maximum angle of the nozzle does not exceed $50°$. The air swirler of the pilot stage is composed of 18 vanes, 6 mm wide each and inclined at an angle of $42°$. The inner and outer diameters of the swirl are respectively 30 mm and 45 mm. The inner diameter of the pilot mixing area is 15 mm as indicated in Fig. 4.2. It is geometrically designed so that 13 % of the global air rate flows through this stage. Rest of air is injected through take-off stage. A swirler composed of 20 equally spaced vanes, 10 mm

wide and inclined at an angle of $34°$. The inner and outer diameters of the swirl are respectively 55 mm and 75 mm. The inner diameter of the pilot mixing area is 50 mm as indicated in Fig. 4.2.

The resulting mixture enters a rectangular combustion chamber ($500 \times 150 \times 150$ mm^3), composed of two silica windows for optical access and two water-cooled walls. The water flow rate is regulated so that the water exit temperature remains constant for all operating conditions. The swirl number S is close to unity [24] based on geometrical considerations. Preheat temperature of the air is 473 K.

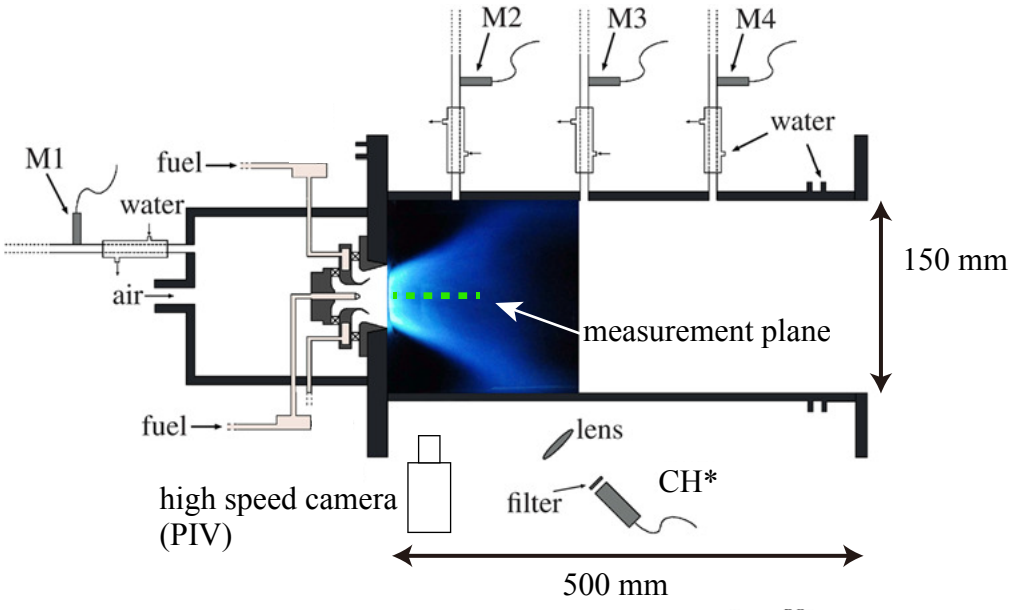

Figure 4.1: Schematic view of the experimental setup.

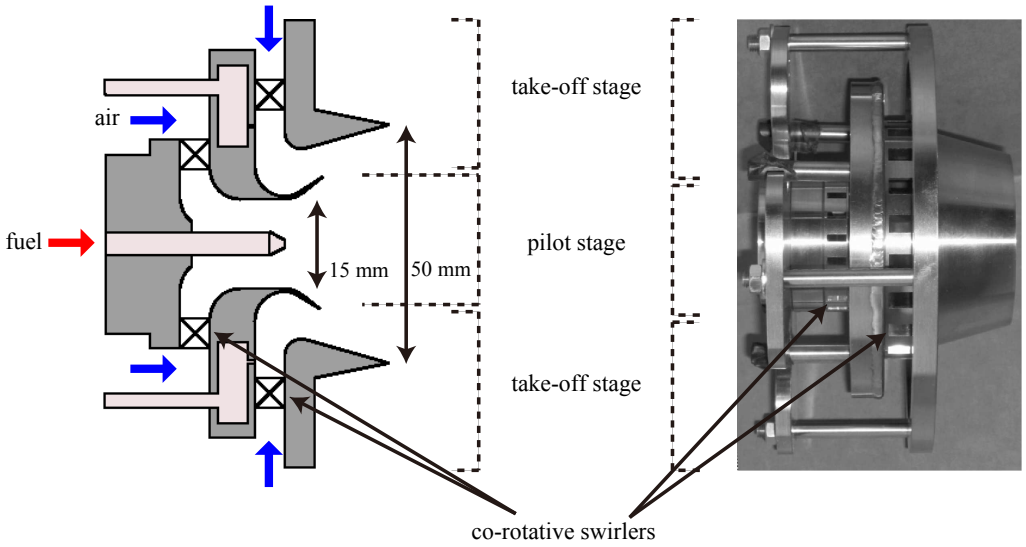

Figure 4.2: Schematic view and photo of the injection device.

4.3 Conditions

Table 4.1 shows the experimental conditions. To investigate the effect of equivalence ratio on the instability, the measurements are conducted by changing equivalence ratio in the ϕ = 0.4 to 0.7 range. There are two ways to change equivalence ratio: decreasing air and increasing fuel. Therefore, there are two series of data set.

For the first one, the global air flow rates are constant ($FC_{40} \sim FC_{70}$) and the amount of fuel is varied with the constant global air flow field while the equivalence ratio is varied from 0.4 to 0.7. The other is that the amount of fuel is kept constant ($PC_{40} \sim PC_{70}$), keeping the power produced by the burner constant. Note that FC_{50} and PC_{50} are both same air flow condition and fuel injection. As a reference, measurements are also conducted with non-reactive cases with both same air flow and same fuel injection as FCs and PCs.

The power produced by the burner is calculated from fuel mass flow rate and lower heating value (LHV) of dodecane, which is $44,240$ kJ·kg^{-1}.

Table 4.1: Operating conditions

ϕ		$\dot{m}_a$ $[g \cdot s^{-1}]$	$\dot{m}_f$ $[g \cdot s^{-1}]$	Pw $[kW]$		$\dot{m}_a$ $[g \cdot s^{-1}]$	$\dot{m}_f$ $[g \cdot s^{-1}]$	Pw $[kW]$
0.40	PC_{40}	40.4	1.02	45.2	FC_{40}	32.3	0.819	36.2
0.45	PC_{45}	35.9	1.02	45.2	FC_{45}	32.3	0.921	40.7
0.50	PC_{50}	32.3	1.02	45.2	FC_{50}	32.3	1.02	45.2
0.55	PC_{55}	29.4	1.02	45.2	FC_{55}	32.3	1.13	49.7
0.60	PC_{60}	26.9	1.02	45.2	FC_{60}	32.3	1.23	54.2
0.65	PC_{65}	24.9	1.02	45.2	FC_{65}	32.3	1.33	58.7
0.70	PC_{70}	23.1	1.02	45.2	FC_{70}	32.3	1.43	63.2

4.4 Analytical techniques

In the investigation on combustion dynamics, post-processing tool to filter or project data to extract coherent components is essential since turbulent and chemical quantities are experimentally or numerically obtained as two- or three-dimensional time discrete datasets.

The aim of this section is to describe the analytical techniques used in this study. Section 4.4.1 describes spectral analysis which is used to extract temporal information, followed by the basic theory of DMD in Sec. 4.4.2 and multi-parameter DMD in Sec. 4.4.3.

4.4.1 Spectral analysis

All time-resolved signals are analyzed either through a Fast Fourier Transform or by computing the Power Spectral Density (PSD) to obtain the spectral content. The PSD is computed using the Welch method, Hamming window with 50% overlap. The number of periodograms and blocks depend on the number of samples.

4.4.2 Dynamic mode decomposition (DMD)

As shown in Chap. 3, POD analysis is widely used to extract energetic structures from the numerical and experimental datasets. However, POD has limitations in choosing dynamically active modes since the time component is generally not resolved.

Dynamic Mode Decomposition (DMD) is one of the most recent post-processing, which can decompose time-resolved measurements into dynamically dominant structures. DMD is firstly shown by Schmid and Sesterhenn [113] and followed by Rowley et al. [114]. The dynamic decomposition is based on the Koopman modes [114] to extract modes from the data snapshots. The each mode is associated to a unique frequency. This is a large advantage of DMD since one of the major interest is to separate phenomena occurring at different frequencies. The

extracted information is referred as a generalization of global stability modes that can be used to characterize the dynamics of a system.

In this study, DMD algorithm that is introduced by Schmid [115, 116] is applied to the time-resolved data to investigate combustion dynamics.

With time discrete n datasets, a snapshot sequence, given by a matrix $\boldsymbol{X}_n$ can be defined as,

$$\boldsymbol{X}_n = \{\boldsymbol{x}_1, \boldsymbol{x}_2, ..., \boldsymbol{x}_n\}, \tag{4.1}$$

where $\boldsymbol{u}_i$ denotes the i th data of the snapshot. DMD assumes the existence of a linear mapping $\boldsymbol{A}$ connects a snapshot data $\boldsymbol{x}_i$ to the subsequent snapshot $\boldsymbol{x}_{i+1}$, that is,

$$\boldsymbol{x}_{i+1} = \boldsymbol{A}\boldsymbol{x}_i. \tag{4.2}$$

It is also assumed that this mapping is constant over the full sampling interval. The defined sequence in Eq. (4.2) can be formulated as a Krylov sequence,

$$\boldsymbol{X}_n = \left\{\boldsymbol{x}_1, \boldsymbol{A}\boldsymbol{x}_1, \boldsymbol{A}^2\boldsymbol{x}_1, ..., \boldsymbol{A}^{n-1}\boldsymbol{x}_1\right\}. \tag{4.3}$$

The goal of DMD is the extraction of the dynamic characteristics, such as eigenvalues and eigenvectors, of the dynamics process described by $\boldsymbol{A}$.

The second assumption, which is made in DMD algorithm is that the vectors given in Eq. (4.2) becomes linearly dependent in the case with sufficient number of snapshots, which can capture the dominant features of the underlying physical process. Beyond a critical number of snapshots, the vector $\boldsymbol{x}_n$ can be expressed as a linear combination of the previous vectors $\boldsymbol{x}_i, (i = 1, \ldots, n-1)$, that is,

$$\boldsymbol{x}_n = a_1\boldsymbol{x}_1 + a_2\boldsymbol{x}_2 + \ + a_{n-1}\boldsymbol{x}_{n-1} + \boldsymbol{r} \tag{4.4}$$

or in matrix form

$$\boldsymbol{x}_n = \boldsymbol{X}_{n-1}\boldsymbol{a} + \boldsymbol{r} \tag{4.5}$$

where $\boldsymbol{r}$ is the residual vector and $\boldsymbol{a}^T = \{a_1, a_2, ..., a_{n-1}\}$. From Eq. (4.2) and (4.5),

$$\begin{aligned}\boldsymbol{A}\boldsymbol{X}_{i-1} &= \boldsymbol{X}_i \\ &= \{\boldsymbol{A}\boldsymbol{x}_1, \boldsymbol{A}\boldsymbol{x}_2, \ldots, \boldsymbol{A}\boldsymbol{x}_{i-1}\} \\ &= \{\boldsymbol{x}_2, \boldsymbol{x}_3, \ldots, \boldsymbol{X}_{i-1}\boldsymbol{a} + \boldsymbol{r}\} \\ &= \boldsymbol{X}_{i-1}\boldsymbol{S} + \boldsymbol{r}\boldsymbol{e}_{i-1}^T\end{aligned}$$

where e_{i-1}^T is the $(n-1)$ th unit vector and the matrix $\boldsymbol{S}$ is a companion matrix of order $i \times i$,

$$\boldsymbol{S} = \begin{pmatrix} 0 & & & & a_1 \\ 1 & 0 & & & a_2 \\ & \ddots & \ddots & & \vdots \\ & & 1 & 0 & a_{i-2} \\ & & & 1 & a_{i-1} \end{pmatrix}. \tag{4.6}$$

The eigenvalues of $\boldsymbol{S}$ are a subset of the eigenvalues of $\boldsymbol{A}$ and the matrix $\boldsymbol{S}$ is computed as follows: the last snapshot of the data sequence, $\boldsymbol{x}_n$ is expressed as a linear combination of the previous dataset as shown in Eq. (4.5). Its least-square solution, for a full-rank matrix $\boldsymbol{X}_{i-1}$, is given by the economy-size QR-decomposition of the data sequence $\boldsymbol{X}_{i-1}$ as,

$$\boldsymbol{a} = \boldsymbol{R}^{-1}\boldsymbol{Q}^H\boldsymbol{x}_i, \tag{4.7}$$

where $\boldsymbol{Q}\boldsymbol{R} = \boldsymbol{X}_{i-1}$. The vector $\boldsymbol{a}$ forms the last column of the companion matrix $\boldsymbol{S}$. The dynamic modes $\boldsymbol{\phi}$ and respective angular frequencies λ are extracted from $\boldsymbol{S}$ through the expression:

$$\boldsymbol{\phi_i} = \boldsymbol{X_{i-1}}\boldsymbol{v_i} \tag{4.8}$$

$$\lambda_i = \arg(\mu_i)F_s \tag{4.9}$$

where v_i is the i th eigenvector of the matrix $\boldsymbol{S}$, μ_i is the i th eigenvalue and F_s is the sampling rate. μ_i are referred as Ritz value and are logarithmically mapped

on to the complex plane, such that their real part represent exponential growth or decay (depending on the sign) and the imaginary part contain the temporal frequency as Eq. 4.9.

4.4.3 Multi-variable DMD

In turbulent combustion, turbulent flame structures have strong interaction with flow field. To resolve the combustion dynamics numerically and experimentally, acquiring multi-variables such as intermediate species and radical distribution, flow field and acoustic pressure fluctuation. In two-phase combustion specifically, data concerning the liquid distribution, acoustics and heat release may be exploited to investigate the combustion dynamics. As is discussed by Richecoeur et al. [117], one way to improve the detection of coherent structures may be to combine the data. To detect coherent structure in different variables, they used multi-variable DMD algorithm combining the data obtained by multi-variable diagnostics. In this study, the multi-variable DMD is applied to the reactive turbulent flows and its capability is shown.

In this method, the data matrix $\boldsymbol{X}_i$ is composed of a superposition of different variables (velocity field, Mie scattering intensity, pressure fluctuation, ...) placed one after the other as illustrated in Fig. 4.3. The obtained dynamic modes are common to all the variables. Thus, it describes not only one variable dynamics but also the whole system dynamics.

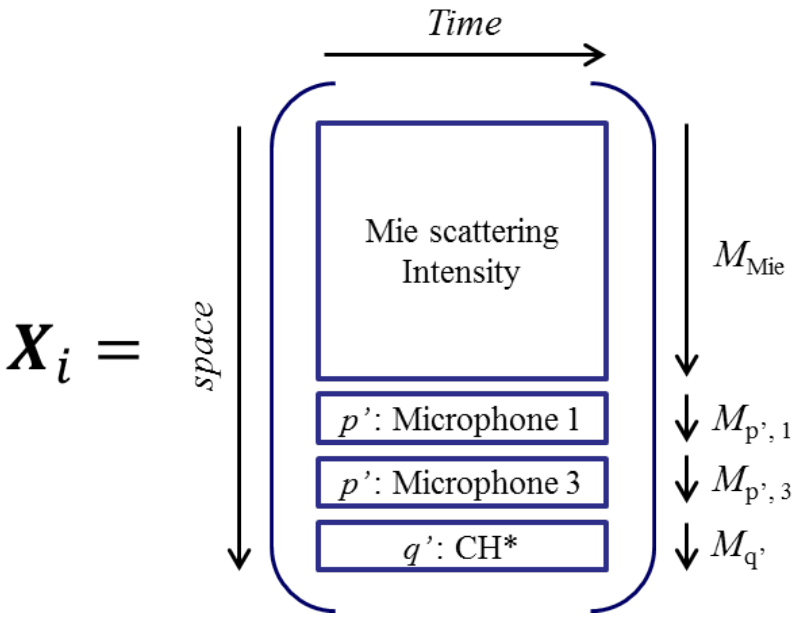

Figure 4.3: Schematic of data matrix in the multi-variable DMD.

4.5 Characterization of global flame and flow structure, and acoustic behavior

4.5.1 Flames and droplets structure

The mean droplet velocity field and reaction zone in the three operating conditions (FC_{40}, FC_{45} and FC_{70}) are shown in Fig. 4.4. The mean fields are computed using 5000 images for each operating condition. Contour line of the velocity magnitude is superimposed on the natural emission, which indicates mean reaction-zone location. Although the droplet distribution exhibits asymmetrical distribution between upper and lower half of the chamber, the mean reaction-zone location was computed from mean line-of-sight integrated spontaneous emission intensity via an Abel deconvolution [118]. It reveals the flame structure on a plane across the axis of the combustor. The droplet velocity is only computed in the region where the droplet's Mie scattering intensity signal shows averagely significant value. For all condition within this measurement, V-shape flame is anchored inside the injection device where intense reaction takes place. Increasing equivalence ratio, the droplet becomes widely spread and the mean reaction-zone shifting downstream region.

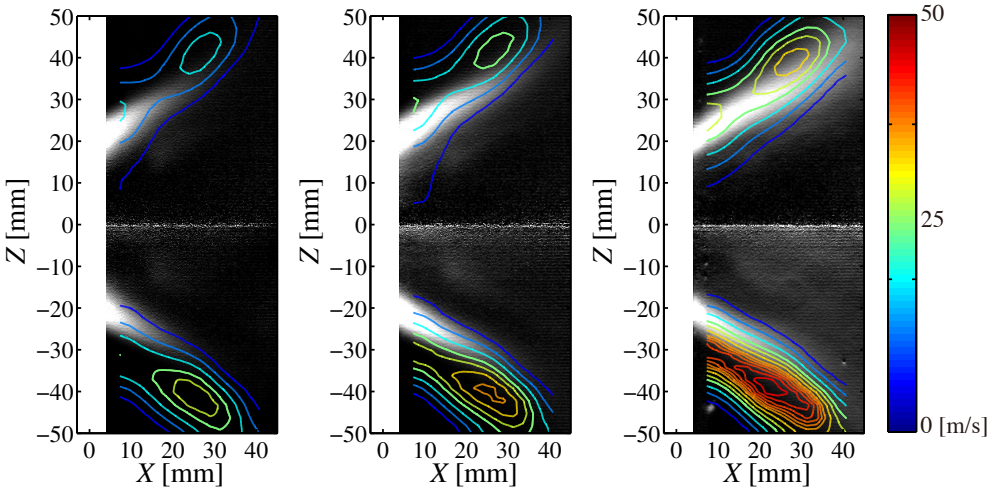

Figure 4.4: The mean velocity field and reaction zones in the three operating conditions (FC_{40}, FC_{50} and FC_{70} in order from the left). Contour line of the velocity magnitude is superimposed on the mean reaction-zone location with gray-scale. The mean reaction-zone location was computed via an Abel deconvolution of the mean line-of-sight integrated natural emission intensity.

4.5.2 Frequency characteristics of acoustic pressure and heat release rate fluctuations

To investigate the evolution of frequency characteristics, the acoustic pressure (M1, M3 and M4) and heat release rate fluctuation (CH^*) are measured in long duration (64 seconds at 16 kHz) with continuously changing condition. The original $2^{14} \times 64$ point data is split up into 1023 data segments, each of length 2048 with 50% overlap, therefore the spectral resolution is 8 Hz.

Figure 4.5 shows power spectra of CH^* intensity (a and b) and acoustic pressure measured by M3, which locates in the middle of the combustion chamber (c and d). Left two figures show the series of data set FCs and right ones show PCs. Note that only under FC_{60} case ($\phi < 0.63$) are calculated from continuous data obtained changing condition at same sampling frequency (16 kHz). PSD of FC_{65}, FC_{70} and all the power constant conditions (PCs) are separately calculated with same spectral resolution and shown in the same figure.

For the operating condition FCs, Fig. 4.5a exhibits three peaks: relatively broad peak between 200 and 400 Hz strongly in high equivalence ratio condition, strong distinct peak around 1700 Hz and very weak one around 1300 Hz only in the low equivalence ratio conditions. The signal from M3 (Fig. 4.5c) shows stronger peak in lower frequency than in higher one. The peak around 1300 Hz is not observed in the acoustic pressure fluctuations from neither M1 nor M4. Instead there is another peak observed around 900 Hz in the higher equivalence ratio conditions. For the operating condition PCs, Figs. 4.5b and 4.5d show similar peaks in low (between 200 and 400) and middle (around 900 Hz) frequency range to those for FCs. However, the distinct peak appear in the high frequency range between 1600 and 2100 Hz.

Acoustic oscillation of the combustor

The strong peak centered around 380 Hz corresponds to the frequency of quater wavelength mode of the chamber. Providakis [119] performed an acoustic anal-

ysis of the combustor using a simplified one-dimensional model [120] and estimated the eigenfrequency range with the same combustor as used in the present study. It is assumed that the chamber temperature is 1400 K for a global equivalence ratio of 0.6 and air preheated at 473 K, using measured temperature at the chamber exit by a thermocouple and an adiabatic flame temperature obtained by a numerical simulation [121].

According to their assumption, the acoustic frequencies for the present measurement conditions can be estimated within a range of 280 to 350 Hz. Obtained frequency in the present study is slightly higher than this estimation. The estimation of the average temperature was made in a same equivalence ratio and preheat temperature as present case but different staging factor (mode of fuel entry). It is possible that the flame temperature difference attributed to the fuel distribution causes the inconsistency.

The peak is observed around 900 Hz in acoustic pressure fluctuation for both cases of FCs and PCs. This peak may not relate to aerodynamic instability but to one of the acoustic mode of chamber, plenum chamber or some parts of burner since the frequency remain nearly unaffected by the change of flow rate as shown in Figs. 4.5c and 4.5d.

Figure 4.6 presents the evolution of the sound pressure level (SPL) measured by microphones (M1, M3 and M4) as a function of equivalence ratio. SPL, denoted L_p and measured in dB is given by,

$$L_p = 10 \log_{10} \frac{p_{rms}^2}{p_0^2} [\mathrm{dB}]. \tag{4.10}$$

Here, p_{rms} is the root mean square of acoustic pressure fluctuation, and $p_0 (= 20 \times 10^{-6}$ [Pa]) is the reference sound pressure. Throughout the whole range within present study, SPL measured in plenum (M1) shows slight increase while that in combustion chamber (M3 and M4) exhibit large increase. SPL remains almost constant for the low equivalence cases, $\phi < 0.45$, increase drastically between $\phi = 0.45$ and 0.55 and exhibit constant increase in the case of $\phi > 0.55$.

Aerodynamic instability

The distinct peak around 1700 Hz (Fig. 4.5a and c) of FCs and between 1600 and 2100 Hz (Fig. 4.5b and b) of PCs in low equivalence ratio conditions represent aerodynamic instability corresponding to a helical structure. In the same combustor with different operating condition, Providakis et al. [106] conducted high-speed PIV and OH PLIF measurement on the several transverse planes in the combustion chamber. It was revealed that the helical structure precesses around the chamber axis. However, in this study the measurements are only conducted in the axial plane, thus it is not possible to examine the existence of PVC in the specific condition. Nevertheless, it can be said that the distinct peak corresponds to the helical structure with its non-axisymmetric nature, which will be shown in Sec. 4.6.3.

It has been known that the rotation frequency of the helical structure and precessing frequency in the case of PVC are a function of flow rate [22]. The rotation frequency can be estimated from geometry of the injection devices. Swirl number is defined as the ratio of the axial flux of tangential momentum to that of the axial momentum times a characteristic dimension of the swirler. Sheen et al. [122] have experimentally shown that the swirl number S is linearly proportional to the ratio of volumetric mean azimuthal ($\bar{u}_\theta$) to axial velocity ($\bar{u}$) with a radial type swirl generator, and the relation is,

$$S = \frac{3}{4}\frac{\bar{u}_\theta}{\bar{u}}. \tag{4.11}$$

Since the swirler was designed so that swirl number, S, is close to unity, one can estimate azimuthal velocities from the axial velocities as:

$$\bar{u}_\theta = \frac{4}{3}\bar{u} \tag{4.12}$$

Considering geometrical relationship, the mean velocity in the axial direction can be estimated as,

$$\bar{u} = \frac{\dot{m}}{\rho\pi(R^2 - R_p^2)} \tag{4.13}$$

where $\dot{m}$ corresponds to the mass flow, R and R_p are the internal radius of the pilot mixing area and the external radius of the pilot fuel injection, and are 7.5 and 2 mm, respectively. 13% of the mass flow rate passes through the pilot swirler so that $\dot{m} = 0.13\dot{m}_a$.

Using above relationship, the rotating frequency of the flow can be estimated as:

$$f_h = \frac{u_\theta}{2\pi R} \tag{4.14}$$

Figure 4.7 compares the estimation to the experimental value. Black circles show the frequencies obtained by the measurement of pressure and heat release rate fluctuation, while red squares are the estimated values from Eq. (4.14). A difference of 15% between the estimated and the experimental values is found. Still, this approximation gives a good order of magnitude of the expected frequency. Dotted line shows a linear regression, $f = a \times \dot{m}_a$ ($a = 50$). The rotation frequency has been measured over a wide range of air flow rate in the previous study (from 10 to 60 [g/s]) [119], and all the cases were on the line, which is consistent with the present case. Strouhal numbers, $St = 2f_h R/\bar{u}$, of the helical mode for all conditions are $St \approx 0.70$ within less than 1.5%.

From Figs. 4.5 and 4.6, one can assume that the aerodynamic instability getting weaker instead of the acoustic oscillation. In addition, the middle range frequency coincide the difference between that of these two fluctuations ($f_h - f_{ac}$) and they are only seen in the conditions where the aerodynamic oscillation strongly appear. It seems to represent the interaction between the acoustic oscillation and the helical fluctuation.

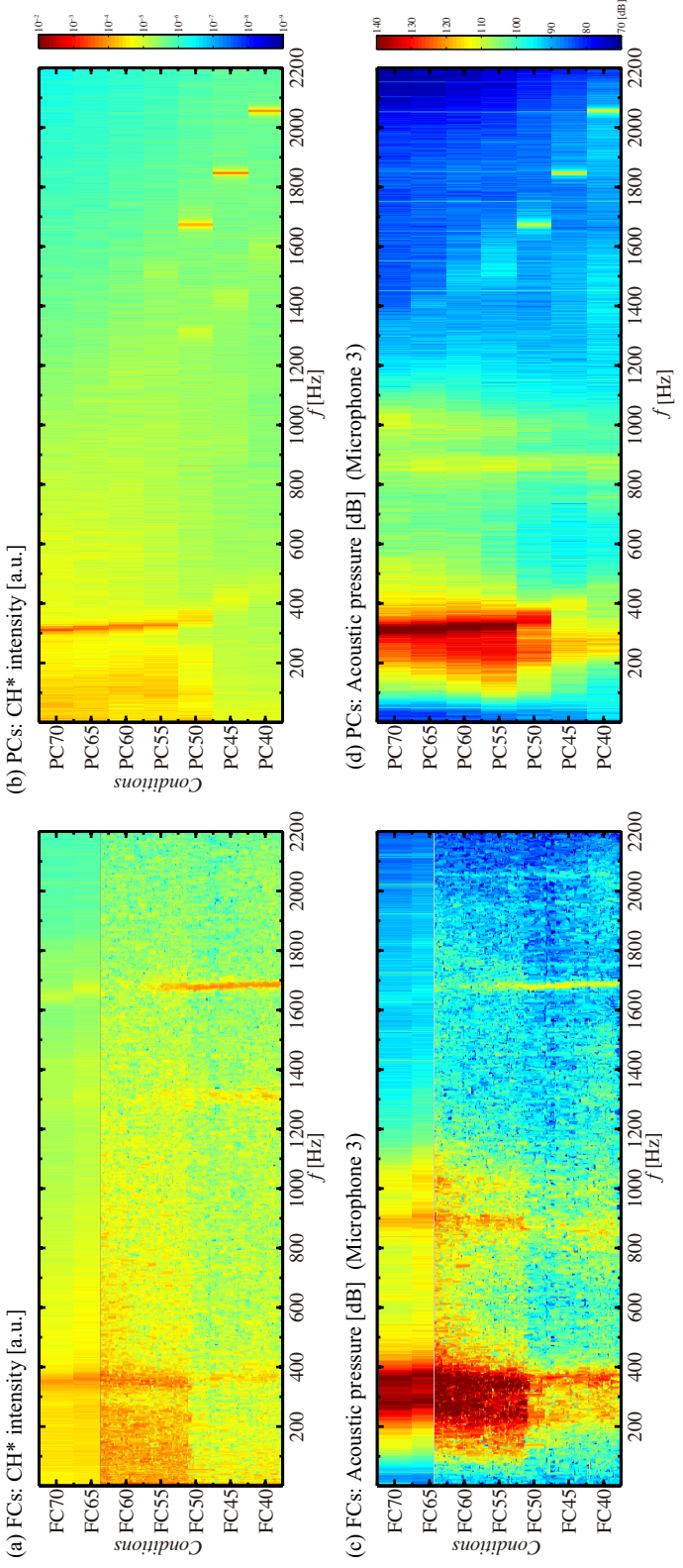

Figure 4.5: Power spectra of CH* intensity (top) and acoustic pressure measured by M3 (bottom) for the operating conditions FCs (left) and PCs (right).

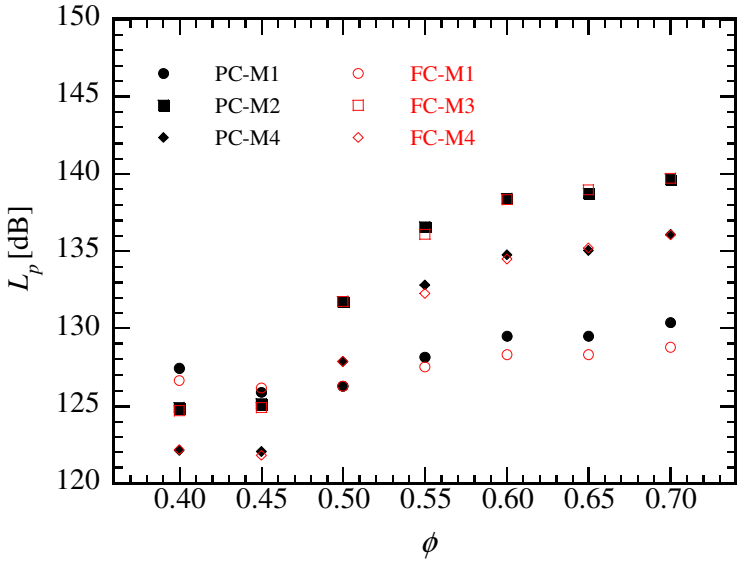

Figure 4.6: Sound pressure level of each conditions measured by M1 (plenum), M3 (in the middle of combustion chamber) and M4 (downstream of combustion chamber).

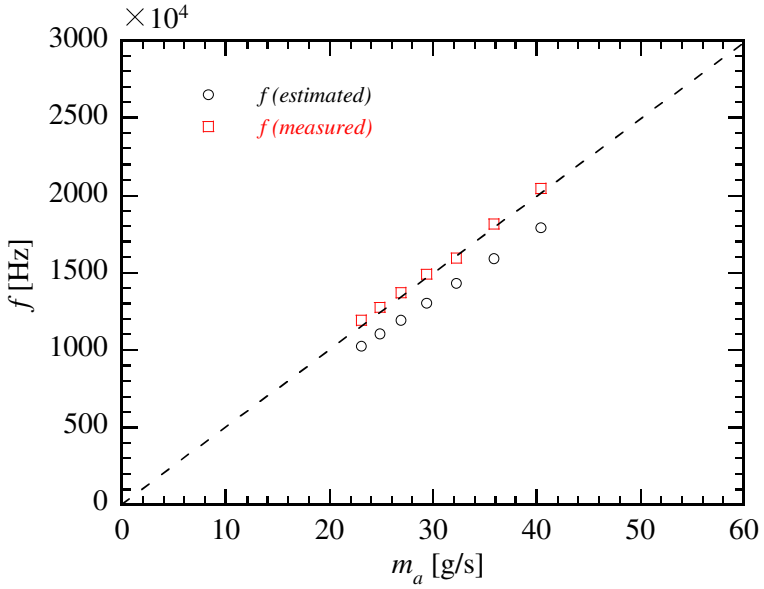

Figure 4.7: Evolution of the frequency of the aerodynamic structure as a function of the air flow rate.

4.5.3 Frequency characteristics of velocity fluctuation

Figure 4.8 shows PSD of velocity fluctuation near the nozzle exit ($X = 12$ mm, $Z = -27$ mm) for two operating conditions (FC_{40} and FC_{70}) with fixing the global air flow rate at 32.3 g/s. In the lowest equivalence ratio condition (FC_{40}, Fig. 4.8a), the distinct peak is seen at $f_h = 1680$ Hz, which is the same frequency as the one observed in the heat release and acoustic pressure fluctuation (Figs. 4.5a and 4.5c). With increasing equivalence ratio, the peak corresponding aerodynamic fluctuation is getting weaker and broader. In the highest equivalence ratio condition (FC_{70}) shown in Fig. 4.8b, there still exist peak around f_h, which is not observed in the heat release and acoustic pressure fluctuation. In addition, one can see a strong but relatively broad peak centered at $f_{ac} = 283$Hz.

The spectra show similar tendency in the case with constant power produced by burner ($PC_{40} \sim PC_{70}$). The spectral analysis on velocity fluctuation also reveals same tendency that aerodynamic instability seems to be strong in lower equivalence ratio conditions and getting weaker with equivalence ratio increase. However, the frequency a characteristic of velocity fluctuation strongly depends on the location of the data is taken. It has been revealed that the helical structure is formed just after the nozzle exit and propagates downstream [123, 124]. Thus, the peak corresponding to the helical oscillation does not appear when the spectral analysis is performed in the downstream region.

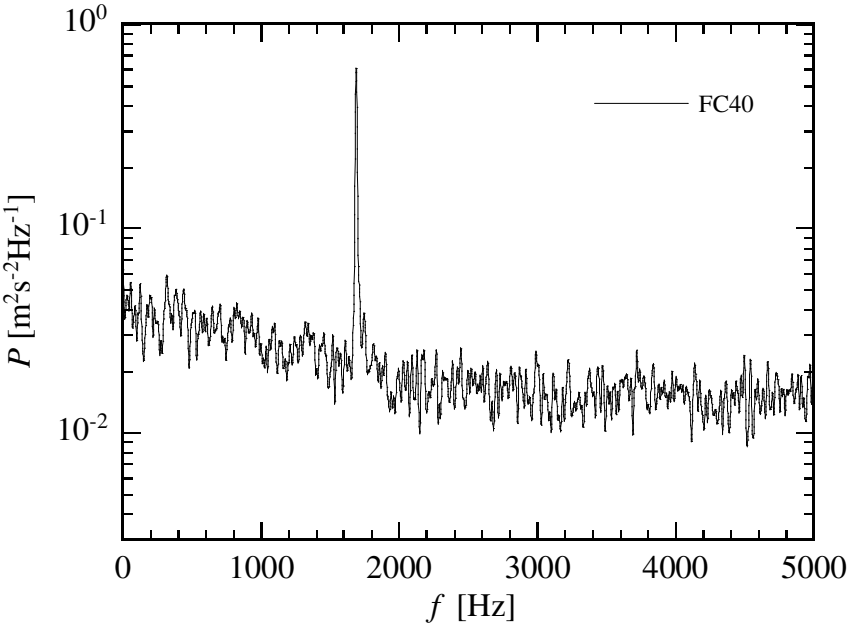

(a) Operating condition: FC_{40}

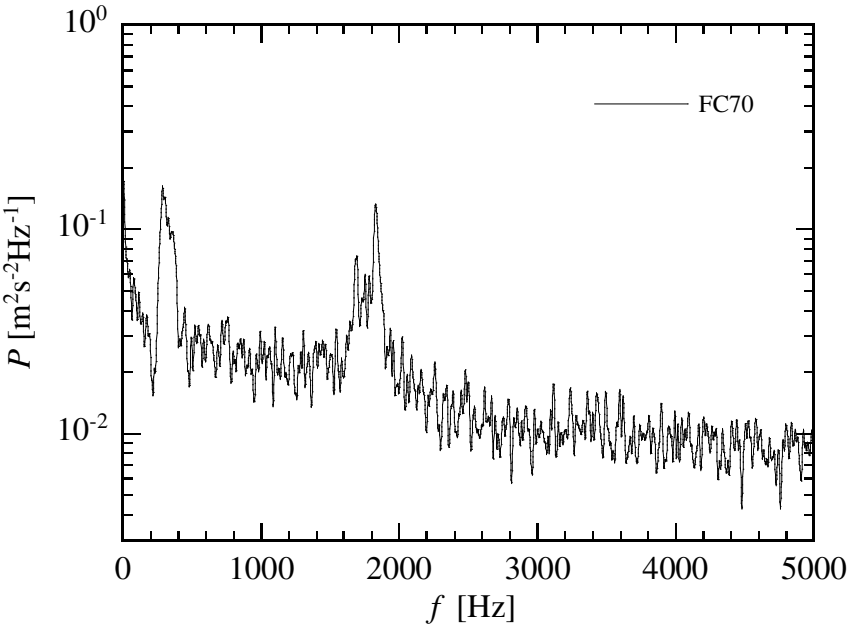

(b) Operating condition: FC_{70}

Figure 4.8: PSD of velocity fluctuation near the nozzle exit (X = 12 mm, $Z = -27$ mm) for two operating conditions (a) FC_{40} and (b) FC_{70}.

4.6 Optimal dynamic modes in the swirl-stabilized combustor

The DMD technique is able to optimally identify and extract the dynamically most relevant structures. The temporal information is contained in the frequency as Eq. (4.9), while the spatial information is expressed as dynamic modes as Eq. (4.8).

4.6.1 Optimization of conditions

According to Schmid [116], the principal values of the algorithm are the time separation between the snapshot, Δt, and the number of processed snapshots, N_s. In addition, the sample images are reduced F_r times from its original size. Since experimental data is used for this analysis, there is an effect of measurement noise. The resize process can reduce the noise as well as the computational time while too large value of F_r causes a lack of spatial resolution. The aim here is to optimize the analysis conditions by determining the values such as time separation, number of samples and resize factor.

Time separation, Δt, can be determined by considering the time-scale of the phenomena of interest and Nyquist frequency, f_n. In this sturdy, the highest frequency that is investigated is that of the helical mode and about 2 kHz, which is less than half of f_n ($= 5$ kHz in the PIV and Mie scattering measurement). Consequently, it is proper to set the time separation of $\Delta t = 1/f_n = 0.2$ ms. The number of samples (N_s) are set to resolve the mode associated to acoustic oscillation ($f_{ac} \approx 380$ Hz) and to helical structure ($f_h \approx 1600$ Hz in the operating condition FCs) at lowest.

DMD analysis is applied to the Mie scattering distribution varying N_s and F_r. The 1.5 seconds measurement data is divided into separate blocks that have N_s snapshots each. Then the DMD technique is applied to these blocks as if they were different datasets but for the same flow and spray condition. Convergence of DMD is evaluated in terms of L_2 norm of residual $\boldsymbol{r}$, which is defined as Eq. (4.5). In Fig. 4.9, the L_2 norm of the residual is shown as a function of number

of samples and resize factor. Note that the residual is logarithmic. The residual decreases with increasing both N_s and F_r.

Spectral resolution, Δf, is known as a variable in DMD. When a mode is distinct and well defined, the local spectral resolution around the frequency tends to be small. It is then important to check Δf around the frequency of interest. Figure 4.10 shows the effects of N_s on the mean and local spectral resolution around the frequency of helical structure with operating condition FC_{40}. Colored markers represent the local resolution with different resize factors. The mean frequency resolution constantly decreases with an increase of the number of samples as classical manner shown as black solid line (F_s/N_s, where Fs is the sampling frequency). However, the local spectral resolutions disperse and depend on resize factor. In the case of $F_r = 1$, which is a raw image, local spectral frequencies are even higher than mean spectral resolution. In some cases in $F_r = 16$, one can see the local spectral resolution much smaller than the average.

From this observation with consideration of spatial resolution, N_s and F_r are chosen as 500 and 4, respectively. In the following analysis, the local frequency resolution around the frequency of interest is about 20 Hz. It is known that Δf also depends on the last snapshot especially when using an experimental data [125]. Even with same N_s and F_r, it shows sometimes smaller or larger value. In this study, the results obtained from 30 data blocks that have 500 snapshots each are investigated.

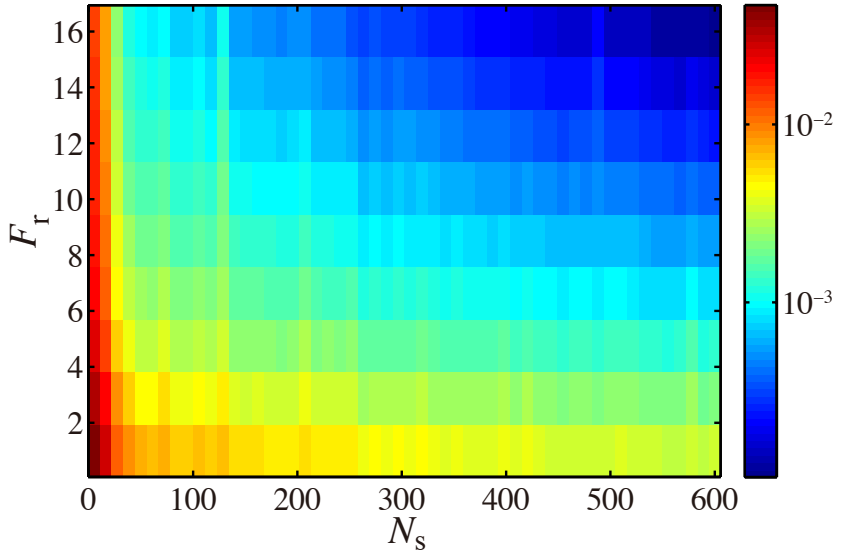

Figure 4.9: Residual of the DMD calculation as a function of Number of samples and resize factor.

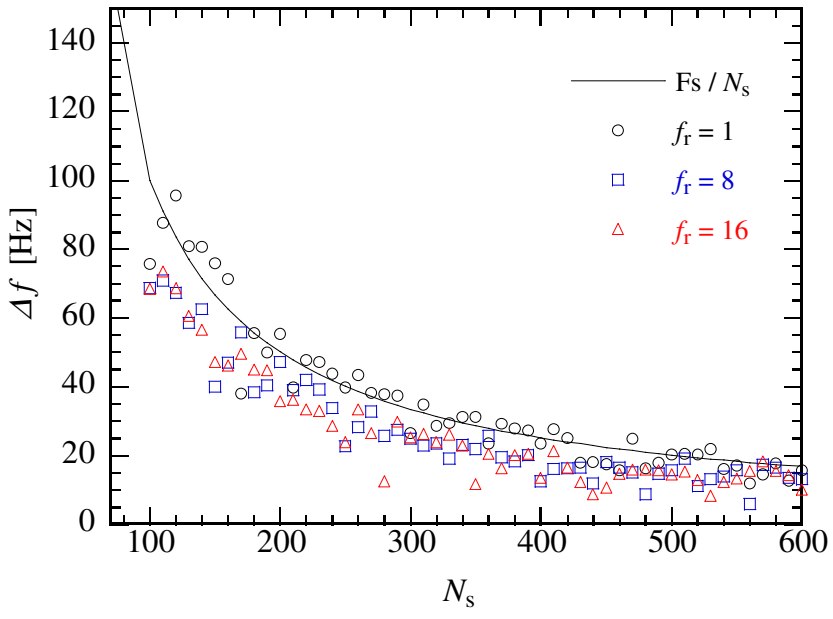

Figure 4.10: Effects of the number of samples on local spectral resolution around the frequency corresponding to the helical mode. The mean frequency resolutions are plotted as a reference with solid line.

The following analysis in this section focuses on two operating conditions: ϕ = 0.40 case (FC_{40}) and ϕ = 0.70 case (FC_{70}) with keeping air flow constant with the object of demonstrating the capability of the DMD analysis to extract dynamically dominant phenomena.

4.6.2 Single-variable DMD on Mie scattering intensity and velocity field

Single-variable DMD described in Sec. 4.4.2 is applied to Mie scattering intensity and velocity field. The relevance of each dynamic mode can be quantified by computing the amplitude of each structure as, $\|\phi_i\|$ and corresponding frequency is $\lambda_i/2\pi$.

In Fig. 4.11, the amplitude spectra of the DMD on Mie scattering intensity for two operating conditions are displayed for FC_{40} (Fig. 4.11a) and for FC_{70} (Fig. 4.11b). One can see a strong peak at same frequency ($f_h = 1690$ Hz) which is observed in spectral analysis of velocity fluctuation (Fig. 4.8a). In the case of FC_{70}, strong peak at acoustic frequency is seen in the spectral analysis in acoustic pressure, heat release fluctuation and velocity fluctuation. However, in DMD analysis on Mie scattering shown in Fig. 4.11b, the peak at frequency associated to acoustic instability cannot be strongly seen. This might be caused by the fact that the fuel droplets only present in upstream region just after nozzle exit where strong helical structure are found. Even though the peak height of the dynamic modes is smaller in the case of FC_{70}, it is not possible to compare it quantitatively from that of other cases. Mie scattering intensities are proportional to the size and the density of droplets, which differ from case to case.

In Fig. 4.12, the amplitude spectra of the DMD on velocity field of case FC_{40} and FC_{70} are shown. As expected from the result of Mie scattering intensity distribution, the amplitude spectrum of the DMD on the velocity field detected distinct peaks at frequency associated to the helical instability for both cases. However, a peak corresponds to the acoustic oscillation cannot be observed.

As is mentioned in Sec 4.6.1, the eigenvalues of $\boldsymbol{S}$ is referred as Ritz value, μ_i, its absolute value represents exponential growth ($|\mu_i| > 1$) or decay ($|\mu_i| < 1$). A unit magnitude hence represents stationary mode amplitude. Fig. 4.13 compares Ritz value of DMD on the Mie scattering intensity distribution (black circles) and on the velocity field (red squares). The operating condition is FC_{40} and the data sequences acquired at same timing are used for both cases. All dynamic modes obtained from velocity field except Mode 0, which is assumed the mean flow field [115], are decaying ($|\mu_i| < 1$). On the other hand, the majority of them cluster on the unit circle in Mie scattering intensity data, which indicate the dynamic processes are in an equilibrium state [114]. The inconsistency between these two despite the fact that same physical phenomena are used for both cases is probably attributed to a lack of spatial resolution. The velocity is calculated using PIV algorithm with 48 pixel interrogation window and obtained every 16 pixels. Consequently, the spatial resolution is not same between Mie scattering and velocity magnitude.

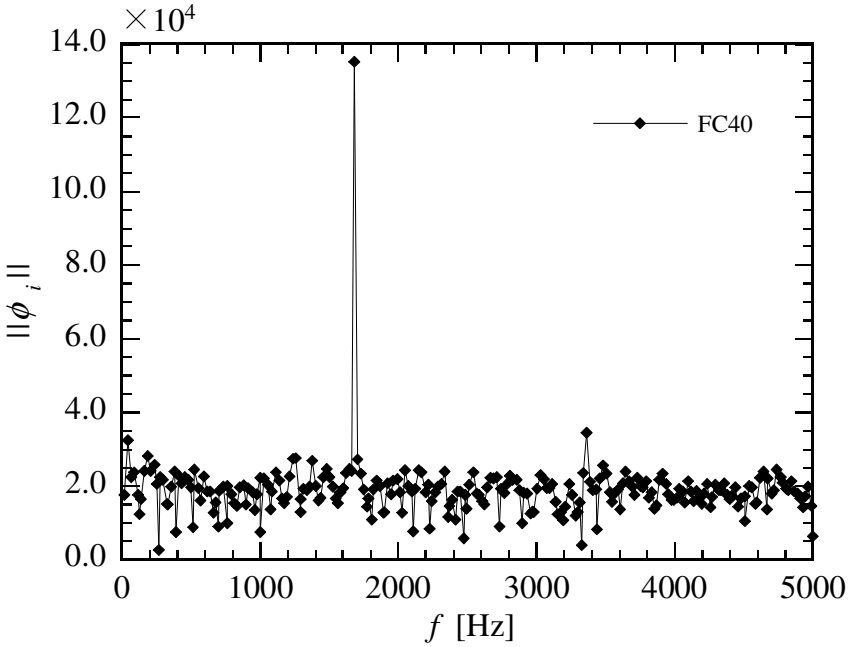

(a) Operating condition: FC_{40}

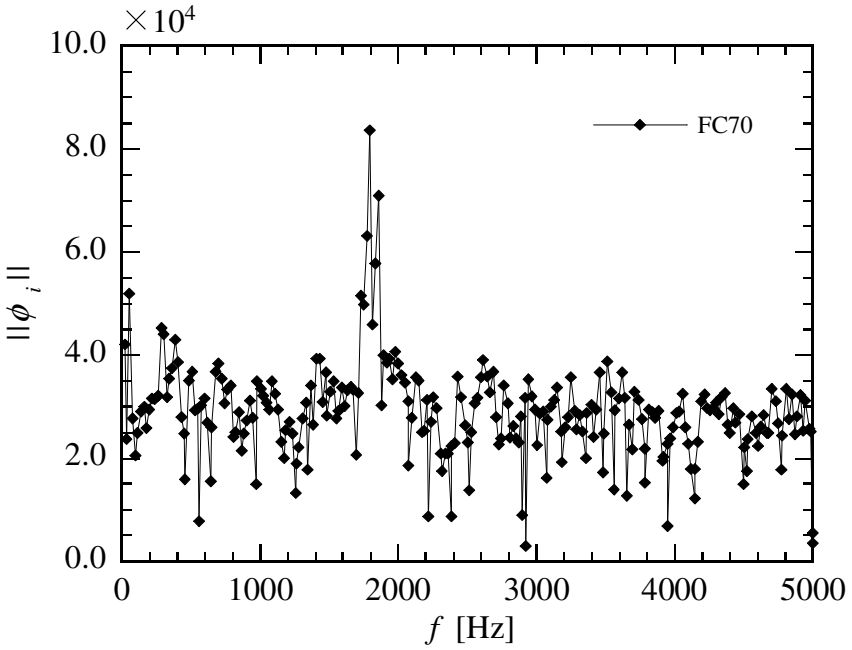

(b) Operating condition: FC_{70}

Figure 4.11: Amplitude spectra of DMD on Mie scattering intensity for two operating conditions (a) FC_{40} and (b) FC_{70}.

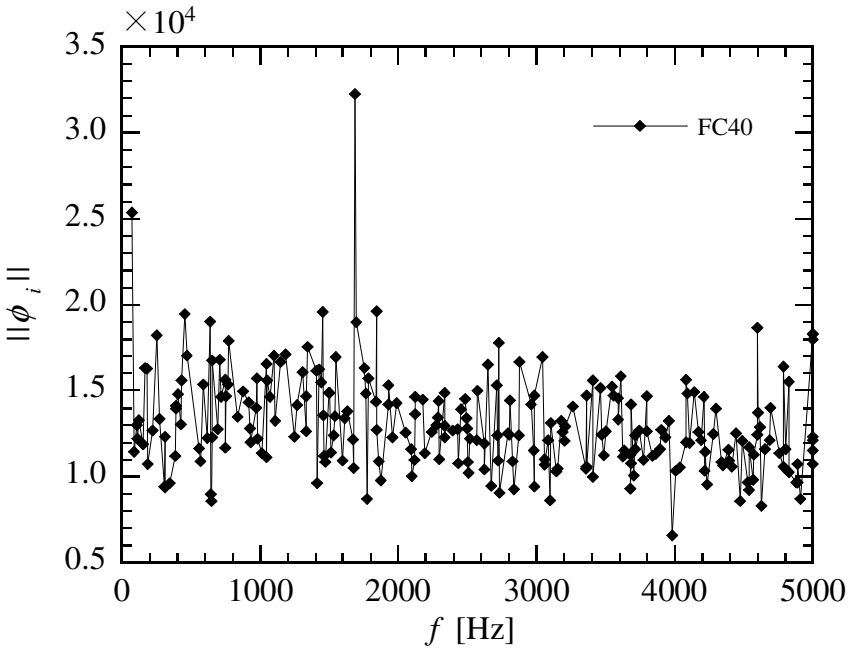

(a) Operating condition: FC_{40}

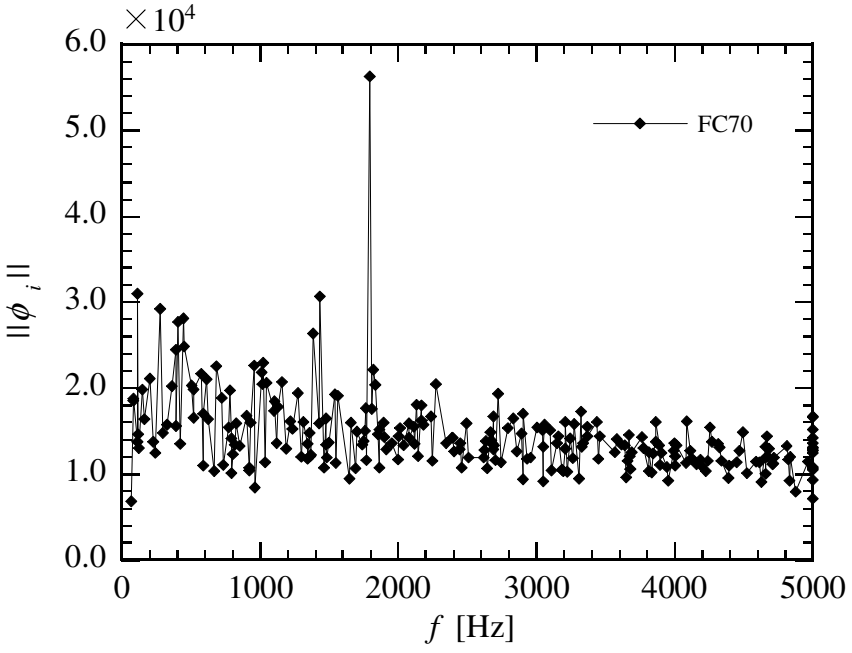

(b) Operating condition: FC_{70}

Figure 4.12: Amplitude spectra of DMD on velocity fields for two operating conditions (a) FC_{40} and (b) FC_{70}.

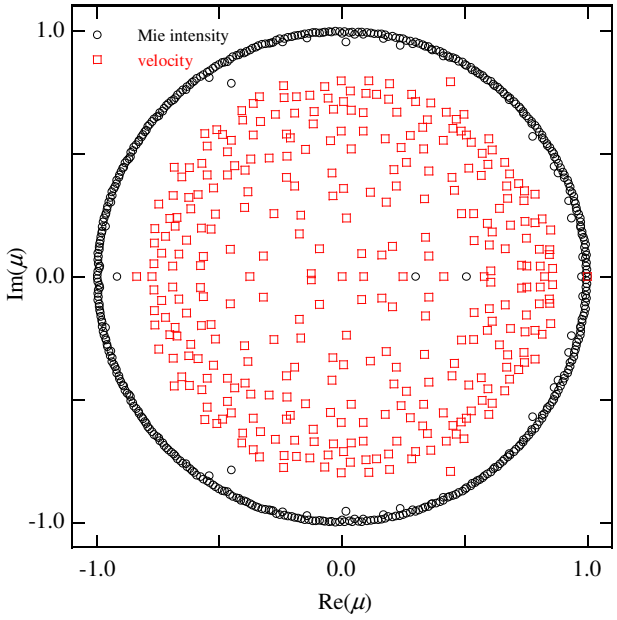

Figure 4.13: Ritz value obtained by DMD analysis with Mie scattering intensity distribution (black circles) and velocity fields (red squares) with operating condition FC_{40}.

4.6.3 Multi-variable DMD

As mentioned in section 4.4.3, one can use the multi-variable DMD algorithm to detect coherent structure in different variables. In present study, multi-variable DMD is applied to the Mie scattering intensity distribution, simultaneously measured acoustic pressure at plenum (M1) and the middle of combustion chamber (M3) and heat release rate fluctuation (CH^*). The analysis condition such as number of samples and resize factor are set to be same as the single variable DMD such that $N_s = 500$ and the Mie images are reduced by $F_r = 4$, respectively.

In Fig. 4.14, the amplitude spectra of the multi-variable DMD of case FC_{40} and FC_{70} are displayed. The spectrum in the lowest equivalence ratio case (4.14a) shows a narrow strong peak at $f_h = 1690$ Hz and a low peak at 280 Hz, which is not observed in the single variable DMD on Mie scattering intensity. The amplitude of the peak associate to aerodynamic fluctuation decreases relative to that of acoustic one with increasing equivalence ratio. In the highest equivalence ratio case (Fig. 4.14b), the spectra reveals high amplitude and relatively wide peak at 288 and 320 Hz which may represent the one observed from PSD of local velocity magnitude ($f_{ac} = 308$ Hz).

The both modes, which are of interest in the present study, associate to acoustic and aerodynamic oscillation can be detected by multi-variable DMD. Their characteristics will be investigated using this technique in the following section.

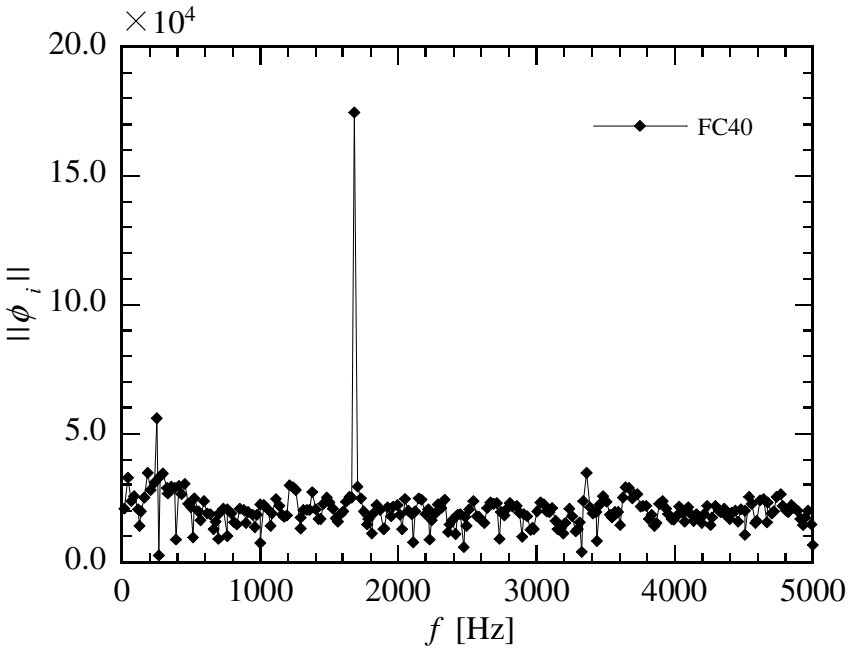

(a) Operating condition: FC_{40}

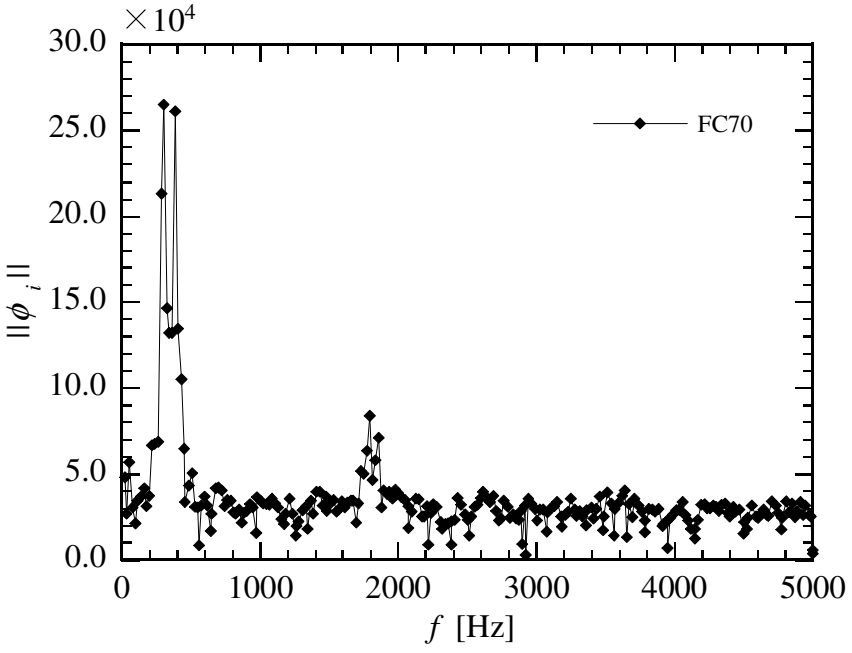

(b) Operating condition: FC_{70}

Figure 4.14: Amplitude spectra of multi-variable DMD on Mie scattering intensity, acoustic pressure and heat release fluctuation for two operating conditions (a) FC_{40} and (b) FC_{70}.

Spatial distribution of dynamic mode

Figures 4.15 and 4.16 show a cycle of reconstructed DMD mode associated to the frequency of aerodynamic instability mode oscillation every 45° for the case FC_{40} as a example of the case in which aerodynamic instability is a dominant, and for the case FC_{70} as a example of the case in which acoustic instability is a dominant. The corresponding frequency is approximately 1690 Hz for FC_{40} and 1720 Hz for FC_{70}. Although acoustic pressure and heat release fluctuation data are also used for the multi-variable DMD analysis, the DMD mode is reconstructed only on Mie scattering data. Red regions represent positive value and blue region is negative. Contours of 25% Mie scattering intensity (black line) are added.

Although lower half of the mode is shown here, all conditions present an opposite behavior between the lower and upper region of the chamber. It represents the asymmetric structure of the helix on the axial plane. In the strong helical oscillation condition (Fig. 4.15), the structure lines up alternatively in the direction of the jet injection. The spatial distribution of the mode is very similar within all low equivalence ratio conditions ($FC_{40,45,50}$ and $PC_{40,45,50}$). On the other hand, each spatial cell (positive or negative) of the strong acoustic oscillation condition (FC_{70}, Fig. 4.16) extends in length towards downstream. Whole structure also stretches and penetrates into deeper region in the chamber. Increasing equivalence ratio lead to the higher flame temperature, rapid evaporation and then better fuel–air mixing. In addition, higher gas temperature causes stronger gas expansion. These phenomena may help fuel jet and mean reaction zone penetrate into deeper region of the combustion chamber.

In the same flow and droplet condition with non-reacting flow, spatial distribution of dynamic modes associated to helical structure do not alter much between the conditions. The change in the distribution will be further investigated in the next section.

Figure 4.17 shows reconstructed DMD mode associated to the frequency of acoustic mode. For this case, opposite half is symmetric. Instead of the alterna-

tive structure in the case of helical oscillation mode, each structure reaches deeper region and the fluctuating cycle shows oblique oscillation. The thermoacoustic instability corresponding to the quarter-wave mode of the combustion chamber induces longitudinal acoustic oscillation. As a result, the dynamic mode indicates that oblique angle of the liquid fuel spray is perturbed with the characteristic frequency.

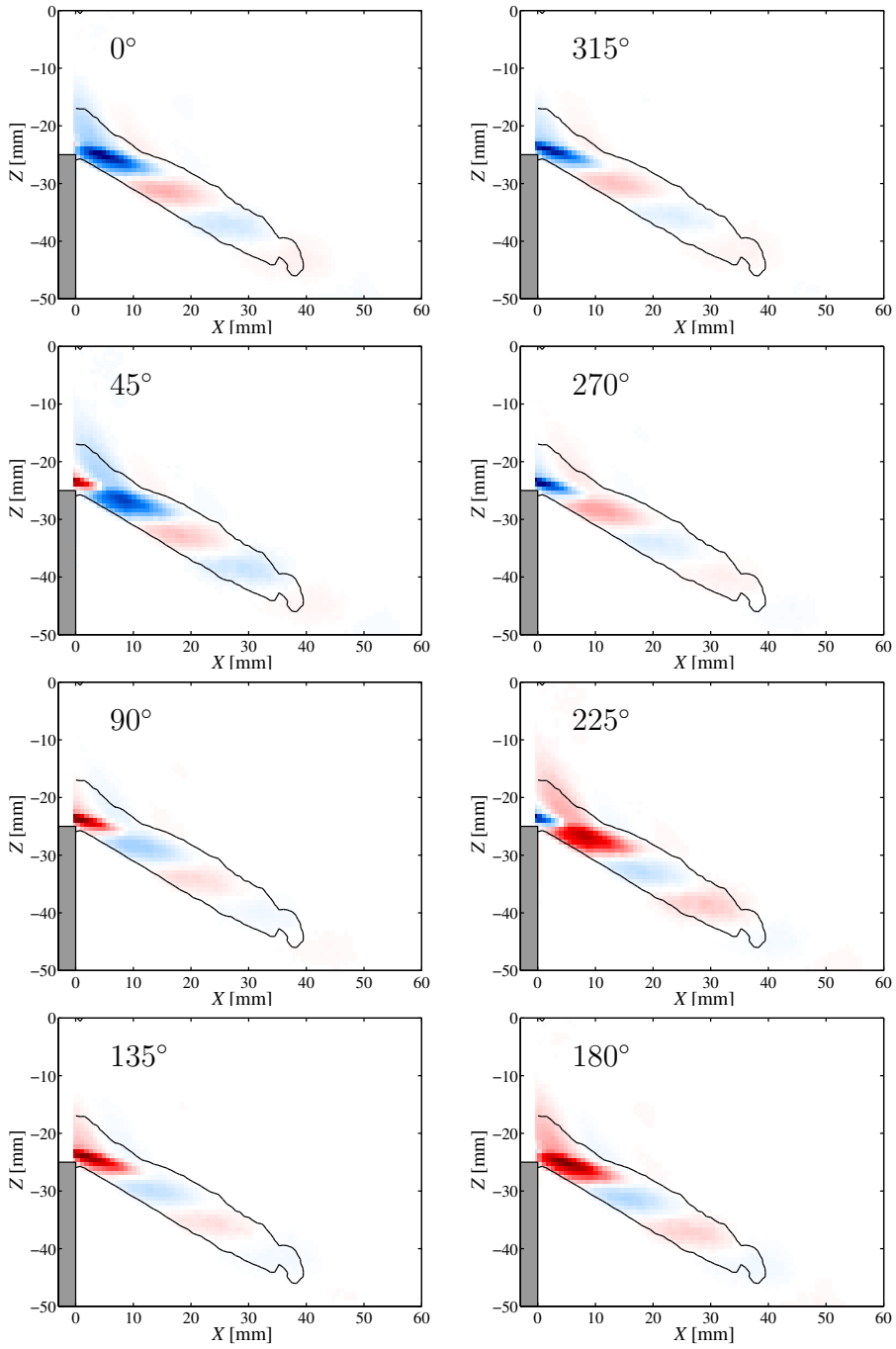

Figure 4.15: Reconstructed DMD mode associate with the helical mode for the operating condition FC_{40}.

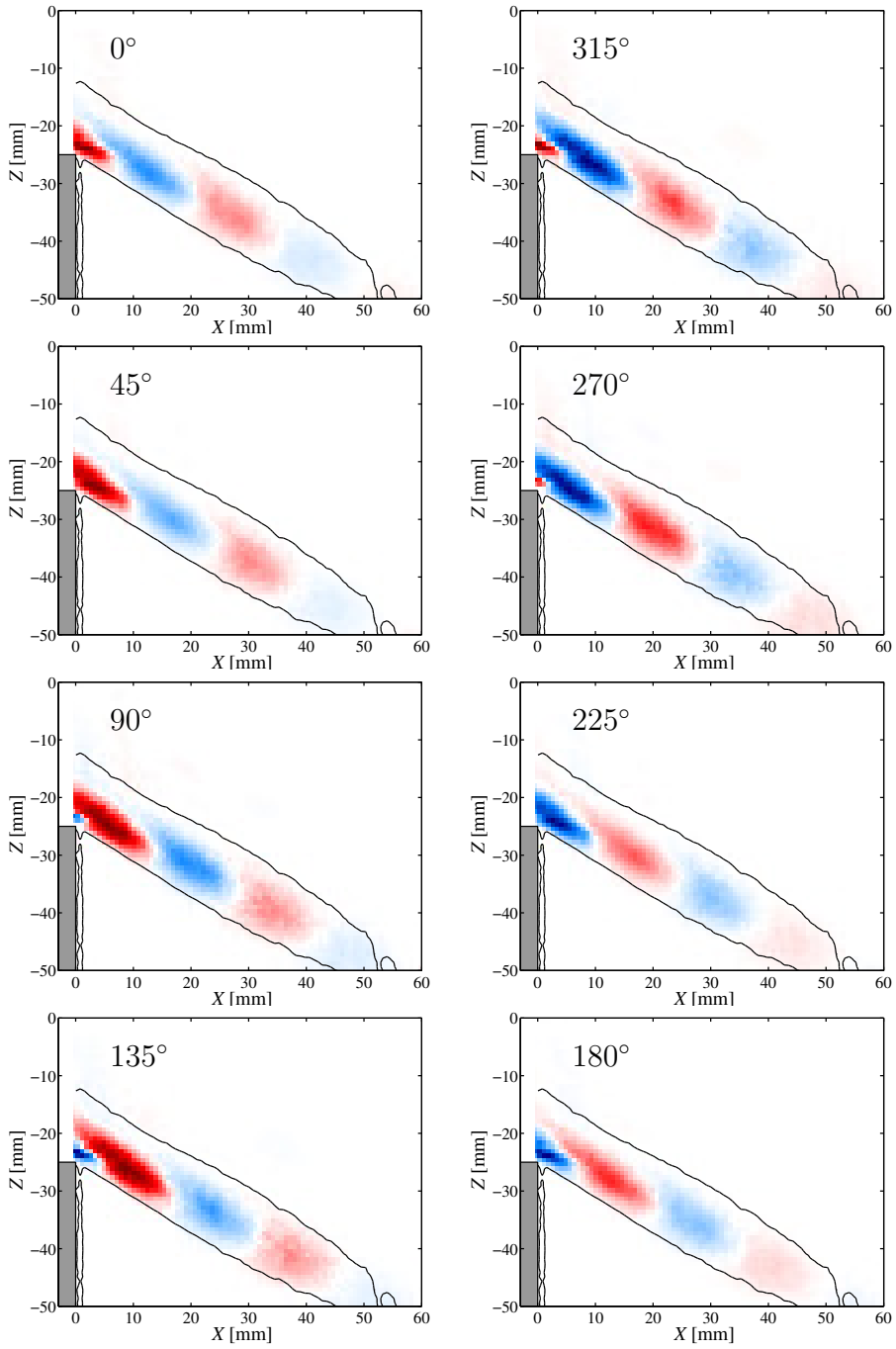

Figure 4.16: Reconstructed DMD mode associate with the helical mode for the operating condition FC_{70}.

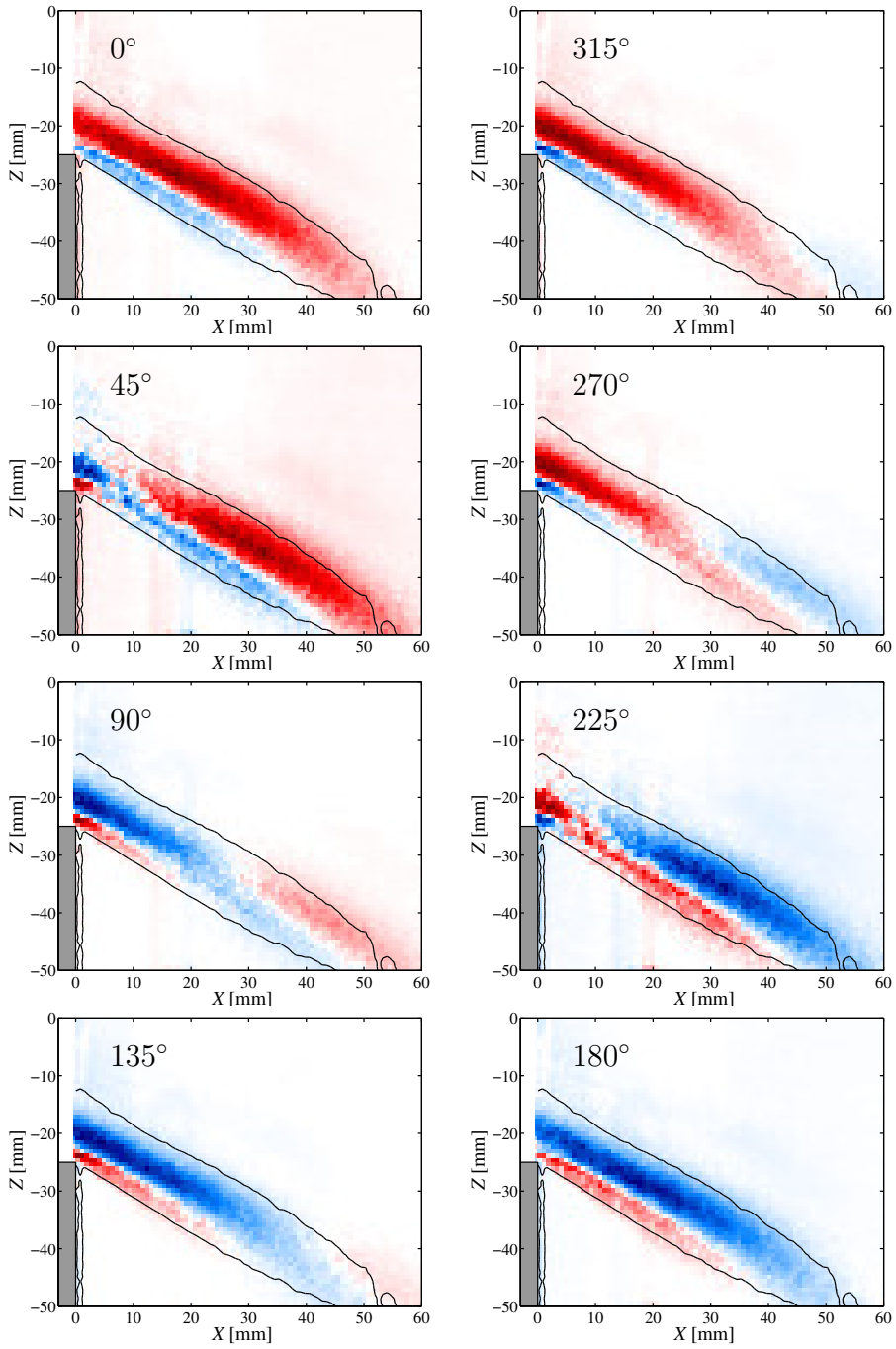

Figure 4.17: Reconstructed DMD mode associate with acoustic mode for the operating condition FC_{70}.

4.7 Dynamic mode associate to aerodynamic and acoustic oscillation

4.7.1 Temporal stability and strength of each dynamic mode

Figure 4.18 shows the frequency associated to helical structure detected in the amplitude spectra in each case. The black circles and red square represent the mean frequency for the each data set of FCs and PCs, respectively. The error bars show standard deviations that are calculated from 30 datasets. The mean helical oscillation frequencies of power constant cases show almost linear decrease with equivalence ratio increase while that of FCs almost constant between 1680 Hz and 1700 Hz. In the case of $\phi < 0.5$, the frequency variation is within several Hz for both data series, FCs and PCs. It indicates that there is a temporally well-defined helical mode only depending on global air flow rate regardless of equivalence ratio unless the mode loses its temporal coherence in the case of $\phi > 0.5$ where the standard deviation of the frequency increases.

On the other hand, the evolution of frequency associated to the acoustic oscillation is shown in Fig. 4.19. In this case, standard deviation (σ) is shown in the right axis to show clearly the change in each condition. For all cases, the characteristic frequencies are between 280 and 360 Hz with relatively high standard deviation. In contrast to the helical mode, the standard deviation becomes low with increase of the equivalence ratio especially in PCs. Therefore, the acoustic oscillation becomes temporally well-defined in high equivalence ratio conditions.

To analyze the strength of a dynamic mode from the spectra, one must be careful because the multi-variable DMD contains Mie signal, which depends on the droplet size. As mentioned in the last section, it changes with spray condition. To allow comparisons between the runs, an “intensity” of the dynamic mode that represents helical structure is computed from the amplitude spectrum as a signal to noise ratio (SNR) of the peak. The height of the peak at the helical oscillation frequency is divided by the baseline (mean value of the signal range

between $f_h - \Delta f$ Hz and $f_h + \Delta f$ Hz). In this study, Δf is chosen to be 200 Hz. Figures 4.20 show the intensity of the helical structure in the both cases of FCs (black circle) and PCs (red square) in the reactive cases (Fig. 4.20a) as well as in the non-reactive cases (Fig. 4.20b) as a reference. Same analyses with different Δf are performed within a range, which does not contain other distinct peak. Consequently, they do not change the result qualitatively.

The standard deviation of this treatment is around $\pm 30\%$, which is quite high but the amount of runs enable tendencies to be drawn. For both cases, the strength is high in low equivalence ratio conditions ($FC_{40,45}$ and $PC_{40,45}$) while it seems to drop between $\phi = 0.45$ and 0.55. On the other hand, the SNRs for both cases in non-reacting flow remain constant (Fig. 4.20b). One cannot see clear difference in its tendency between two sets of data: changing equivalence ratio with air flow rate constant (FCs) or power constant (PCs).

The strength of the acoustic modes is also calculated in the same manner as for helical oscillation mode. Figure 4.21 shows the SNR of acoustic mode in the both cases of FCs (black circle) and PCs (red square). The strength of the acoustics fluctuation shows constant increase with the equivalence ratio. This is consistent with an evolution of SPL. Furthermore, it is shown that the acoustic oscillation dominates the whole system in high equivalence ratio condition.

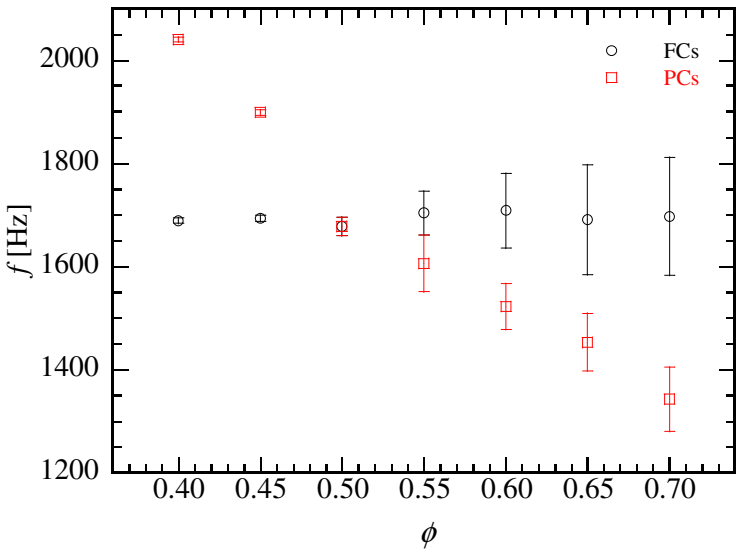

Figure 4.18: Detected frequency corresponding helical mode from multi-variable DMD for each condition.

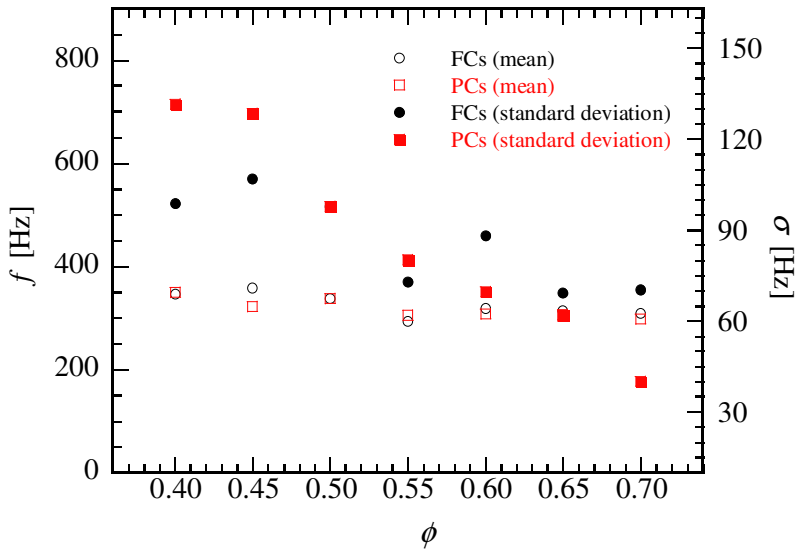

Figure 4.19: Detected frequency corresponding acoustic mode from multi-variable DMD for each condition.

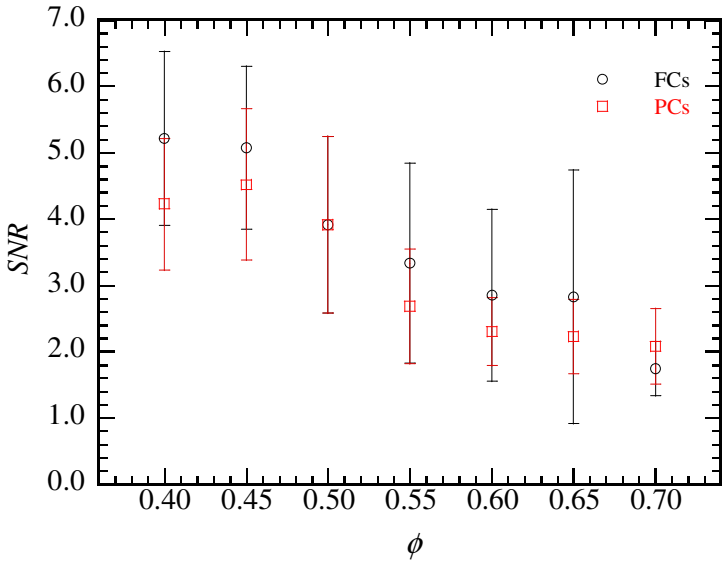

(a) Reactive cases

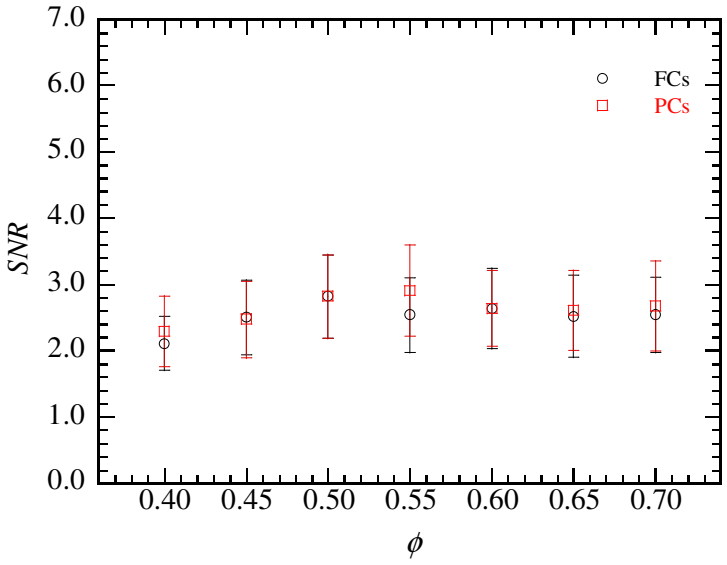

(b) Non-Reactive cases

Figure 4.20: The strength of helical mode as a function of equivalence ratio with FCs (black) and PCs (red).

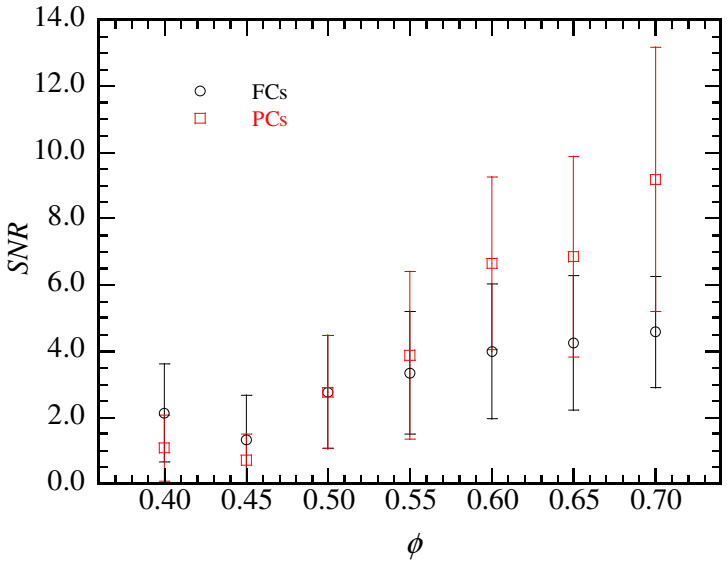

Figure 4.21: The strength of acoustic mode as a function of equivalence ratio with FCs (black) and PCs (red).

4.7.2 Coherence of helical structure

As discussed in above, the helical structure is temporally well defined and mode strength is high in the low equivalence ratio condition and its strength decrease with the equivalence ratio increase while the acoustic oscillation is becoming stronger and temporally well-defined. A concern here is if the spatial structure of helix itself alters with equivalence ratio change or the structure is coherent in any condition and its relative strength just getting weaker. To determine the coherence of the spatial distribution of modes associated to the frequency of helical oscillation in each mode, correlation coefficient of each run is calculated.

Figure 4.22 shows the correlation coefficient of the reconstructed mode between FC_{50} and the other cases. Since the dominant mode seems to be different between higher and lower equivalence ratio of 0.5, FC_{50} is chosen to be a reference in this analysis. The correlation coefficient is calculated only in regions of mean Mie scattering intensity above 25% of the maximum intensity.

Figure 4.22a shows the correlation coefficient for the operating conditions FCs (black circle) and PCs (red square). Figure 4.22b is for the case of non-reactive sprays with both same air flow and same fuel injection condition as a reference case. In the low equivalence ratio conditions, $FC_{40,45}$ and $PC_{40,45}$ in Fig. 4.22a, the correlation coefficient is very high (> 0.9) and its variation is small. It means that the spatial structure of helical mode is not change, suggesting that the aerodynamic instability possesses coherent helical structure in low equivalence ratio conditions. The correlation coefficient in FC/PC_{50} distribute with larger standard deviation while the values itself are still high. With increasing equivalence ratio, the mean value decreases and the standard deviation increases.

In the non-reactive cases, the mean correlation coefficient remain high (> 0.9) in the high equivalence ratio conditions. This means that the changes in the spray do not alter the helical structure. The decrease of the value can be seen higher equivalence ratio case ($\phi > 0.5$). This corresponds to the change in the mode strength in Fig. 4.20a. The coefficients are lower in the conditions PCs than that

in FCs since the global flow rate alters with different equivalence ratio, hence the mean distribution of the droplets also alters.

One may conclude that there is a temporally well defined and spatially coherent helical mode in the low equivalence ratio cases in $\phi \leqq 0.5$. In higher equivalence ratio cases, the helical mode loses the coherence, and dominant mode switches to the acoustic oscillation.

The helical structure has an effect to stabilize flame in upstream of the chamber by enhancing the mixing of air and fuel [18, 23, 24]. Therefore, weakening the helical mode leads to modification of the flame anchoring process. The mode changes coincide with the evolution of SPL with equivalence ratio change, which is measured by microphones (as shown in Fig. 4.6). This can be the result of flame–turbulence interaction. The acoustic pressure oscillation vibrates the helical structure and results in a loss of the stability and the coherence. The weakening the helical mode changes flame anchoring process, leading to the increase of unsteady flame fluctuation and the coupling of heat release and pressure oscillation. The measurement of local flame structure such as CH and OH PLIF is highly required to investigate such flame–turbulence interaction.

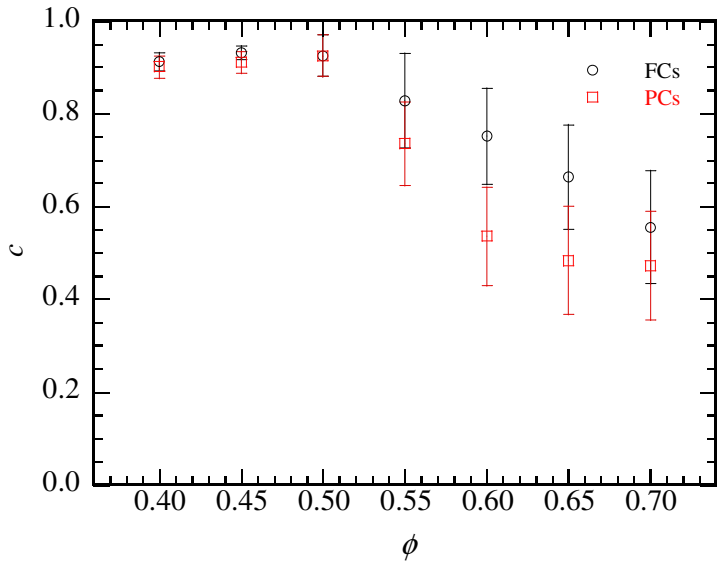

(a) Reactive cases

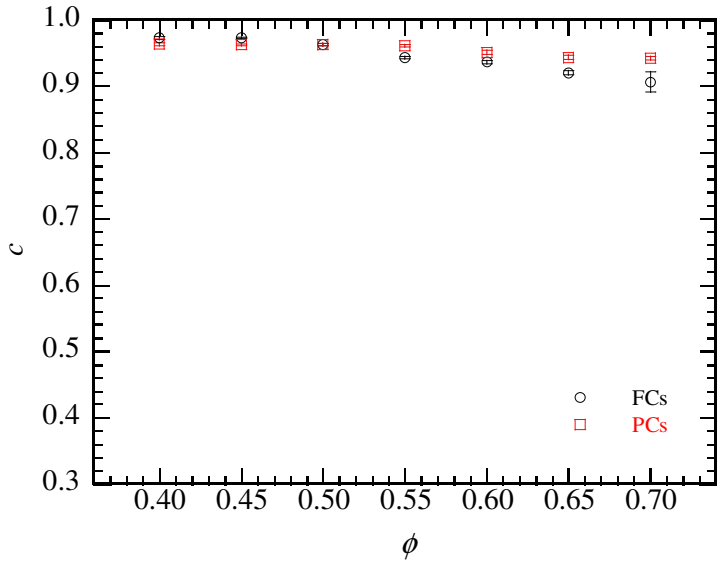

(b) Non-Reactive cases

Figure 4.22: The correlation coefficient of DMD mode associated to helical oscillation between equivalence ratio 0.50 case (FC/PC_{50}) and others. The operating conditions FCs (black) and PCs (red).

4.8 Interim conclusions

In this chapter, the two dominant modes that are acoustic and aerodynamic instability have been investigated in the liquid-fueled (dodecane) swirl-stabilized combustor with varying global equivalence ratio. To give detailed insight into the flow dynamics, multi-variable DMD has been introduced. The obtained results are as follows.

(1) In swirl-stabilized combustor, the helical structure associated to the aerodynamic instability and the oscillation caused by thermoacoustic instability exist.

(2) There is a temporally well defined and spatially coherent helical mode regardless of the global equivalence ratio in the case of $\phi \leqq 0.50$ and aerodynamic instability is dominant, while in higher equivalence ratio cases, the helical mode loses the temporal and spatial coherence, and dominant mode switches to the acoustic oscillation.

Chapter 5

Conclusions

In this study, flame and flow dynamics in turbulent combustion have been investigated by the high-speed laser diagnostics in order to contribute the development of highly-efficient and low-emission combustor. The results obtained in each chapter are summarized in the present chapter as follows.

In chapter 2, high repetition rate simultaneous measurement consisting of CH–OH PLIF and stereoscopic PIV with an acquisition rate of 10 kHz and a measurement duration exceeding 1.0 s has been developed. The obtained results are summarized as follows.

(1) With increasing the jet velocity, the number of flame wrinklings increases and the flame front turns to exhibit a very complicated geometry, leading to the creation of the large-scale unburned mixture islands in high Reynolds number turbulent jet premixed flame.

(2) The large-scale unburned mixture islands are split into many fine-scale unburned mixtures. These fine-scale mixtures are expected to be consumed very rapidly, they may enhance the turbulent burning velocity of the entire jet flame.

(3) When sequential OH and CH PLIF images are observed simultaneously in high Reynolds number turbulence, some regions of fine-scale unburned mixtures are detected only in the CH images.

(4) The developed high-speed measurement system based on simultaneous CH–OH PLIF and stereoscopic PIV can investigate flame and flow dynamics in turbulent combustion.

In chapter 3, to clarify the flame and flow dynamics of turbulent premixed flame in high Reynolds number turbulence, the rapid consumption of the fine-scale unburned mixtures, which are observed around the flame tip of the turbulent jet, has been investigated. The followings are the obtained results.

(1) The formation and the rapid consumption of the fine-scale unburned mixture are dominant structures around the tip of high Reynolds number turbulent jet flame.

(2) The radius of the fine-scale unburned mixtures is approximately 1 mm, of the order of Taylor micro scale.

(3) Every consumption rate which is obtained from CH/OH PLIF images on the basis of spherical and pillar assumption, is much higher than the laminar burning velocity (0.39 m/s).

(4) The most probable consumption rate as a function of mean curvature suggests the increase of the consumption rate with decreasing curvature (or decreasing radius of the mixture).

(5) There are two dominant effects on the consumption rate, which are heating up of the mixtures by surrounding burned gas and strain rate due to turbulence.

In chapter 4, the two dominant modes that are acoustic and aerodynamic instability have been investigated in the liquid-fueled (dodecane) swirl-stabilized combustor with varying global equivalence ratio. To give detailed insight into the flow dynamics, multi-variable DMD has been introduced. The obtained results are as follows.

(1) In swirl-stabilized combustor, the helical structure associated to the aerodynamic instability and the oscillation caused by thermoacoustic instability exist.

(2) There is a temporally well-defined and spatially coherent helical mode regardless of the global equivalence ratio in the case of $\phi \leqq 0.50$ and aerodynamic instability is dominant, while in higher equivalence ratio cases, the helical mode loses the temporal and spatial coherence, and dominant mode switches to the acoustic oscillation.

References

[1] IEA. Energy Balance 2013, 2013.

[2] 経済産業省. エネルギー白書 2014 年版, 2014.

[3] BP. BP Energy Outlook 2035, 2014.

[4] F. Birol, J. Corben, M. Argiri, M. Baroni, A. Corbeau, L. Cozzi, and A. Yanagisawa. Are we entering a golden age of gas? *IEA World Energy Outlook*, 2011.

[5] N. Peters. *Turbulent combustion*. Cambridge university press, 2000.

[6] A. Kerstein, W. Ashurst, and F. Williams. Field equation for interface propagation in an unsteady homogeneous flow field. *Phys. Rev. A*, 37:2728–2731, Apr 1988. doi: http://dx.doi.org/10.1103/PhysRevA.37.2728.

[7] N. Shiwaku, Y. Nada, M. Tanahashi, and T. Miyauchi. SGS modeling of hierarchical structures in turbulent premixed flames for large eddy simulation. In *Proceedings of 11th Conference on Numerical Combustion*, page 40, 2006.

[8] T. Miyauchi, M. Tanahashi, and F. Gao. Translated from nensho no kagaku to gijutsu, 1, 29 (1992) fractal characteristics of turbulent diffusion flames. *Combustion Science and Technology*, 96(1-3):135–154, 1994. doi: http://dx.doi.org/10.1080/00102209408935351.

[9] I. Yoshikawa, Y.-S. Shim, Y. Nada, M. Tanahashi, and T. Miyauchi. A dynamic SGS combustion model based on fractal characteristics of turbulent premixed flames. *Proceedings of the Combustion Institute*, 34(1):1373 – 1381, 2013. doi: http://dx.doi.org/10.1016/j.proci.2012.06.166.

[10] S. M. Correa. Power generation and aeropropulsion gas turbines: from combustion science to combustion technology. In *Symposium (International) on Combustion*, volume 27, pages 1793–1807. Elsevier, 1998. doi: http://dx.doi.org/10.1016/S0082-0784(98)80021-0.

[11] A. H. Lefebvre. *Gas turbine combustion*. Taylor & Francis, 1999.

[12] R. Tacina. Low NO(x) potential of gas turbine engines. 1990. doi: http://dx.doi.org/10.2514/6.1990-550.

[13] A. Lefebvre. The role of fuel preparation in low-emission combustion. *Journal of engineering for gas turbines and power*, 117(4):617–654, 1995. doi: http://dx.doi.org/10.1115/1.2815449.

[14] M. Moore. Nox emission control in gas turbines for combined cycle gas turbine plant. *Proceedings of the Institution of Mechanical Engineers, Part A: Journal of Power and Energy*, 211(1):43–52, 1997. doi: http://dx.doi.org/10.1243/0957650971536980.

[15] J. Fritz, M. Kroner, and T. Sattelmayer. Flashback in a swirl burner with cylindrical premixing zone. *Journal of engineering for gas turbines and power*, 126(2):276–283, 2004. doi: http://dx.doi.org/10.1115/1.1473155.

[16] M. Konle, F. Kiesewetter, and T. Sattelmayer. Simultaneous high repetition rate PIV–LIF-measurements of CIVB driven flashback. *Experiments in Fluids*, 44(4):529–538, 2008. doi: http://dx.doi.org/10.1007/s00348-007-0411-2.

[17] S. Candel. Combustion dynamics and control: progress and challenges. *Proceedings of the combustion institute*, 29(1):1–28, 2002. doi: http://dx.doi.org/10.1016/S1540-7489(02)80007-4.

[18] Y. Huang and V. Yang. Dynamics and stability of lean-premixed swirl-stabilized combustion. *Progress in Energy and Combustion Science*, 35(4): 293 – 364, 2009. doi: http://dx.doi.org/10.1016/j.pecs.2009.01.002.

[19] J. Rayleigh. The explanation of certain acoustical phenomena. *Nature*, 18 (455):319–321, 1878.

[20] A. K. Gupta. *Swirl flows*. Technomic Publishing Co., Lancaster, PA, 1984.

[21] O. Lucca-Negro and T. O'doherty. Vortex breakdown: a review. *Progress in energy and combustion science*, 27(4):431–481, 2001. doi: http://dx.doi.org/10.1016/S0360-1285(00)00022-8.

[22] N. Syred. A review of oscillation mechanisms and the role of the precessing vortex core (pvc) in swirl combustion systems. *Progress in Energy and Combustion Science*, 32(2):93–161, 2006. doi: http://dx.doi.org/10.1016/j.pecs.2005.10.002.

[23] I. Boxx, M. Stöhr, C. Carter, and W. Meier. Temporally resolved planar measurements of transient phenomena in a partially pre-mixed swirl flame in a gas turbine model combustor. *Combustion and Flame*, 157(8):1510–1525, 2010. doi: http://dx.doi.org/10.1016/j.combustflame.2009.12.015.

[24] D. Galley, S. Ducruix, F. Lacas, and D. Veynante. Mixing and stabilization study of a partially premixed swirling flame using laser induced fluorescence. *Combustion and Flame*, 158(1):155–171, 2011. doi: http://dx.doi.org/10.1016/j.combustflame.2010.08.004.

[25] R. K. Hanson. Combustion diagnostics: planar imaging techniques. In

Symposium (International) on Combustion, volume 21, pages 1677–1691. Elsevier, 1988. doi: http://dx.doi.org/10.1016/S0082-0784(88)80401-6.

[26] M. Dyer and D. Crosley. Fluorescence imaging for flame chemistry. In *Proceedings of the International Conference on Lasers*, volume 84, pages 211–218. Elsevier, 1985.

[27] M. Smooke, Y. Xu, R. Zurn, P. Lin, J. Frank, and M. Long. Computational and experimental study of OH and CH radicals in axisymmetric laminar diffusion flames. In *Symposium (International) on Combustion*, volume 24, pages 813–821. Elsevier, 1992. doi: http://dx.doi.org/10.1016/S0082-0784(06)80099-8.

[28] J. M. Seitzman, J. Haumann, and R. K. Hanson. Quantitative two-photon LIF imaging of carbon monoxide in combustion gases. *Applied optics*, 26 (14):2892–2899, 1987. doi: http://dx.doi.org/10.1364/AO.26.002892.

[29] M. Allen, R. D. Howe, and R. K. Hanson. Digital imaging of reaction zones in hydrocarbon — air flames using planar laser-induced fluorescence of CH and C_2. *Optics letters*, 11(3):126–128, 1986. doi: http://dx.doi.org/10.1364/OL.11.000126.

[30] C. Carter, J. Donbar, and J. Driscoll. Simultaneous CH planar laser-induced fluorescence and particle imaging velocimetry in turbulent nonpremixed flames. *Applied Physics B: Lasers and Optics*, 66(1):129–132, 1998. doi: http://dx.doi.org/10.1007/s003400050366.

[31] M. S. Mansour, N. Peters, and Y.-C. Chen. Investigation of scalar mixing in the thin reaction zones regime using a simultaneous CH-LIF/Rayleigh laser technique. In *Symposium (International) on Combustion*, volume 27, pages 767–773. Elsevier, 1998. doi: http://dx.doi.org/10.1016/S0082-0784(98)80471-2.

[32] S. Böckle, J. Kazenwadel, D.-I. Shin, C. Schulz, J. Wolfrum, et al. Simultaneous single-shot laser-based imaging of formaldehyde, OH, and temperature in turbulent flames. *Proceedings of the Combustion Institute*, 28(1): 279–286, 2000. doi: http://dx.doi.org/10.1016/S0082-0784(00)80221-0.

[33] J. M. Donbar, J. F. Driscoll, and C. D. Carter. Reaction zone structure in turbulent nonpremixed jet flames—from CH-OH PLIF images. *Combustion and Flame*, 122(1):1–19, 2000. doi: http://dx.doi.org/10.1016/S0010-2180(00)00098-5.

[34] K. Watson, K. Lyons, J. Donbar, and C. Carter. Scalar and velocity field measurements in a lifted CH_4–air diffusion flame. *Combustion and Flame*, 117(1):257–271, 1999. doi: http://dx.doi.org/10.1016/S0010-2180(98)00086-8.

[35] M. Tanahashi, S. Murakami, G.-M. Choi, Y. Fukuchi, and T. Miyauchi. Simultaneous CH–OH PLIF and stereoscopic PIV measurements of turbulent premixed flames. *Proceedings of the Combustion Institute*, 30(1): 1665–1672, 2005. doi: http://dx.doi.org/10.1016/j.proci.2004.08.270.

[36] M. Shimura, T. Ueda, G.-M. Choi, M. Tanahashi, and T. Miyauchi. Simultaneous dual-plane CH PLIF, single-plane OH PLIF and dual-plane stereoscopic PIV measurements in methane-air turbulent premixed flames. *Proceedings of the Combustion Institute*, 33(1):775–782, 2011. doi: http://dx.doi.org/10.1016/j.proci.2010.05.026.

[37] C. Kaminski, J. Hult, and M. Aldén. High repetition rate planar laser induced fluorescence of OH in a turbulent non-premixed flame. *Applied Physics B: Lasers and Optics*, 68(4):757–760, 1999. doi: http://dx.doi.org/10.1007/s003400050700.

[38] R. Schefer, M. Namazian, E. Filtopoulos, and J. Kelly. Temporal evolution of turbulence/chemistry interactions in lifted, turbulent-jet flames. In

Symposium (International) on Combustion, volume 25, pages 1223–1231. Elsevier, 1994. doi: http://dx.doi.org/10.1016/S0082-0784(06)80762-9.

[39] K. Watson, K. Lyons, C. Carter, and J. Donbar. Simultaneous two-shot CH planar laser-induced fluorescence and particle image velocimetry measurements in lifted CH_4/air diffusion flames. *Proceedings of the Combustion Institute*, 29(2):1905–1912, 2002. doi: http://dx.doi.org/10.1016/S1540-7489(02)80231-0.

[40] S. A. Filatyev, M. P. Thariyan, R. P. Lucht, and J. P. Gore. Simultaneous stereo particle image velocimetry and double-pulsed planar laser-induced fluorescence of turbulent premixed flames. *Combustion and flame*, 150(3):201–209, 2007. doi: http://dx.doi.org/10.1016/j.combustflame.2007.02.005.

[41] M. Tanahashi, S. Taka, M. Shimura, and T. Miyauchi. CH double-pulsed PLIF measurement in turbulent premixed flame. *Experiments in Fluids*, 45(2):323–332, 2008. URL `http://dx.doi.org/10.1007/s00348-008-0482-8`.

[42] M. Cundy and V. Sick. Hydroxyl radical imaging at kHz rates using a frequency-quadrupled Nd: YLF laser. *Applied Physics B*, 96(2-3):241–245, 2009. doi: http://dx.doi.org/10.1007/s00340-009-3597-6.

[43] C. Kittler and A. Dreizler. Cinematographic imaging of hydroxyl radicals in turbulent flames by planar laser-induced fluorescence up to 5 kHz repetition rate. *Applied Physics B*, 89(2-3):163–166, 2007. doi: http://dx.doi.org/10.1007/s00340-007-2803-7.

[44] J. Wäsle, A. Winkler, and T. Sattelmayer. Spatial coherence of the heat release fluctuations in turbulent jet and swirl flames. *Flow, turbulence and combustion*, 75(1-4):29–50, 2005. doi: http://dx.doi.org/10.1007/s10494-005-8586-1.

[45] M. Juddoo and A. Masri. High-speed OH-PLIF imaging of extinction and re-ignition in non-premixed flames with various levels of oxygenation. *Combustion and Flame*, 158(5):902–914, 2011. doi: http://dx.doi.org/10.1016/j.combustflame.2011.02.003.

[46] B. Böhm, C. Heeger, I. Boxx, W. Meier, and A. Dreizler. Time-resolved conditional flow field statistics in extinguishing turbulent opposed jet flames using simultaneous highspeed PIV/OH-PLIF. *Proceedings of the Combustion Institute*, 32(2):1647–1654, 2009. doi: http://dx.doi.org/10.1016/j.proci.2008.06.136.

[47] I. Boxx, C. Heeger, R. Gordon, B. Böhm, A. Dreizler, and W. Meier. On the importance of temporal context in interpretation of flame discontinuities. *Combustion and Flame*, 156(1):269–271, 2009. doi: http://dx.doi.org/10.1016/j.combustflame.2008.09.010.

[48] A. Steinberg, I. Boxx, C. Arndt, J. Frank, and W. Meier. Experimental study of flame-hole reignition mechanisms in a turbulent non-premixed jet flame using sustained multi-kHz PIV and crossed-plane OH PLIF. *Proceedings of the Combustion Institute*, 33(1):1663–1672, 2011. doi: http://dx.doi.org/10.1016/j.proci.2010.06.134.

[49] A. Steinberg, I. Boxx, M. Stöhr, C. Carter, and W. Meier. Flow–flame interactions causing acoustically coupled heat release fluctuations in a thermo-acoustically unstable gas turbine model combustor. *Combustion and Flame*, 157(12):2250–2266, 2010. doi: http://dx.doi.org/10.1016/j.combustflame.2010.07.011.

[50] W. Meier, I. Boxx, M. Stöhr, and C. Carter. Laser-based investigations in gas turbine model combustors. *Experiments in fluids*, 49(4):865–882, 2010. doi: http://dx.doi.org/10.1007/s00348-010-0889-x.

[51] I. Boxx, C. M. Arndt, C. D. Carter, and W. Meier. High-speed laser diagnostics for the study of flame dynamics in a lean premixed gas turbine model combustor. *Experiments in fluids*, 52(3):555–567, 2012. doi: http://dx.doi.org/10.1007/s00348-010-1022-x.

[52] P. Trunk, I. Boxx, C. Heeger, W. Meier, B. Böhm, and A. Dreizler. Premixed flame propagation in turbulent flow by means of stereoscopic PIV and dual-plane OH-PLIF at sustained kHz repetition rates. *Proceedings of the Combustion Institute*, 34(2):3565–3572, 2013.

[53] B. Peterson, E. Baum, B. Böhm, and A. Dreizler. Early flame propagation in a spark-ignition engine measured with quasi 4D-diagnostics. *Proceedings of the Combustion Institute*, 35(3):3829 – 3837, 2015. doi: http://dx.doi.org/10.1016/j.proci.2014.05.131.

[54] N. Jiang, R. A. Patton, W. R. Lempert, and J. A. Sutton. Development of high-repetition rate CH PLIF imaging in turbulent nonpremixed flames. *Proceedings of the Combustion Institute*, 33(1):767–774, 2011. doi: http://dx.doi.org/10.1016/j.proci.2010.05.080.

[55] J. D. Miller, S. R. Engel, T. R. Meyer, T. Seeger, and A. Leipertz. *Optics Letters*, (19):3927–3929. doi: http://dx.doi.org/10.1364/OL.36.003927.

[56] C. D. Carter, S. Hammack, and T. Lee. High-speed planar laser-induced fluorescence of the CH radical using the $C^2\Sigma^+ - X^2\Pi\,(0,0)$ band. *Applied Physics B*, 116(3):515–519, 2014. doi: http://dx.doi.org/10.1007/s00340-014-5899-6.

[57] R. Wood. Lviii. the fluorescence of sodium vapour and the resonance radiation of electrons. *Philosophical Magazine Series 6*, 10(59):513–525, 1905. doi: http://dx.doi.org/10.1080/14786440509463399.

[58] J. W. Daily. Laser induced fluorescence spectroscopy in flames.

Progress in Energy and Combustion Science, 23(2):133–199, 1997. doi: http://dx.doi.org/10.1016/S0360-1285(97)00008-7.

[59] N. M. Laurendeau. Temperature measurements by light-scattering methods. *Progress in energy and combustion science*, 14(2):147–170, 1988. doi: http://dx.doi.org/10.1016/0360-1285(88)90002-0.

[60] J. McDaniel, D. Baganoff, and R. Byer. Density measurement in compressible flows using off-resonant laser-induced fluorescence. *Physics of Fluids*, 25(7):1105–1107, 1982. doi: http://dx.doi.org/10.1063/1.863872.

[61] W. P. Partridge and N. M. Laurendeau. Formulation of a dimensionless overlap fraction to account for spectrally distributed interactions in fluorescence studies. *Applied Optics*, 34(15):2645–2647, 1995. doi: http://dx.doi.org/10.1364/AO.34.002645.

[62] W. L. Wiese, M. W. Smith, and B. M. Glennon. Atomic transition probabilities, Vol. i: Hydrogen through neon – A critical data compilation. In *Nat. Stand. Ref. Data Ser., NSRDS-NBS 4*. U.S. Government Printing Office, Washington, D.C., 1966.

[63] W. L. Wiese, M. W. Smith, and B. M. Miles. Atomic transition probabilities, Vol. ii: Sodium through calcium - A critical data compilation. In *Nat. Stand. Ref. Data Ser., NSRDS-NBS 22*. U.S. Government Printing Office, Washington, D.C., 1969.

[64] A. Radzig and B. Smirnof. Reference data on atoms, molecules and ions. *Springer-Verlag Series in Chemical Physics*, 31, 1985. doi: http://dx.doi.org/10.1007/978-3-642-82048-9.

[65] J. Luque and D. Crosley. OH,CH and NO spectroscopic database and spectra simulation. *SRI International, Version 0.99d*, 1994.

[66] C. E. Willert and M. Gharib. Digital particle image velocimetry. *Experiments in fluids*, 10(4):181–193, 1991. doi: http://dx.doi.org/10.1007/BF00190388.

[67] R. D. Keane and R. J. Adrian. Theory and simulation of particle image velocimetry. In *Laser Anemometry: Advances and Applications–Fifth International Conference*, pages 477–492. International Society for Optics and Photonics, 1993. doi: http://dx.doi.org/10.1117/12.150541.

[68] S. Kumar and S. Banerjee. Development and application of a hierarchical system for digital particle image velocimetry to free-surface turbulence. *Physics of Fluids*, 10(1):160–177, 1998. doi: http://dx.doi.org/10.1063/1.869558.

[69] J. Westerweel, D. Dabiri, and M. Gharib. The effect of a discrete window offset on the accuracy of cross-correlation analysis of digital PIV recordings. *Experiments in fluids*, 23(1):20–28, 1997. doi: http://dx.doi.org/10.1007/s003480050082.

[70] M. Tanahashi, M. Ootsu, M. Fukushima, and T. Miyauchi. Measurement of coherent fine scale eddies in turbulent mixing layer by DPIV. *Engineering Turbulence Modelling and Experiments 5, Elsevier Science*, pages 525–534, 2002.

[71] V. Gauthier and M. Riethmuller. Application of particle image displacement velocimetry (PIDV) to complex flows: measurements of the third component. In *Particle Image Displacement Velocimetry*, volume 1, 1988.

[72] A. Prasad and R. Adrian. Stereoscopic particle image velocimetry applied to liquid flows. *Experiments in Fluids*, 15(1):49–60, 1993. doi: http://dx.doi.org/10.1007/BF00195595.

[73] R. J. Adrian. Particle-imaging techniques for experimental fluid mechanics. *Annual review of fluid mechanics*, 23(1):261–304, 1991. doi: http://dx.doi.org/10.1146/annurev.fl.23.010191.001401.

[74] A. K. Prasad and K. Jensen. Scheimpflug stereocamera for particle image velocimetry in liquid flows. *Applied optics*, 34(30):7092–7099, 1995. doi: http://dx.doi.org/10.1364/AO.34.007092.

[75] A. K. Prasad. Stereoscopic particle image velocimetry. *Experiments in fluids*, 29(2):103–116, 2000. doi: http://dx.doi.org/10.1007/s003480000143.

[76] C. Willert. Stereoscopic digital particle image velocimetry for application in wind tunnel flows. *Measurement science and technology*, 8(12):1465, 1997. doi: http://dx.doi.org/10.1088/0957-0233/8/12/010.

[77] M. Tanahashi, T. Hirayama, S. Taka, and T. Miyauchi. Measurement of fine scale structure in turbulence by time-resolved dual-plane stereoscopic PIV. *International Journal of Heat and Fluid Flow*, 29(3):792–802, 2008. doi: http://dx.doi.org/10.1016/j.ijheatfluidflow.2008.02.009.

[78] T. Poinsot, D. Veynante, and S. Candel. Quenching processes and premixed turbulent combustion diagrams. *Journal of Fluid Mechanics*, 228:561–606, 1991. doi: 10.1017/S0022112091002823.

[79] W. Roberts, J. Driscoll, M. Drake, and J. Ratcliffe. OH fluorescence images of the quenching of a premixed flame during an interaction with a vortex. In *Symposium (International) on Combustion*, volume 24, pages 169–176. Elsevier, 1992. doi: http://dx.doi.org/10.1016/S0082-0784(06)80025-1.

[80] S. A. Filatyev, J. F. Driscoll, C. D. Carter, and J. M. Donbar. Measured properties of turbulent premixed flames for model assessment, including burning velocities, stretch rates, and surface densities. *Combustion and Flame*, 141(1):1–21, 2005. doi: http://dx.doi.org/10.1016/j.combustflame.2004.07.010.

[81] H. Kobayashi, K. Seyama, H. Hagiwara, and Y. Ogami. Burning velocity correlation of methane/air turbulent premixed flames at high pressure and high temperature. *Proceedings of the Combustion Institute*, 30(1):827–834, 2005. doi: http://dx.doi.org/10.1016/j.proci.2004.08.098.

[82] Z. Li, B. Li, Z. Sun, X.-S. Bai, and M. Aldén. Turbulence and combustion interaction: High resolution local flame front structure visualization using simultaneous single-shot PLIF imaging of CH, OH, and CH_2o in a piloted premixed jet flame. *Combustion and Flame*, 157(6):1087–1096, 2010. doi: http://dx.doi.org/10.1016/j.combustflame.2010.02.017.

[83] M. Shimura, K. Yamawaki, N. Fukushima, Y. Shim, Y. Nada, M. Tanahashi, and T. Miyauchi. Flame and eddy structures in hydrogen–air turbulent jet premixed flame. *Journal of Turbulence*, (13), 2012. doi: http://dx.doi.org/10.1080/14685248.2012.720022.

[84] J. B. Bell, M. S. Day, and J. F. Grcar. Numerical simulation of premixed turbulent methane combustion. *Proceedings of the Combustion Institute*, 29(2):1987–1993, 2002. doi: http://dx.doi.org/10.1016/S1540-7489(02)80242-5.

[85] Y. Nada, M. Tanahashi, and T. Miyauchi. Effect of turbulence characteristics on local flame structure of H_2-air premixed flames. *Journal of Turbulence*, 5(16):1–3, 2004. doi: http://dx.doi.org/10.1088/1468-5248/5/1/016.

[86] M. Tanahashi, M. Fujimura, and T. Miyauchi. Coherent fine-scale eddies in turbulent premixed flames. *Proceedings of the Combustion Institute*, 28(1): 529 – 535, 2000. doi: http://dx.doi.org/10.1016/S0082-0784(00)80252-0.

[87] J. L. Lumley. The structure of inhomogeneous turbulent flows. *Atmospheric turbulence and radio wave propagation*, pages 166–178, 1967.

[88] L. Sirovich. Turbulence and the dynamics of coherent structures. i-Coherent structures. ii-Symmetries and transformations. iii-Dynamics and scaling. *Quarterly of applied mathematics*, 45:561–571, 1987.

[89] G. Berkooz, P. Holmes, and J. L. Lumley. The proper orthogonal decomposition in the analysis of turbulent flows. *Annual review of fluid mechanics*, 25(1). doi: http://dx.doi.org/10.1146/annurev.fl.25.010193.002543.

[90] K. E. Meyer, J. M. Pedersen, and O. Özcan. A turbulent jet in crossflow analysed with proper orthogonal decomposition. *Journal of Fluid Mechanics*, 583:199–227. doi: http://dx.doi.org/10.1017/S0022112007006143.

[91] C. Duwig, S. Ducruix, and D. Veynante. Studying the stabilization dynamics of swirling partially premixed flames by proper orthogonal decomposition. *Journal of Engineering for Gas Turbines and Power*, 134(10):101501. doi: http://dx.doi.org/10.1115/1.4007013.

[92] D. Ballal and A. Lefebvre. The structure and propagation of turbulent flames. *Proceedings of the Royal Society of London. A. Mathematical and Physical Sciences*, 344(1637):217–234, 1975. doi: http://dx.doi.org/10.2307/78959.

[93] G. J. Smallwood, Ö. Gülder, D. R. Snelling, B. Deschamps, and I. Gökalp. Characterization of flame front surfaces in turbulent premixed methane/air combustion. *Combustion and Flame*, 101(4):461–470, 1995. doi: http://dx.doi.org/10.1016/0010-2180(94)00226-I.

[94] H. Kobayashi, T. Tamura, K. Maruta, T. Niioka, and F. A. Williams. Burning velocity of turbulent premixed flames in a high-pressure environment. In *Symposium (International) on Combustion*, volume 26, pages 389–396. Elsevier, 1996. doi: http://dx.doi.org/10.1016/S0082-0784(96)80240-2.

[95] D. Bradley, M. Lawes, and M. Mansour. Correlation of turbulent burning velocities of ethanol–air, measured in a fan-stirred bomb up

to 1.2 Mpa. *Combustion and Flame*, 158(1):123–138, 2011. doi: http://dx.doi.org/10.1016/j.combustflame.2010.08.001.

[96] R. Abdel-Gayed, D. Bradley, M. Lawes, and F.-K. Lung. Premixed turbulent burning during explosions. In *Symposium (International) on Combustion*, volume 21, pages 497–504. Elsevier, 1986. doi: http://dx.doi.org/10.1016/S0082-0784(88)80278-9.

[97] M. Fairweather, M. Ormsby, C. Sheppard, and R. Woolley. Turbulent burning rates of methane and methane–hydrogen mixtures. *Combustion and Flame*, 156(4):780–790, 2009. doi: http://dx.doi.org/10.1016/j.combustflame.2009.02.001.

[98] C. K. Law. *Combustion physics*. Cambridge University Press, 2006.

[99] A. F. Ibarreta, J. F. Driscoll, and D. A. Feikema. Markstein numbers of negatively stretched premixed flames: microgravity measurements and computations. *Proceedings of the Combustion Institute*, 29(2):1435–1443, 2002. doi: http://dx.doi.org/10.1016/S1540-7489(02)80176-6.

[100] M. Tanahashi, S. Inoue, M. Shimura, S. Taka, G.-M. Choi, and T. Miyauchi. Reconstructed 3D flame structures in noise-controlled swirl-stabilized combustor. *Experiments in Fluids*, 45(3):447–460, 2008. doi: http://dx.doi.org/10.1007/s00348-008-0487-3.

[101] R. J. Kee, F. M. Rupley, and J. A. Miller. Chemkin-ii: A Fortran chemical kinetics package for the analysis of gas-phase chemical kinetics. Technical report, Sandia National Labs., Livermore, CA (USA), 1989.

[102] Structure, aerodynamics, and geometry of premixed flamelets. *Progress in Energy and Combustion Science*, 26(4–6):459 – 505, 2000. doi: http://dx.doi.org/10.1016/S0360-1285(00)00018-6.

[103] C. Sun, C. Sung, L. He, and C. Law. Dynamics of weakly stretched flames: quantitative description and extraction of global flame parameters. *Combustion and Flame*, 118(1–2):108 – 128, 1999. doi: http://dx.doi.org/10.1016/S0010-2180(98)00137-0.

[104] A. Sengissen, A. Giauque, G. Staffelbach, M. Porta, W. Krebs, P. Kaufmann, and T. Poinsot. Large eddy simulation of piloting effects on turbulent swirling flames. *Proceedings of the Combustion Institute*, 31(2): 1729–1736, 2007. doi: http://dx.doi.org/10.1016/j.proci.2006.07.010.

[105] M. Tanahashi, S. Inoue, M. Shimura, S. Taka, G.-M. Choi, and T. Miyauchi. Reconstructed 3D flame structures in noise-controlled swirl-stabilized combustor. *Experiments in Fluids*, 45(3):447–460, 2008. doi: http://dx.doi.org/10.1007/s00348-008-0487-3.

[106] T. Providakis, L. Zimmer, P. Scouflaire, and S. Ducruix. Characterization of the coherent structures in swirling flames stabilized in a two-staged multi-injection burner: Influence of the staging factor. *Comptes Rendus Mecanique*, 341(1):4–14, 2013. doi: http://dx.doi.org/10.1016/j.crme.2012.10.010.

[107] K. Walsh, M. Long, M. Tanoff, and M. Smooke. Experimental and computational study of CH, CH^*, and OH^* in an axisymmetric laminar diffusion flame. In *Symposium (International) on Combustion*, volume 27, pages 615–623. Elsevier, 1998. doi: http://dx.doi.org/10.1016/S0082-0784(98)80453-0.

[108] T. Schuller, D. Durox, and S. Candel. Dynamics of and noise radiated by a perturbed impinging premixed jet flame. *Combustion and Flame*, 128(1–2): 88 – 110, 2002. doi: http://dx.doi.org/10.1016/S0010-2180(01)00334-0.

[109] Y. Hardalupas, M. Orain, C. S. Panoutsos, A. Taylor, J. Olofsson, H. Seyfried, M. Richter, J. Hult, M. Aldén, F. Hermann, and

J. Klingmann. Chemiluminescence sensor for local equivalence ratio of reacting mixtures of fuel and air (FLAMESEEK). *Applied Thermal Engineering*, 24(11–12):1619 – 1632, 2004. doi: http://dx.doi.org/10.1016/j.applthermaleng.2003.10.028.

[110] T. Yi and D. Santavicca. Combustion instability and flame structure of turbulent swirl-stabilized liquid-fueled combustion. *Journal of Propulsion and Power*, 28(5):1000–1014, 2012. doi: http://dx.doi.org/10.2514/1.B34438.

[111] D. Kang, F. Culick, and A. Ratner. Combustion dynamics of a low-swirl combustor. *Combustion and Flame*, 151(3):412 – 425, 2007. doi: http://dx.doi.org/10.1016/j.combustflame.2007.07.017.

[112] T. Providakis, L. Zimmer, P. Scouflaire, S. Ducruix, et al. Characterization of the acoustic interactions in a two-staged multi-injection combustor fed with liquid fuel. *Journal of Engineering for Gas Turbines and Power*, 134 (11), 2012. doi: http://dx.doi.org/10.1115/1.4007200.

[113] P. L. Schmid and J. L. Sesterhenn. Dynamic mode decomposition of numerical and experimental data. In *61th Annual Meeting of the APS Division of Fluid Dynamics*, volume 61, page 208. American Physical Society, 2008.

[114] C. W. Rowley, I. MEZIĆ, S. Bagheri, P. Schlatter, and D. S. Henningson. Spectral analysis of nonlinear flows. *Journal of Fluid Mechanics*, 641: 115–127, 2009. doi: http://dx.doi.org/10.1017/S0022112009992059.

[115] P. J. Schmid. Dynamic mode decomposition of numerical and experimental data. *Journal of Fluid Mechanics*, 656(1):5–28, 2010. doi: http://dx.doi.org/10.1017/S0022112010001217.

[116] P. J. Schmid. Application of the dynamic mode decomposition to experimental data. *Experiments in fluids*, 50(4):1123–1130, 2011. doi: http://dx.doi.org/10.1007/s00348-010-0911-3.

[117] F. Richecoeur, L. Hakim, A. Renaud, L. Zimmer, et al. DMD algorithms for experimental data processing in combustion. *Proceeding of the 2012 Summer Program*, pages 459–468, 2012.

[118] C. J. Dasch. One-dimensional tomography: a comparison of Abel, onion-peeling, and filtered backprojection methods. *Appl. Opt.*, 31(8):1146–1152, Mar 1992. doi: http://dx.doi.org/10.1364/AO.31.001146.

[119] T. Providakis. *Etude de la dynamique de flamme swirlé dans un injecteur diphasique multipoints étagé*. PhD thesis, Ecole Centrale Paris, 2012.

[120] L. Lamraoui. *Acoustique et dynamique de flamme dans un foyer turbulent premelange swirle : application a l' etude du bruit de combustion dans les chambres de turbines a gaz.* PhD thesis, Ecole Centrale Paris, 2011.

[121] B. Franzelli, E. Riber, M. Sanjosé, and T. Poinsot. A two-step chemical scheme for kerosene–air premixed flames. *Combustion and Flame*, 157(7):1364–1373, 2010. doi: http://dx.doi.org/10.1016/j.combustflame.2010.03.014.

[122] H. Sheen, W. Chen, S. Jeng, and T. Huang. Correlation of swirl number for a radial-type swirl generator. *Experimental Thermal and Fluid Science*, 12 (4):444 – 451, 1996. doi: http://dx.doi.org/10.1016/0894-1777(95)00135-2.

[123] M. Stöhr, I. Boxx, C. Carter, and W. Meier. Dynamics of lean blowout of a swirl-stabilized flame in a gas turbine model combustor. *Proceedings of the Combustion Institute*, 33(2):2953–2960, 2011. doi: http://dx.doi.org/10.1016/j.proci.2010.06.103.

[124] J. P. Moeck, J.-F. Bourgouin, D. Durox, T. Schuller, and S. Candel. Nonlinear interaction between a precessing vortex core and acoustic oscillations in a turbulent swirling flame. *Combustion and Flame*, 159(8):2650–2668, 2012. doi: http://dx.doi.org/10.1016/j.combustflame.2012.04.002.

[125] K. K. Chen, J. H. Tu, and C. W. Rowley. Variants of dynamic mode decomposition: boundary condition, koopman, and fourier analyses. *Journal of nonlinear science*, 22(6):887–915, 2012. doi: http://dx.doi.org/10.1007/s00332-012-9130-9.

Acknowledgment

I would like to express my appreciation and sincere thanks to my academic advisor, Prof. Tanahashi for encouraging my research and allowing me to have precious experience throughout my PhD.

I would also like to gratitude to my supervisor during the master course, Prof. Miyauchi. His advice both on the research and on my career have been valuable.

I would like to thank secretaries in the laboratory, Ms. Kawahara and Ms. Kagawa for practical support.

I am deeply grateful to Assoc. Prof. Shimura, Assist. Prof. Naka and Assist. Prof. Fukushima. I could not have been finished PhD without their supports.

My sincere thanks go to Dr. Zimmer and ERASMUS MUNDUS BEAM Program, for offering me the opportunities to stay in Ecole Centrale Paris. I would like to thank all members of EM2C, especially Antoine and Theodore who have significantly contributed the work in Chap.4.

I would like to thank Academy for Co-Creative Education of Environment and Energy Science for the financial support and offering me the valuable experience.

I would like to gratitude Japan Society for the Promotion of Science (JSPS) for allowing me to be JSPS Research Fellow from 2013.

I would like to thank co-members of the Reactive Gas Dynamics Laboratory including; Basmil, Hiraoka, Ito, Miyata, Matsui, Osawa, Aoki, Kishita, Kobayashi, Saito and Yoshida. I would also like to thank graduates of the laboratory; Tomita, Kuchiki, Katada, Park, Ogawa, Murayama, Obayashi and PEB.

Last but not least, I would like to thank my family and my friends.